

Impedance Spectroscopy for Single Cell Analysis and Dispensing

THÈSE N° 6082 (2017)

PRÉSENTÉE LE 13 OCTOBRE 2017
À LA FACULTÉ DES SCIENCES ET TECHNIQUES DE L'INGÉNIEUR
LABORATOIRE DE MICROSYSTÈMES 4
PROGRAMME DOCTORAL EN MICROSYSTÈMES ET MICROÉLECTRONIQUE

ÉCOLE POLYTECHNIQUE FÉDÉRALE DE LAUSANNE

POUR L'OBTENTION DU GRADE DE DOCTEUR ÈS SCIENCES

PAR

David Vincent BONZON

acceptée sur proposition du jury:

Prof. C. Guiducci, présidente du jury
Prof. Ph. Renaud, Prof. D. Bertrand, directeurs de thèse
Prof. M. Madou, rapporteur
Dr G. Kaigala, rapporteur
Dr P.-A. Besse, rapporteur



ÉCOLE POLYTECHNIQUE
FÉDÉRALE DE LAUSANNE

Suisse
2017

To my family,

Résumé

La cytométrie en flux est un outil essentiel en biologie et en médecine avec des applications cliniques pour le diagnostic de l'immunodéficience, l'immunosurveillance, la transplantation d'organes ainsi que de nombreuses utilisations dans la recherche fondamentale. Bien avant l'utilisation généralisée des trieurs cellulaires activés par fluorescence (FACS), le premier cytomètre en flux a été inventé par Wallace Coulter et consistait en un dispositif remarquablement simple. Le compteur Coulter consiste à faire passer des particules dans une ouverture simultanément à un courant électrique pour en mesurer les variations d'impédance électrique. Dans les années cinquante, le compteur Coulter s'est imposé comme un standard pour le comptage cellulaire et la détermination de leur taille. Plus récemment, grâce aux progrès de la miniaturisation, les cytomètres en flux micro fabriqués et basés sur la spectroscopie d'impédance ont permis l'analyse des propriétés diélectriques des cellules. Ces dispositifs ont ouverts la voie à l'analyse cellulaire sans marqueur, non invasive et ont permis la différenciation de populations cellulaires. Cependant, ces cytomètres en flux n'ont pas été conçus pour permettre la récupération de la cellule analysée et ne fournissent pas la capacité de travailler avec un nombre limité de cellules.

Premièrement, cette thèse étend la capacité des cytomètres de flux basé sur la spectroscopie d'impédance pour permettre l'isolation cellulaire sur dispositifs jetable. De nombreuses méthodes biologiques sont basées sur l'isolation cellulaire. Dans le développement de lignées cellulaires, la procédure standard implique une dilution en série. Cependant, cette approche nécessite beaucoup de temps car elle se répète sur plusieurs semaines pour assurer la clonalité. Dans cette thèse, un outil permettant l'isolation d'une cellule en une seule étape et basé sur la spectroscopie d'impédance est développé. Cet outil comprend un cône de pipette jetable intégrant un capteur cellulaire basé sur le principe de Coulter. Couplé avec une pipette instrumentée, ce cône de détection jetable permet l'isolation de cellule unique. En outre, ce système permet d'enregistrer la trace d'impédance de manière à l'utiliser comme preuve de l'isolation cellulaire.

Deuxièmement, cette thèse transpose ce concept de dispositif d'isolation cellulaire jetable sur une technologie de micro fabrication planaire standard. L'utilisation de la technologie de micro fabrication planaire permet un meilleur contrôle du comportement fluide ainsi que l'intégration de fonctions plus complexes sur le même dispositif. Cependant, un dispositif jetable nécessite un procédé de production à grande échelle et peu coûteux. Un procédé de

fabrication planaire basé sur les lignes de fabrication industrielles des circuits imprimés électroniques (PCB) est étudié pour produire différentes topologies de cytomètres de flux.

Troisièmement, cette thèse est consacrée à l'exploration des paramètres cellulaires pouvant être analysés à l'aide de la spectroscopie d'impédance. Les canaux ioniques activés par un ligand sont des protéines membranaires cellulaires réagissant de manière très sensible et spécifique à la liaison d'une molécule en modulant la perméabilité de la membrane. Ce mécanisme cellulaire a été proposé en tant qu'éléments de transduction pour développer des biocapteurs chimiques hautement sensibles et spécifiques. Cependant, cela implique les défis techniques d'une mesure électrophysiologique cellulaire sur le long terme, automatisée et intégrable. Finalement, dans cette thèse, la mesure de perméabilité des canaux ioniques activés par ligands est étudiée en utilisant la spectroscopie d'impédance pour son mode opératoire non invasif, sans marqueur ainsi que sa capacité d'analyse en temps réelle.

Mots-clés: Spectroscopie d'impédance, Spectroscopie diélectrique, compteur Coulter, Cellule unique, Isolation, Dispositif consommable, Pipette instrumentée, PCB.

Abstract

Flow cytometry is an essential tool in biology and medicine with applications in immunodeficiency diagnostic, immunosurveillance, organ transplantation in addition to its basic research usage. Before the widespread use of the Fluorescent-Activated Cell Sorting (FACS), the first flow cytometer was invented by Wallace Coulter and was embodied in a remarkably simple device. The Coulter counter principle consists in passing particles in an aperture concurrently with an electric current to measure the related impedance variations. In the fifties, the Coulter counter has established as a gold standard for cell counting and sizing. More recently, thanks to advances in miniaturization, micromachined impedance spectroscopy flow cytometers extended their analysis capabilities to the dielectric properties of cells. This opened the way to label-free and non-invasive methods for cell population differentiations such as leukocytes clustering. However, these flow cytometers were not designed for cell retrieval neither provided the ability to work with a limited number of scarce cells.

First, this thesis extends the capability of impedance based flow cytometers to perform single cell isolation on disposable devices. Today, many biological methods are based on single cell isolation. In cell lines development, the gold standard procedure involves serial dilution. However, this approach is time-consuming as it needs to be repeated over several weeks to ensure clonality. In this thesis, a tool enabling single cell isolation in one step and based on impedance spectroscopy is developed. The modeling, designing and testing of a disposable pipette tip integrating a cell sensor based on the Coulter principle is reported. Coupled with an instrumented pipette, this disposable sensing tip enables single cell dispensing. Furthermore, this system allows recording the impedance trace to be used as proof of single cell isolation.

Second, this thesis translates the concept of disposable, sterile and low-cost single-cell dispensing device on a standard planar microfabrication technology. Using a planar microfabrication technology enables a better control of the fluidic behavior and permits the integration of more complex features on the dispensing device. However, a disposable device requires a large-scale and cost-effective production method. A planar fabrication method based on the industrially standardized printed circuit board (PCB) manufacturing process is assessed to produce different topologies of flow cytometers with emphasis on the disposable aspect of the devices required for cell culture.

Third, this thesis is dedicated to further exploring the cell parameters that can be analyzed by impedance spectroscopy. Ligand-gated ion channels are cellular membrane proteins reacting very specifically and rapidly to the binding of a ligand molecule and modulate the membrane permeability. This cellular mechanism was proposed as the transducing elements for highly sensitive and specific chemical biosensors. However, this implies the engineering challenges of a long-term, automated and integrated cellular electrophysiology monitoring. Finally, in this thesis, the monitoring of ligand-gated ion channel permeability is investigated using impedance spectroscopy as a real-time, non-invasive and label free analytical technique.

Keywords: Impedance spectroscopy, Dielectric spectroscopy, Coulter counter, Single cell, Isolation, Disposable, Sensing tip, Instrumented Pipette, PCB.

Acknowledgments

This thesis was an exciting journey in the scientific world and also a fantastic opportunity to meet and interact with numerous rewarding and inspiring peoples.

First, I would like to express my deepest gratitude to Prof. Philippe Renaud, my thesis director. During my studies at EPFL, he was the professor that inspired me through his successful approach mixing physics, engineering and innovation to solve tomorrow's complex problems. He also raised my interest for micro and nano technologies as well as entrepreneurship. But most importantly, Philippe was unconditionally supportive and offered me all the opportunities encountered during this thesis.

It was also my privilege to have Prof. Daniel Bertrand as thesis co-director. Daniel is a model in his methodic problem solving approach and his unconditional passion for science. He is embodying the success in complex scientific researches while maintaining a realistic vision required for technological developments. I feel grateful that he dedicated a substantial amount of his time for my different questions and my scientific education. He initiated me to the fascinating world of electrophysiology, helped me in many encountered problems and strengthened my passion for innovation.

I also thank Dr. Pierre-André Besse, my internal examiner. He is a physicist with a strong analytical approach and thanks to the valuable time he dedicated to me, he allowed me to formalize and solve many analytical aspects of this thesis. Our numerous discussions and considerations about the similarities in semiconductor physics and electrophysiology were a real drive and pleasure for me. Also, the thesis was not the only path in which I benefited from Pierre-André support and encouragements as I had the pleasure to share many cycling and sportive adventures with him.

I also express my sincere gratitude to Prof. Marc Madou, my external examiner. Marc raised my interest for research and triggered my decision to pursue with a PhD during my master thesis under his supervision in California. I admire his open way to perform research. I also have a deep respect for him because of his humanistic approach to global education and his vision of the world of tomorrow. My stay in his lab was the opportunity to meet fantastic peoples.

Thanks to Dr. Govind Kaigala, my external examiner. I met him during a few conferences and appreciated his kindness and open-mindedness in answering my questions. Our discussions inspired my work with his concept of open space microfluidic.

Thanks to Prof. Carlotta Guiducci my thesis jury president and a former master teacher that I appreciated.

Thanks to Prof. Yann Barrandon, who envisioned the concept of a simple tool for single cell isolation and always supported me during this work. Thanks to Prof. Nicolas Mermoud who answered my questions about biotechnology. Thanks to Prof. Jan Reloef van der Meer for his help in my different projects guidance.

I was lucky to share an exciting part of this research with Georges Muller. Together we imagined the concept of the instrumented pipette for single cell dispensing and have made it happen. Along this path, strengths of one have often filled the doubts of the other and vice versa. We made a good team, which I hope, will allow us to continue this project.

Thanks to David Forchelet and Guillaume Petit-Pierre, my colleagues and close friends. We have shared many things together during this thesis. We shared doubts at some points. We also often shared excitements, challenges and learnings. But most importantly, they offered me true friendship and help at every moment we spent together.

I would like to express my gratitude to all my LMIS colleagues. In particular, I thank Arnaud Bertsch who always helped me in structuring and presenting my ideas. Thanks a lot for his patience and efficiency in reviewing my writings. Sébastien Jiguet for the numerous advices he shares with each of us in the lab. Thomas Braschler who represents an unlimited source of ideas and knowledge. Thomas is always available for fruitful discussions. Harald van Lintel for his precious advises with lab instruments and setup fabrication.

All this work would not have been possible without the help of my numerous and talented students; Simon, Oussama, Camille, Florence, Steve, Berenice, Niklas, Nicolas K., Jonas and Luc. Without forgetting many precious collaborators on the different projects; Nicolas U., Nicolas B., Fiona, Jean-Baptiste.

A special thanks to Benoîte Bargeton who prepared and provided me with all the frog oocytes and solutions used during the experimental part of this thesis. Her knowledge and experience in electrophysiology was also of great help to tackle this project.

I also would like to express my gratitude to Shady Gawad, one of the pioneers in micromachined impedance spectroscopy flow cytometers and that became a friend over the different discussions and passions we shared together.

I acknowledge the help from Marc Lany and Sensima Inspection for providing me with the SI-QSD lock-in with numerous advices for its integration. I'm grateful for all the enriching discussions we had with Marc and his availability.

I acknowledge the EPFL ACI team for the fabrication of all the PCB presented in this thesis. In particular I warmly thank José Garciacano, Jean-Marie Barblan and Jean-Marc Buchs for their constant help, interest and support that has enabled part of this study.

I also thank the EPFL CMI for their help in the different processes presented in this thesis and in particular Joffrey Pernollet and Cyrille Hibert.

I am also grateful to André Catana and Alberto Di Consiglio of the EPFL Technology Transfer Office for the continuous support and motivation they offered me.

A tender thanks to Andrea, who has always provided me with encouragements and help but most importantly supported me during those few years of thesis.

Finally but most importantly, I would like to thank my parents Chantal and Jean-Pierre for their unconditional love and support during my life. They also transmitted me the curiosity and determination that allowed me to follow this path. A special thank to my father who fabricated an important part of the setups used in this research and transmitted me his precious practical skills. I also thank my brother Nicolas for our complicity. To conclude, I dedicate posthumously the efforts and results of this thesis to my grand mother Evelyne and my grand father Alexandre who have been the best examples of fortitude and purposefulness, which has imprinted my character.

Content

Chapter 1 : Introduction.....	23
1.1 Single cell impedance spectroscopy	24
1.2 Thesis contribution & structure.....	28
1.2.1 Single cell isolation for cloning applications using impedance spectroscopy	28
1.2.2 Cost effective designs and fabrication processes allowing to produce disposable flow cytometers.....	28
1.2.3 A non-invasive cell biosensor based on impedance spectroscopy	29
Chapter 2 : Single Cell Dispensing Using a Pipette Tip Integrating an Impedance Sensor	31
2.1 Introduction.....	32
2.1.1 Need for single cell isolation	32
2.1.2 Specifications	33
2.1.3 From closed chip to open space microfluidic	33
2.2 Design of the single cell dispensing tool	35
2.2.1 The sensing tip.....	35
2.2.2 Instrumented pipette	36
2.2.3 Dispensing workflow	38
2.2.4 Sensing tip fabrication process.....	40
2.2.5 Fabrication costs	42
2.2.6 Sensing tip modeling	43

2.3 Results	46
2.3.1 Sensing tip characterization.....	46
2.3.1.1 Impedance & potential distribution.....	46
2.3.1.2 Sensing tip impedance spectra.....	46
2.3.1.3 Aperture size and total impedance magnitude.....	47
2.3.1.4 Particle detection and sensitivity to particle size	48
2.3.1.5 Noise analysis & theoretical smallest particle detectable	51
2.3.1.6 Effect of the membrane thickness on the particle detection and size sensitivity	56
2.3.2 Fabrication constraints allowing cost effective design	59
2.3.2.1 Effect of the electrodes placement	59
2.3.2.2 Effect of the aperture size	60
2.3.2.3 Summary on fabrication tolerances.....	61
2.3.3 Sensing tip fluidic behavior.....	63
2.3.3.1 Fluidic characterization.....	63
2.3.3.2 Fluidic Model	65
2.3.3.3 Model validation.....	68
2.3.3.4 Model parameters for cell dispensing	69
2.3.4 Single particle dispensing validation	74
2.3.5 Single particle dispensing reliability and plate filling rate	75
2.3.6 Cell viability	78
2.4 Discussion.....	81

Chapter 3 : Cost Effective and Large Scale Manufacturing of Flow Cytometers.....	85
3.1 Introduction.....	86
3.2 Materials & methods.....	89
3.3 Results	90
3.3.1 PCB production line fabrication capabilities.....	90
3.3.2 Electrodes array probe fabrication and characterization	92
3.3.3 Cell toxicity assay with the electrodes array probe	94
3.3.4 PCB made flow cytometers and beads detection	98
3.3.4.1 Liquid electrode design	98
3.3.4.2 Coulter counter design.....	100
3.3.5 Performances & Comparison with previous designs	102
3.3.6 Cost analysis	105
3.4 Discussion.....	107
3.4.1 PCB fabrication processes for BioMEMS and flow cytometers.....	107
3.4.2 Planar flow cytometers.....	109
Chapter 4 : Impedance Spectroscopy for Active Cells Analysis	111
4.1 Introduction.....	112
4.2 Models for non-invasive measurements of electrically active cells	116
4.2.1 Discrete impedance membrane model	116
4.2.2 Cell impedance segmentation to access local membrane parameters.....	118
4.2.3 Spatiotemporal ion distribution model for electrically active cells.....	122

4.2.3.1	Model & assumptions	123
4.2.3.2	Numerical solving	127
4.2.3.3	Resolutions.....	129
4.2.3.4	Ions concentration.....	131
4.2.3.5	Charge & electric field at the membrane.....	132
4.2.3.6	Trans-membrane potential	132
4.2.4	Non-invasive measurements of ion channel permeability	133
4.2.4.1	Trans-membrane potential measurements	133
4.2.4.2	Charge & electrical field measurements.....	133
4.2.4.3	Impedance measurements.....	134
4.3	Impedance spectroscopy on <i>Xenopus laevis</i> oocytes for ion channel modulation investigations.....	135
4.3.1	Material & methods	135
4.3.1.1	<i>Xenopus laevis</i> oocytes	135
4.3.1.2	Injection & preparation	136
4.3.2	Setup design and model.....	137
4.3.2.1	Transoocyte chamber design & fabrication	137
4.3.2.2	Electrical equivalent model of an oocyte in the transoocyte chamber.....	138
4.3.3	Results.....	142
4.3.3.1	Oocytes impedance spectra	142
4.3.3.2	Ion channels modulation spectra.....	143
4.3.3.3	Ion channels expression spectra	145

4.3.3.4 Single frequency impedance measurements of ion channels modulation for integrated systems.....	146
4.3.4 Strategies to increase the seal	149
4.3.4.1 Sucrose perfusion chamber	149
4.3.4.2 Localized impedance measurement with a microelectrode	152
4.4 Discussion.....	154
Chapter 5 : Conclusion & Future Work.....	157
5.1 Single cell dispensing using a pipette tip integrating an impedance sensor	158
5.2 Cost effective and large scale manufacturing of flow cytometers	159
5.3 Impedance spectroscopy for active cells analysis	160
Chapter 6 : References	163
Chapter 7 : Appendix.....	177
7.1 Hair follicle morphogenetic assay using the instrumented pipette. Figure reprinted from Georges Muller PhD thesis.....	178
7.2 Python code: Sensing tip analytical model	179
7.3 Matlab code: Spatiotemporal ion distribution model for electrically active cells	184

List of figures

<i>Figure 1.1 The original Coulter counter</i>	25
<i>Figure 1.2 : Concept of impedance spectroscopy with different Coulter counter embodiments</i>	26
<i>Figure 1.3 : Two embodiments of microfabricated impedance spectroscopy flow cytometers</i>	27
<i>Figure 2.1 : Design and implementation of a cell sensor integrated on a pipette tip</i>	36
<i>Figure 2.2 : Instrumentation for single cell dispensing</i>	37
<i>Figure 2.3 : Lock-in demodulation principle used for the sensing tip impedance measurement</i>	38
<i>Figure 2.4 : Workflow for single cell dispensing with the instrumented pipette and the sensing tip</i>	39
<i>Figure 2.5 : Process flow for the sensing tip fabrication</i>	41
<i>Figure 2.6 : Illustration of the sensing tip batch fabrication process capability.</i>	42
<i>Figure 2.7 : Sketch of the sensing tip segmentation with dimensions defining the analytical model</i>	44
<i>Figure 2.8 : Result of analytical model and experimental characterization of the sensing tip</i>	48
<i>Figure 2.9 : Sensing tip sensitivity to dielectric particle size</i>	50
<i>Figure 2.10 : Resistive bridge instrumentation allowing to measure the sensing tip impedance variation</i>	52
<i>Figure 2.11 : Minimal particles size detectable for a given aperture size</i>	53
<i>Figure 2.12 : Transimpedance amplifier instrumentation allowing to measure the sensing tip impedance</i>	54
<i>Figure 2.13 : Effect of the membrane thickness on the particle detection and size sensitivity</i>	58
<i>Figure 2.14 : Effect of the electrode placement</i>	60
<i>Figure 2.15 : Effect of the aperture diameter on the particle detection</i>	61
<i>Figure 2.16 : Sensing tip fluidic characterization with cycles of liquid aspiration and dispense</i>	65
<i>Figure 2.17 : Fluidic model of the sensing tip</i>	66
<i>Figure 2.18 : Fluidic model validation with liquid dispensing experiment</i>	69
<i>Figure 2.19 : Sketch illustrating the concept of particle escape distance</i>	71
<i>Figure 2.20 : Distance traveled by the particle when leaving the sensing tip</i>	72
<i>Figure 2.21 : Poisson distribution defining the average number of cell dispensed per well by serial dilution</i>	73
<i>Figure 2.22: Demonstration of the system capability to isolate single particle in wells</i>	75
<i>Figure 2.23 : Estimation of the electric field and shear stress applied on cells during dispensing</i>	79
<i>Figure 2.24 : Cell viability assay after cell dispensing performed with the instrumented pipette</i>	81
<i>Figure 3.1 : Fabrication process used for manufacturing BioMEMS using a PCB fabrication line</i>	89
<i>Figure 3.2: Fabrication capabilities of a standard PCB fabrication line used for BioMEMS applications</i>	92
<i>Figure 3.3 : Electrodes array probe</i>	94
<i>Figure 3.4 : Cell compatibility assay with PCB made test probes</i>	97
<i>Figure 3.5 : Liquid electrode flow cytometer</i>	100
<i>Figure 3.6 : PCB based Coulter counter</i>	102
<i>Figure 3.7 : Performances comparison between the different flow cytometer topologies</i>	105
<i>Figure 4.1 : The Hodgkin-Huxley model for cell membranes</i>	117
<i>Figure 4.2 : Nerve bundle recording</i>	119
<i>Figure 4.3 : Neuron recording with a MEA</i>	120
<i>Figure 4.4 : Torpedo electrocyte exhibiting a trans-cell voltage</i>	121
<i>Figure 4.5 : Generalized cell segmentation concept</i>	122

<i>Figure 4.6 : Ions distribution around the cell membrane</i>	123
<i>Figure 4.7 : Construction of the spatiotemporal ion distribution model</i>	124
<i>Figure 4.8 : Ion current between elements</i>	125
<i>Figure 4.9 : Resolutions of the spatiotemporal ion distribution model</i>	130
<i>Figure 4.10 : Xenopus laevis oocyte structure</i>	137
<i>Figure 4.11 : Transoocyte chamber for asymmetric impedance measurements on Xenopus laevis oocytes</i>	138
<i>Figure 4.12: Electrical equivalent model of an oocyte in the transoocyte chamber</i>	140
<i>Figure 4.13 : Xenopus laevis oocyte impedance spectra in the transoocyte chamber</i>	143
<i>Figure 4.14 : Ion channels modulation spectra</i>	145
<i>Figure 4.15 : Ion channels expression spectra</i>	146
<i>Figure 4.16 : Single frequency impedance measurements of ion channels modulation</i>	148
<i>Figure 4.17 : Sucrose perfusion chamber</i>	151
<i>Figure 4.18 : Custom-made microelectrode</i>	152
<i>Figure 4.19 : Localized impedance measurement</i>	154
<i>Figure 7.1 : Hair follicle morphogenetic assay</i>	178

List of tables

<i>Table 2.1 : Theoretical and experimental noise of the different impedance measurement instrumentations</i>	56
<i>Table 2.2 : Summary on the sensing tip design parameter tolerances</i>	63
<i>Table 2.3 : Single particle dispensing reliability and plate filling rate</i>	77
<i>Table 2.4 : Maximal shear stress in the sensing tip and FACS during operations</i>	79
<i>Table 2.5 : Fabrication costs of the sensing tip</i>	42
<i>Table 3.1 : Performances comparison of the different flow cytometer topologies</i>	104
<i>Table 3.2 : Fabrication costs of the different flowcytometer topology using different fabrication processes</i>	106
<i>Table 4.1 : Parameters selected for the spatiotemporal ion distribution model</i>	127
<i>Table 4.2 : Selected values for the transoocyte chamber impedance model</i>	140

Abbreviations

3D	Three-dimensional
AC	Alternating Current
Au	Gold
BioFET	Field Effect Transistor based Biosensor
BioMEMS	Biomedical/Biological MicroElectroMechanical Systems
Cl	Chloride
CMOS	Complementary Metal Oxide Semiconductor
CNC	Computer Numeric Control
CPE	Constant Phase Element
Cu	Copper
CVD	Chemical Vapor Deposition
DMEM	Dulbecco/Vogt modified Eagle's Minimal Essential Medium
DPBS	Dulbecco's Phosphate-Buffered Saline
ENaC	Epithelial Sodium Channel
FACS	Fluorescent-Activated Cell Sorter
FBS	Fetal bovine serum
GFP	Green Fluorescent Protein
HEPES	4-(2-hydroxyethyl)-1-piperazineethanesulfonic acid (chemical buffering agent)
IC	Integrated Circuit
ISFET	Ion Sensitive Field Effect Transistor
K	Potassium
LCP	Liquid Cristal Polymer
MBS	Modified Barth's Saline
MEA	MultiElectrodes Array
MEMS	MicroElectroMechanical Systems
Na	Sodium
NFR	Normal Frog Ringier
NMDG	N-Methyl-D-glucamin
PBS	Phosphate-Buffered Saline
PC	Personal Computer
PCB	Printed Circuit Board
PI	Polyimide
POM	Polyoxymethylene
RCT	Charge Transfer Resistance
RI	Riston
SEM	Scanning Electron Microscope
TEVC	Two Electrode Voltage Clamp

Chapter 1 : Introduction

“Biology is not simply writing information; it is doing something about it. A biological system can be exceedingly small. Many of the cells are very tiny, but they are very active; they manufacture various substances; they walk around; they wiggle; and they do all kinds of marvelous things – all on a very small scale. Also, they store information. Consider the possibility that we too can make a thing very small which does what we want – that we can manufacture an object that maneuvers at that level!”

Richard P. Feynman

1.1 Single cell impedance spectroscopy

Today, flow cytometry is ubiquitous in biology with modern Fluorescent-Activated Cell Sorting instruments (FACS) that have opened the way to new therapeutic and clinical applications (Tung, 2007; Malmed, 2001; Ormerod, 2008). Amongst many examples, FACS are used for analysis of leukaemias and lymphomas (Craig, 2008), HIV and immunodeficiency disease diagnosis (Mandy, 2002), solid organ transplantation and postoperative monitoring (Bray, 1994; Shanahan, 1997) and stem cell enumeration (Keeney, 1998). However, before the widespread use of optical detection, flow cytometry was rooted to impedance spectroscopy (Fulwyler, 1965). In the fifties, Wallace Coulter invented an instrument for detecting and counting particles suspended in a conductive liquid (Coulter, patent, 1953; Robinson, 2013).

The principle of the Coulter counter consists in passing particles through an aperture while applying an electric current between the two compartments, which results in an impedance change depending on the particle volume. To apply the electric current, one electrode is placed in each of the compartments separated by the aperture as shown in Figure 1.1 a). When a particle passes the aperture, its section is diminished leading to the decrease of the electrical current and increase of impedance (Figure 1.1 b). The electrical current is measured and the current drop detected to count the particle passage. The bigger the particle passing the aperture, the larger the current drop. According to this principle, the Coulter counter is also capable of characterizing the particle size.

This simple system was initially embodied as a glass tube containing a tiny aperture on its side. The glass tube was plunged in a vessel containing the sample to be analyzed. One electrode was placed in the glass tube and the other in the sample vessel to apply the potential difference. Using a tiny hydrostatic pressure caused by a difference in liquid height between the tube and the vessel, particles were flown through the aperture (Figure 1.1 c). At that time, this instrument (Figure 1.1 d) revolutionized hematology and became the gold standard for automated blood cells counting and sizing with the ability to count up to 6000 individual cells per second (Coulter, 1956). This system allowed to perform cell counting 100 times faster than the microscopy based blood cell counting method. Today, a large part of hematology analyzers is still based on the Coulter counter principle (Kim, 2008).

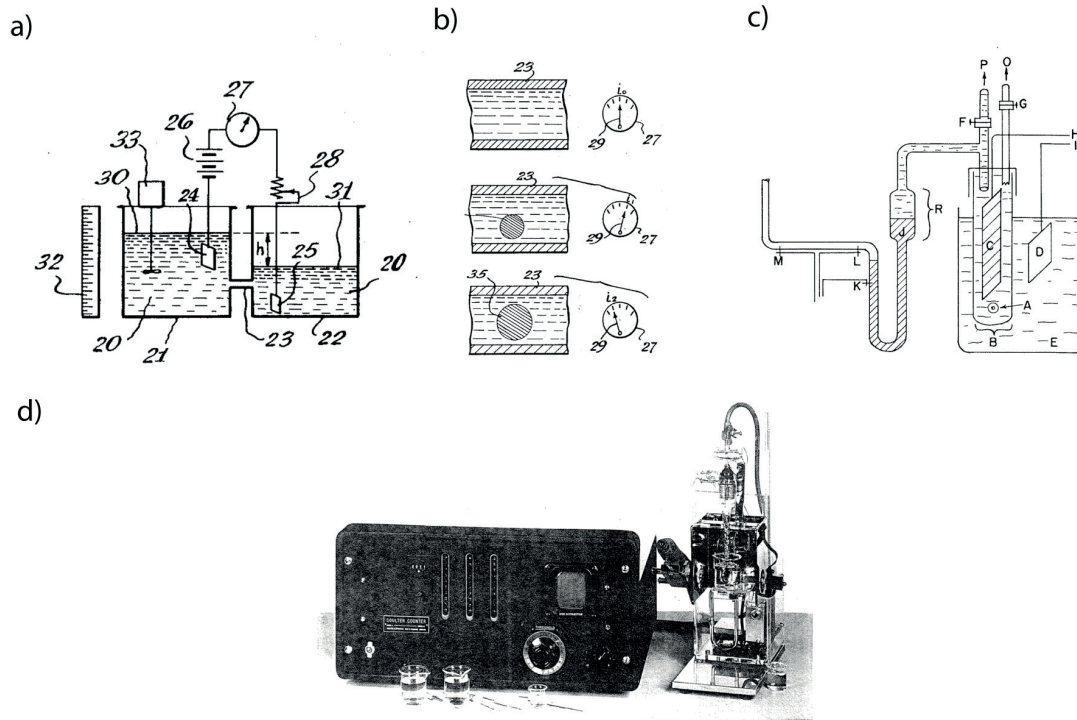


Figure 1.1 The original Coulter counter. a) Working principle and structure with two compartments separated by an aperture b) Particle in the aperture inducing a current decrease c) & d) First realization of the Coulter counter. Reprinted from (Coulter, 1953) and (Coulter, 1956)

A few years later, Wallace Coulter proposed to improve its instrument by applying a high frequency excitation signal in addition to the continuous excitation to measure both the resistive and reactive changes in the current modulation occurring when a biological cell passes the aperture (Figure 1.2 a). This provided the ability to classify cells on parameter such as their electric capacity that is defined by their membrane thickness and surface (Coulter, 1970; Coulter, 1988). In essence, the concept of single cell impedance spectroscopy was born with the idea of applying excitations at different frequency to retrieve information on the dielectric structure of the cell.

However, at that time, the initial Coulter counter design was suffering from major limitations to apply high frequency excitation on the cell. Essentially, the large capacitive losses in the wall separating the two chamber of the Coulter counter were preventing the use of high frequencies. Coulter proposed different embodiments to circumvent those limitations. One consisted of a gradual increase of the wall thickness around the aperture in order to reduce the stray capacitance as shown in Figure 1.2 b) (Coulter, 1973). He also

proposed different counter embodiments that are now described as micromachined impedance spectroscopy flow cytometers. One embodiment consisted in two microelectrodes facing each other in a microchannel as shown in Figure 1.2 c). Yet another embodiment consisted in a monopolar microelectrode sitting in a microchannel as shown in Figure 1.2 d). However, microfabrication capabilities were limited making those different designs difficult to realize. Consequently and amongst other reasons, the developments of instruments for cell analysis and population differentiation took another pass with optical detection techniques (Hulett, 1969) leaving behind the beauty of the Coulter counter with its extremely simple structure and its real label-free analytical principle.

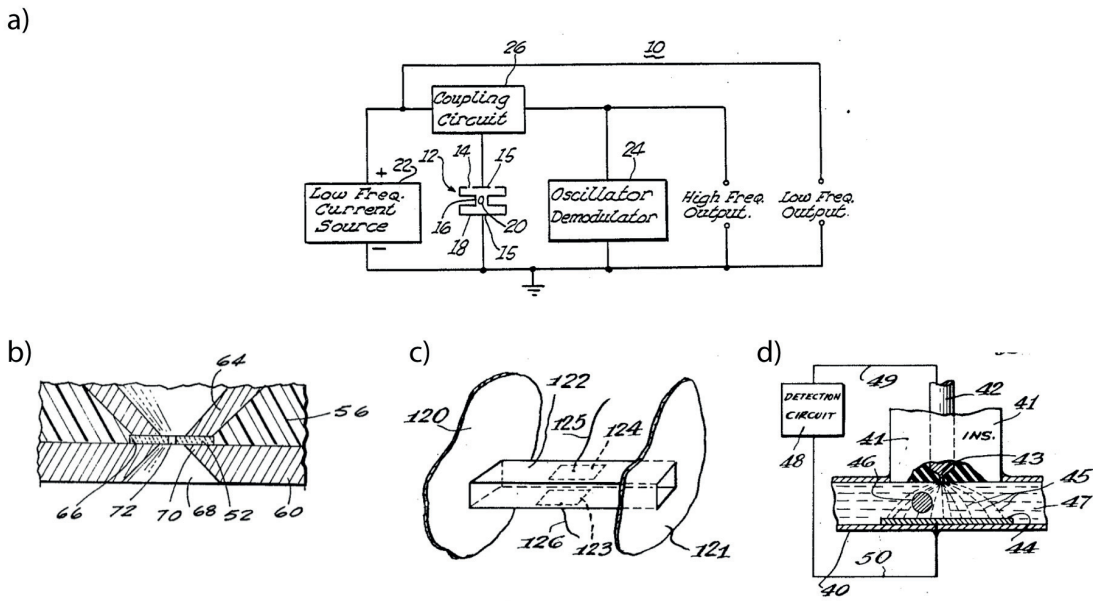


Figure 1.2 : Concept of impedance spectroscopy with different Coulter counter embodiments allowing for the use of high frequency excitations. a) Measurement principle with two excitation frequencies b) Coulter counter embodiment with the vessel thickening around the aperture. c) Embodiment with microelectrodes facing each others in a microfluidic channel, d) Embodiment with a monopolar microelectrode in a microfluidic channel. Adapted from (Coulter, 1949), (Coulter, 1970) and (Coulter, 1973).

Thanks to sustained efforts in microelectronic development and semiconductor miniaturization (Moore, 1965), important advances in microfabrication techniques (Madou, 1997) allowed to produce micromachined impedance spectroscopy flow cytometers (Ayliffe, 1999) (Gawad, 2001) as illustrated in Figure 1.3. With such miniaturized technologies and the low amount of liquid volume handled, micromachined flow cytometers were exhibiting a low stray capacitance compared to the initial Coulter counter embodiment. Consequently,

researchers demonstrated the detection and classification of latex beads, ghost cell, human polymorphonuclear leukocytes and erythrocytes based on their dielectric structure using impedance spectroscopy.

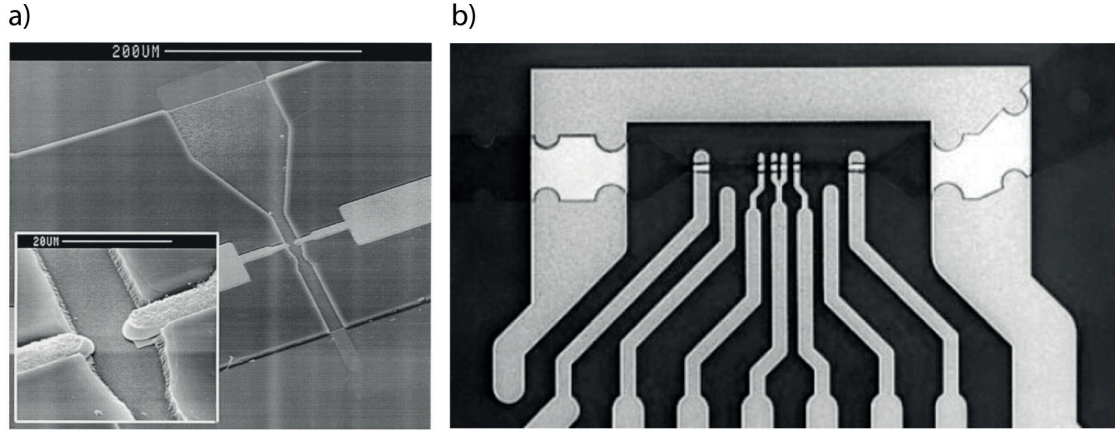


Figure 1.3 : Two embodiments of microfabricated impedance spectroscopy flow cytometers. Reprinted from (Ayliffe, 1999) and (Gawad, 2001).

Later, researchers demonstrated the use of micromachined impedance spectroscopy flow cytometers for the leukocyte differentiation and clustering in monocytes, neutrophils and T-lymphocytes sub-population based on the cell dielectric properties (Holmes, 2009; Holmes, 2010). Similarly, Kuttel et al. (Kuttel, 2007) showed the ability to use micromachined impedance spectroscopy flow cytometers to detect *Babesia bovis* infected red blood cell. Cell viability was also shown to be detectable based on the dielectric properties of the cell because of the impact on the cell membrane capacitance after cell apoptosis (Wang, 2002).

These different publications confirmed the potential of micromachined impedance spectroscopy flow cytometers for label-free and non-invasive cell characterization based on their dielectric properties and morphology unlike FACS that require fluorescent tagging of the cells (Gawad, 2004; Sun, 2010; Cheung, 2005; Morgan, 2006; Sun, 2006; Sun, 2007; Cheung, 2010).

However, none of those proposed solutions were designed to allow isolation and retrieval of a specific cell detected during the population analysis (Chen, 2012).

1.2 Thesis contribution & structure

This thesis aims to focus on single cell impedance spectroscopy and covers three specific problematics. First, the use of single cell impedance spectroscopy to isolate and retrieve rare and precious cells. To do so, we propose to revisit the design of the Coulter counter chosen for of its inherent simplicity. Second, cost effective designs and fabrication processes of flow cytometers allowing single-cell analyzing and dispensing are investigated to allow the fabrication of disposable devices required to be compatible with cell culture. Third and finally, the analytical capability of impedance spectroscopy is further explored with detection of cell parameters such as ligand-gated ion channel activity.

1.2.1 Single cell isolation for cloning applications using impedance spectroscopy

The first problematic described in this thesis is related to the use of cells to produce recombinant proteins and every similar processes in which the establishment of clones are required. Bioprocesses for recombinant proteins production cover many complex aspects ranging from the cell substrate genomic modification to the extraction and purification of proteins. However, all those bioprocesses have in common the isolation of single cell required initially for the cell line establishment. The scope of this first part of the thesis is restricted to the problematic of single cell isolation. A method for single cell isolation based on impedance spectroscopy is proposed with emphasis on its disposable and sterile aspect suited for cell culture required to perform cell cloning. The approach consists of building a single-cell dispensing tool based on the Coulter counter principle on an existing disposable and gold-standard pipette tip. Challenges are to microfabricate a cheap and disposable cell sensor on a 3D object.

1.2.2 Cost effective designs and fabrication processes allowing to produce disposable flow cytometers

The second part of this thesis consists of translating the concept of disposable, sterile and low-cost single cell dispensing system on a standard planar microfabrication technology. The use of planar microfabrication technology allows to integrate more complex features on

the dispensing tool. However, as a disposable tool, it needs to be produced at low cost and in a high volume. A planar fabrication method based on conventional PCB manufacturing, a standard and established industrial method, is studied to produce low cost flow cytometers in high volume.

1.2.3 A non-invasive cell biosensor based on impedance spectroscopy

The third part of the thesis is dedicated to further exploring cell parameters that can be observed using impedance spectroscopy by focusing on detecting cell activity with namely the monitoring of ligand-gated ion channel opening. It focuses on the investigation of ligand-gated ion channel permeability modulation using impedance spectroscopy. Cellular mechanisms such as ion flow through activated ion channel are reacting very specifically and rapidly to the binding of a ligand molecule. Shear *et al.* (Shear, 1995) demonstrated the interest of this principle to develop biosensors offering high sensitivity selectivity and bandwidth performances. According to this concept, cells act as transducers between the chemical compound to be detected and ion flux through cell membrane channels. Using the cell as transducer to make a biosensor requires measuring the electrophysiological state of the cell. One engineering challenge is to develop a non-invasive measurement method allowing long-term measurements as well as automated and sufficiently miniaturized for its integration as a sensor. In the context of this thesis, the use of impedance spectroscopy is investigated for this aim with an emphasis on the non-invasive character of the method.

Chapter 2: Single Cell Dispensing Using a Pipette Tip Integrating an Impedance Sensor

This chapter is adapted from the following work and publications:

Bonzon, D., Muller, G., Barrandon, Y., & Renaud, P. (2014). Single-cell dispensing on a pipette. *Nanobiotech Conference, Montreux, Switzerland*

Bonzon, D., Muller, G. H., Renaud, P., & Barrandon, Y. (2014). Sensing tip with electrical impedance sensor. *Patent application WO 2015056176 A1*

Bonzon, D., Muller, G., Barrandon, Y., & Renaud, P. (2015). Microfabrication on a pipette tip for single cell dispensing. *Nanobiotech Conference, Montreux, Switzerland*

Bonzon, D., Muller, G. H., Renaud, P., Barrandon, Y., Bureau, J.-B., & Béguin, S. (2016). Devices, systems and methods for dispensing and analysing particles. *Patent application WO 2016166729 A1*

Bonzon, D., Bonzon, J.-P., Muller, G., Bureau, J.-B., Barrandon, Y., Renaud, P. (2017). Tip connector for fluidic and electrical connection. *Patent application PCT/IB2017/052088*

2.1 Introduction

2.1.1 Need for single cell isolation

Today, in the pharmaceutical industry, four of the five best selling drugs are produced using a bioprocess (Philippidis, 2015; Huggett, 2012). A bioprocess consists of using a cell substrate that is genetically modified to produce a drug under the form of a recombinant protein product (Kantardjieff, 2013). Because of the safety and quality issues related to drug production and to avoid heterogeneity in the expression, regulation authorities requires that each cell substrate derives from a single cell progenitor (ICH, 1997). Furthermore, the single cell isolation procedure needs to be fully documented with proof or appropriate statistic of single cell isolation evidence (WHO, 2014). The selection step of the cell substrate consists of isolating each genetically modified cell, expanding them in culture separately and screening their protein production to select for the best producing candidate (Wurm, 2004). In this context, the gold-standard method used to isolate single cells is currently serial dilution (Fuller, 2001). This technique consists of pipetting a given volume containing on average only one cell per dispensed aliquot according to Poisson distribution. To lower the risk of a clone being derived from multiple cells, each of the clones are cultured for two weeks, diluted and sub-cloned at least two to three times, hence turning this isolation step into a long process lasting for several weeks.

To avoid sub-cloning steps, several methods and devices were developed to perform single cell cloning in one step. One method is the cell picking. Under a microscope, a single cell is selected and aspirated from a dish using a capillary terminated with a diameter slightly bigger than a cell. This single cell of interest is then simply rejected in another container used for the culture (Fröhlich, 2000; Barrandon, 1985). However, these techniques require technical skills, are prone to contamination and offer a limited throughput. Many different techniques allows automatizing the cell picking including the handling of cells using optical, dielectrophoretic or acoustic tweezers (Askin, 1987; Thomas, 2009; Shi, 2009) but involve complex engineering implementations.

Different microfluidic solutions enable single cell isolation to perform single cell genomic or proteomic assays. Well known examples are multichambers allowing multiplexed fluidic addressing capability to capture single cells, perfuse them with different conditions and to

perform end-point assays on the cells or their product (Di Carlo, 2006; Kalisky, 2011; Kalisky, 2011). However, none of those devices permits for direct and easy retrieval of the cell enabling culture or further assays.

Finally, Fluorescent-Activated Cell Sorters (FACS) (Shapiro, 2003; Shapiro, 2004), even though initially designed to analyze and separate cells into sub-populations, are now capable of isolating single cell into wells in modern versions (Evans, 2015; Vermeulen, 2008). However, the main limitations of FACS are inherent from their long section of tubing imposing large dead volumes that make the instrument difficult to sterilize. Additionally, because of these dead volumes, the tool cannot be used with a limited amount of cells in input. All those different techniques with their respective advantages and limitations are well described and compared by Gross and colleagues. (Gross, 2015).

These considerations support the need of a simple tool that specifically answer the problem of single cell isolation with traceability for processes where the single cell is going to be further manipulated and cultivated.

2.1.2 Specifications

The ideal solution should allow for single cell isolation without risk of doublet. In order to comply with regulation agencies, the method should provide single cell isolation evidence for traceability. The device containing the cells sample should be disposable to avoid cross contamination between the different dispensing procedures. Consequently the production process of the device requires to be cost-effective. The procedure should be sterile to avoid bacterial and viral contamination. Finally, the tool should preserve the cell viability and functionality to enable the cell culture for recombinant protein production or other similar processes.

2.1.3 From closed chip to open space microfluidic

As introduced early in this thesis (§1.1), the goal of most impedance spectroscopy based flow cytometers developed so far was the single cell analysis and populations differentiation. As a consequence, they all consisted of microchips embedding sealed channels to convey the cell to the cytometer sensitive volume (Gawad, 2001; Holmes, 2010; Cheung Review, 2010; Chen, 2012). With such embodiment, the main limitations

encountered are the difficulties to introduce the sample, the risk of channel clogging with dust or bubble formation. More importantly, these closed microfluidic chips use channels to connect the cell analysis sensitive volume to the chip outlets. Similarly, tubing is required to connect the microchip to the macro world. Those microfluidic channels and tubing impose important dead volumes compared to the cell size and the flow cytometer sensitive volume. Because of those dead volumes combined with the risk of cell capture by surfaces, the particles order is likely to be different between their passage in the flow cytometer sensitive volume and their escape of the tubing. Similarly, because of the cell-surface interaction, not every cell will leave the chip and the tubing. This prevents the ability to retrieve with confidence a specific single cell that has been analyzed in the chip. This also prevents to analyze and retrieve a sample composed of a limited number of scarce cells. If those solutions were well suited for single cell analysis, they are not capable of single cell isolation.

Different solutions inspired from inkjet printing were proposed to allow the dispensing of single cell (Tornay, 2007; Yusof, 2011; Gross, 2013; Schoendube, 2015). However, solutions involving droplet formation present important limitations such as the risk of satellites formation and drying effects linked to the complexity of droplet ejection physics. Moreover, the small size of the droplet coupled with thermal and pressure constraints encountered during the flight might induce important changes of the cell environment to be avoided for fragile cells or proteins. Based on similar considerations, Kaigala *et al.* introduced the concept of open space microfluidic (Kaigala, 2011; Kaigala, 2012), circumventing the need of a closed microfluidic chip and eliminating the related drawbacks. The principle is based on a hydrodynamic confinement of liquid at the end of a vertical microfluidic probe. With the ability to interact locally with a biological sample in the open space, they demonstrated a large panel of applications such as the localized immunochemistry treatment of biological sample (Lovchik, 2012).

The problem of single cell dispensing studied in this thesis imposes similar requirements. The cell environment should be minimally disrupted and immersing a probe in a solution is very close to standard biologists pipetting habits. More importantly, placing the flow cytometer sensitive volume at the boundary between the device containing the cell and the open space allows detecting, analyzing and simultaneously isolating with confidence a single cell escaping the device.

2.2 Design of the single cell dispensing tool

A sensing tip for single cell detection and a corresponding instrumented pipette for single cell dispensing are presented in this section.

2.2.1 The sensing tip

The cell sensor is incorporated in a standard and commercially available tip that is disposable and made of standard material as shown in Figure 2.1. It allows compatibility with cells and the culture process. To perform the dispensing function, the detected cells should leave the tip with no risk of being trapped in dead volume after detection as discussed in the previous section (§2.1.3). In this regards, the integrated cell sensor is built as the last interface of the tip. The cell sensor is designed according to a Coulter counter topology introduced earlier (§1.1)(Coulter, 1953; Coulter, 1956; Robinson, 2013). This cell detection principle is simple and particularly well suited for single cell dispensing as it is only composed of a membrane containing an aperture as well as an inner and outer electrodes as shown in Figure 2.1 b). One compartment of the Coulter counter consists of the tip inside volume where an inner electrode is inserted in the tip. The other compartment consists of the well in which the tip is immersed to perform the dispensing. The outer electrode is deposited on the tip external surface. With this arrangement, the membrane containing the aperture and defining the particle sensitive volume is effectively superimposed with the tip external boundary.

Moreover, unlike microfabricated channel-based flow cytometer chips (Ayliffe, 1999; Gawad, 2001), the Coulter counter topology is not sensitive to electrode placement as only the aperture shape and diameter defines the sensitive area. Consequently, this Coulter counter embodiment allows a facile fabrication on 3D objects with no photolithography required and results in a possible cost effective fabrication of a cell sensor on an existing pipette tip as shown in Figure 2.1 c).

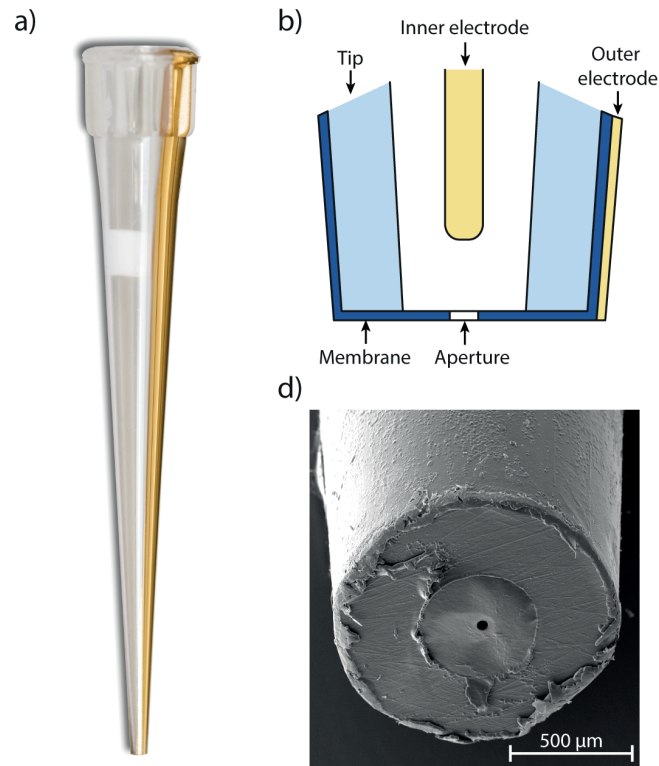


Figure 2.1 : Design and implementation of a cell sensor integrated on a pipette tip a) Picture of sensing tip used for single cell dispensing b) Design of a Coulter counter integrated on standard pipette tip consisting of a membrane closing the tip with an aperture and two electrodes inside and outside the tip allowing to detect and dispense single particles. c) Electron microscopy of the fabricated sensing tip showing the Coulter counter aperture.

2.2.2 Instrumented pipette

To increase acceptance, the tool is embodied in a pipette form showed in Figure 2.2 a), as commonly used by biologists and as already suggested by different work (Ayliffe, 2011; Zhang, 2014). In order to dispense a single cell when required, a system controller consisting of a Labview (National Instruments, US) algorithm running on a computer coordinates the full system composed of a flow controller, an impedance analyzer and the sensing tip as shown in Figure 2.2 b). In this version, the impedance analyzer is embedded in the pipette and the flow controller is an external instrument.

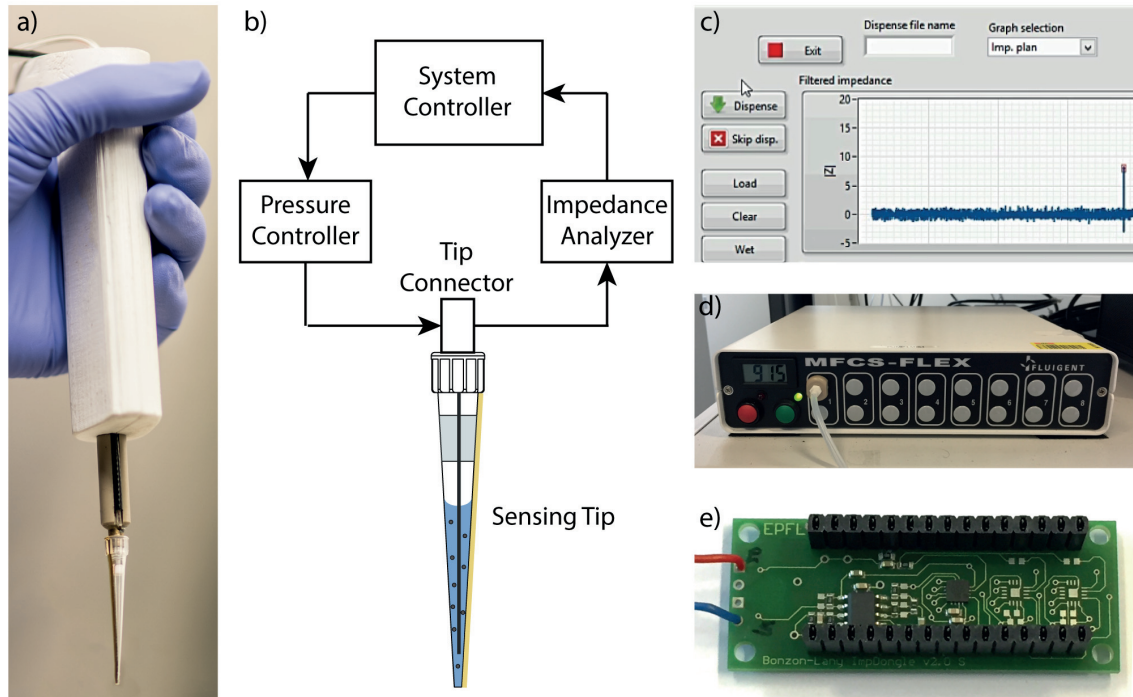


Figure 2.2 : Instrumentation for single cell dispensing. a) Single cell dispensing instrument embodied in a standard pipette shape. b) Overall block diagram of the instrument. c) User interface of the system controller d) Pressure controller e) Electronic circuit for impedance measurement.

The liquid aspiration and ejection is controlled using a pressure-based flow controller with a range of -25 mbar to 25 mbar (MFCS-EZ, Fluigent, FR) showed in Figure 2.2 d). The impedance of the sensing tip is measured according to a lock-in demodulation principle presented in Figure 2.3 and performed with an electronic circuit implementing an integrated lock-in demodulator (SI-QSD, Sensima, CH) interfaced with a microcontroller development kit (Nano, Arduino, IT) as shown in Figure 2.2 e). On the outer electrode, an excitation frequency of 49 kHz with amplitude of 0.5 V_{pp} is applied by the SI-QSD. From the inner electrode, the current is amplified using a transimpedance amplifier (OPA2350, TI, USA). The amplified current is measured and the impedance is determined using the acquisition, demodulation and filtering capability of the SI-QSD. Impedance measurements are then transmitted to the system controller at a sampling rate of 2.4 kHz with adequate low pass-filtering to adapt the bandwidth. Then a high pass filter at 6 Hz is applied on the signal in order to remove the slow variations of the signal baseline due to medium conductivity changes, aperture obstruction and other elements than cells passage.

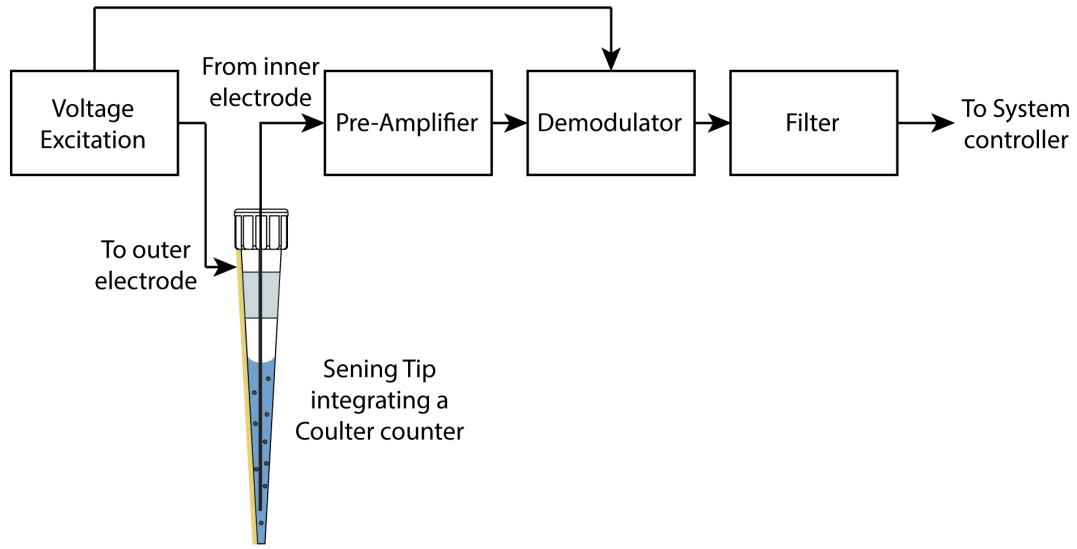


Figure 2.3 : Lock-in demodulation principle used for the sensing tip impedance measurement. An alternative voltage excitation is applied on the sensing tip external electrode. The current collected from the internal electrode is amplified and demodulated using the voltage excitation frequency and a low pass filter. The demodulated current is sent to the system controller.

2.2.3 Dispensing workflow

Before performing single cell dispensing, the sensing tip is loaded with a suspension of cells in a concentration range between 10^3 and 10^5 cells / mL.

When a single cell is required, the sensing tip is immersed in a well filled with media. A single cell dispense is triggered by the user on the system controller interface. Accordingly, the pressure-based flow controller applies a positive dispensing pressure P_D to flow the liquid containing the cells toward the outside of the sensing tip.

On the filtered impedance signal, impedance peaks representing cell passage are detected by the system controller. Each signal sample with an impedance peak magnitude $|\Delta Z|$ exceeding a threshold Z_{Th} trigs the peak detection. The peak is validated and considered as a cell passage when the signal magnitude returns below the threshold. Impedance peak height is then extracted to deduce the cell size. After a single cell has been detected, a delay t_d is waited to avoid the cell re-aspiration and then the flow is automatically stopped by applying the holding pressure P_H . Because a perfectly null pressure is not practically achievable, a slightly negative holding pressure P_H is applied to make sure no further cells will pass the

aperture. The tip is removed from the well and the impedance data of the corresponding well are saved for traceability purpose. All the procedure is triggered again when needed, to dispense the next single cell. This workflow is illustrated in Figure 2.4.

All the specific values discussed in the workflow such as dispensing pressure P_D , holding pressure P_H , time delay t_{delay} and detection threshold Z_{Th} are the object of explanations and details along the results part of this thesis (§2.3).

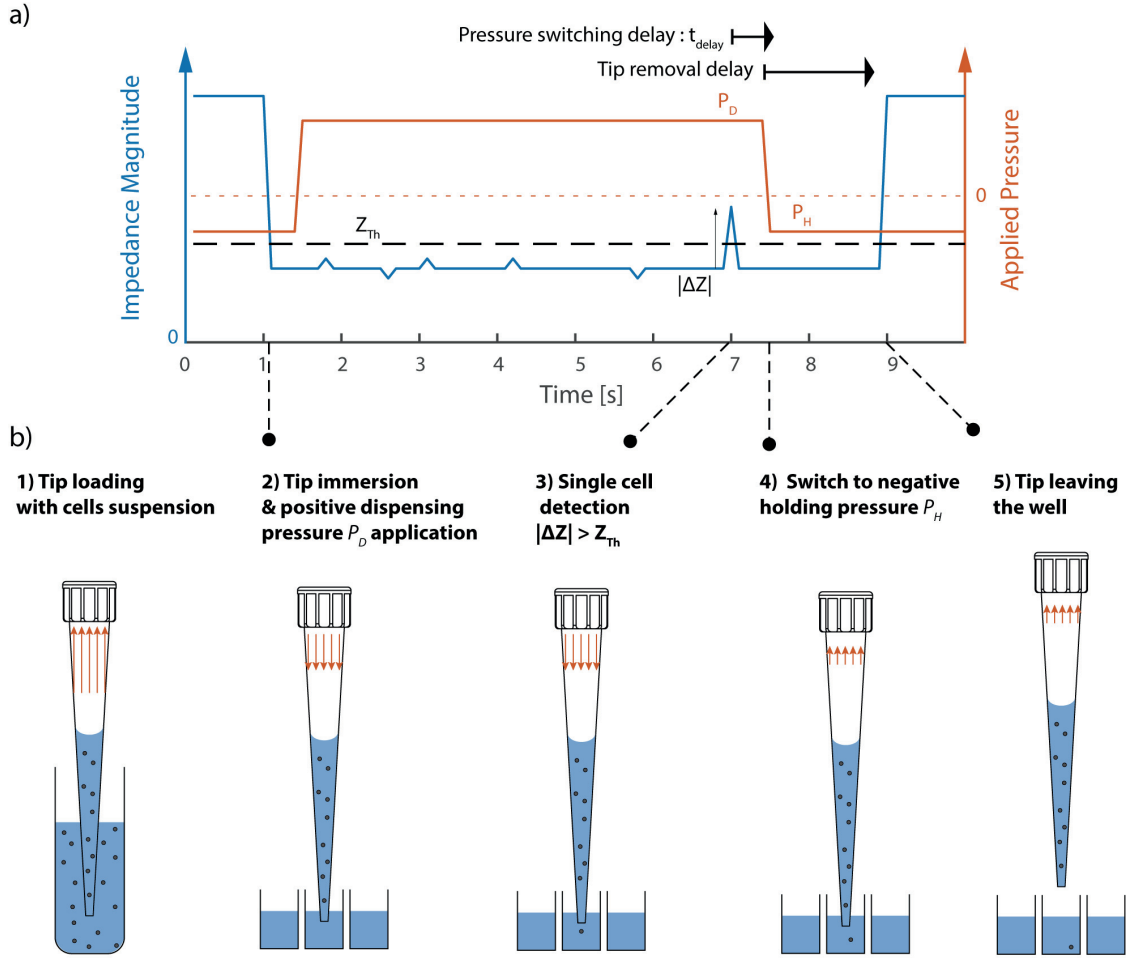


Figure 2.4 : Workflow for single cell dispensing with the instrumented pipette and the sensing tip. a) Shows the applied pressure timeline defined by the impedance measurement and b) shows the corresponding operations. 1) The sensing tip is loaded with a cell suspension, 2) The sensing tip is immersed in the well receiving the single cell leading to an impedance decrease and the dispensing pressure is applied. 3) When a single cell is detected with an impedance peak magnitude exceeding the detection threshold, 4) the pressure is switched to the holding pressure after the pressure switching delay preventing the cell re-aspiration. 5) Finally, the sensing tip is removed from the well containing the single cell and the impedance time trace is saved.

2.2.4 Sensing tip fabrication process

The sensing tip fabrication process starts with a 15 μm parylene C membrane deposition by Chemical Vapor Deposition (CVD) (C-30-S, Comelec, CH) on a commercial pipette tip (200 μl colorless, RatioLab, GE). This membrane deposition is performed in two steps. First, a sacrificial layer of parafilm (Parafilm M, Bemis, US) is applied on the tip opening. A 5 μm layer of parylene is then deposited on the sacrificial layer. Second, the sacrificial layer is removed, leaving a 5 μm floating membrane at the end of the pipette tip. A second 5 μm parylene layer deposition is performed on each side of the membrane to increase its thickness to 15 μm and to strengthen its anchoring. A 150 nm gold film is subsequently deposited on one side of the tip surface by evaporation (LAB 600H, Leybold Optics, CH) and using a shadow mask to define the outer electrode shape. The aperture is ablated using an excimer laser (LSV3, Optec, BE) on the previously deposited membrane. Different aperture diameters ranging from 30 μm to 45 μm are performed depending on the cell size to be measured. The inter electrode consists of a 300 μm diameter stainless steel wire (316L, Sadevinox, FR) inserted in the tip. A tip filter is inserted from the top of the tip to mechanically maintain the inner electrode and avoid aerosol contaminations. The entire fabricated sensing tip is then gamma sterilized. The full process flow is detailed in Figure 2.5.

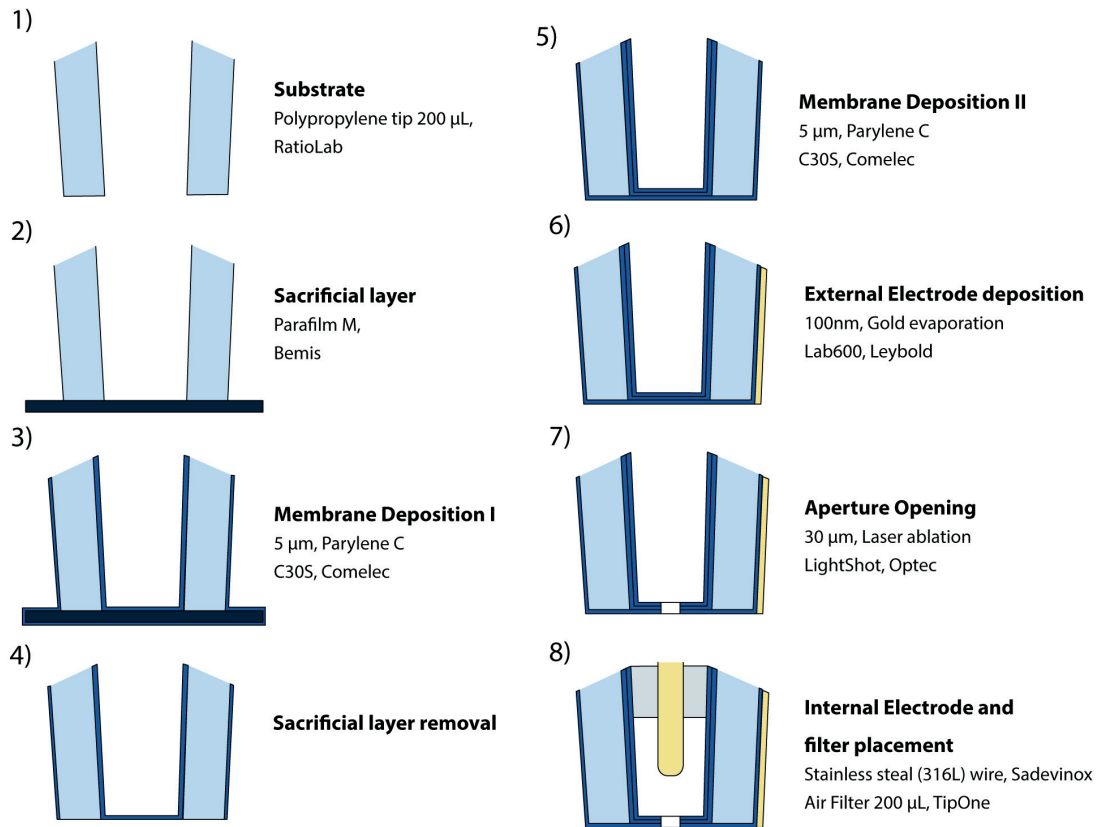


Figure 2.5 : Process flow for the sensing tip fabrication. 1) The process starts with a plastic pipette tip as substrate. 2) Parafilm is applied on the tip opening as sacrificial layer. 3) A first parylene C layer of 5 µm is deposited on the tip. 4) The sacrificial layer is removed. 5) A second parylene C layer of 5 µm is deposited on the tip. 6) The gold outer electrode is deposited. 7) The aperture is laser ablated. 8) A stainless steel wire serving as internal electrode is placed in the tip and holded in place with a tip air filter.

Figure 2.6 illustrates the batch production capability of this process required to produce a cost effective disposable device. Sensing tips were produced in batch of 96 or more parts.

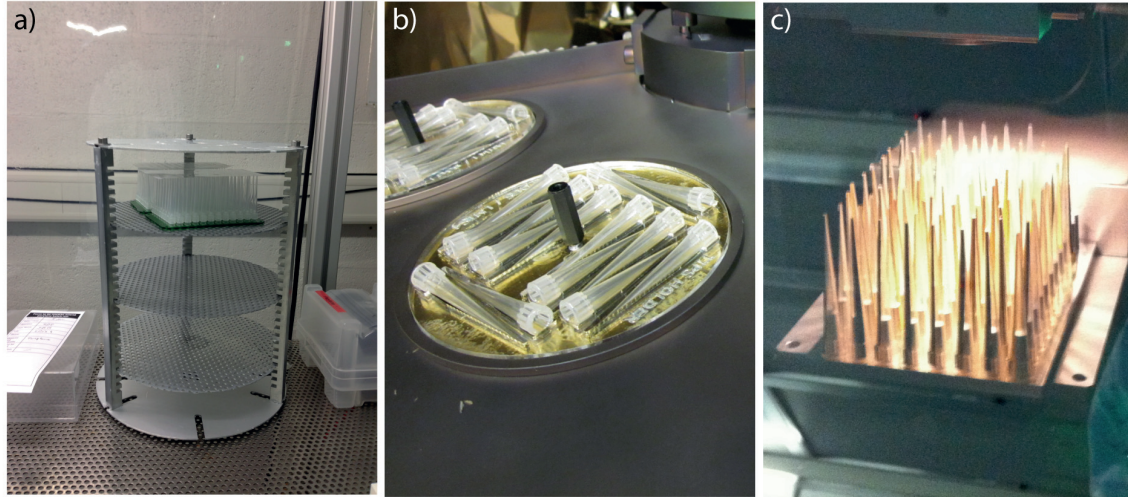


Figure 2.6 : Illustration of the sensing tip batch fabrication process capability. Some key steps of the process are shown; a) Tips ready for the parylene chemical vapor deposition. b) Gold electrode deposition by evaporation through a shadow mask. c) Aperture opening by laser ablation.

2.2.5 Fabrication costs

The fabrication costs of the sensing tip are evaluated in the academic context of this work. The material cost as well as the equipment and operator time is taken in account. Hourly rates for equipment and operator are assumed to be 80 CHF/h. The cost of each item is presented in Table 2.1 and results in a total sensing tip cost of 7.99 CHF per piece.

Table 2.1 : Fabrication costs of the sensing tip

	Material costs [CHF]	Equipment time [min]	Operator time [min]	Cost	Batch size	Price per tip
Plastic tip	CHF 0.02			CHF 0.02	1	CHF 0.02
Membrane (15 μ m parylene deposition)		360	45	CHF 540.00	576	CHF 0.94
External electrode (100 nm gold deposition)	CHF 66.00	60	20	CHF 172.67	96	CHF 1.80
Aperture (laser ablation)		120	120	CHF 320.00	96	CHF 3.33
Internal electrode (stainless steel electrode)	CHF 115		20	CHF 141.67	96	CHF 1.48
Filter	CHF 14.40		20	CHF 41.07	96	CHF 0.43
Total cost per sensing tip						CHF 7.99

2.2.6 Sensing tip modeling

This section presents a linear one-dimensional analytical model of the sensing tip impedance, including how it is influenced by particle passage. This model describes the real resistive part of the sensing tip impedance, neglecting membrane, tip, electrode and stray capacitances. It assumes that the impedance measurement of the instrumented pipette are performed in the resistive plateau frequency range. This model approximates the electrical resistance in infinitesimal sections along the sensing tip axis using resistivity law for the bulk contribution and taking into account the spreading resistance in close proximity of the sensing tip aperture. It is assumed that the sensing tip contains a liquid of resistivity $\rho = 0.65 \Omega \text{ m}$ (DPBS 1x, Sigma Aldrich, US) and is immersed in this same liquid.

The model is segmented in 4 sub-domains corresponding to the pipette geometry as shown in Figure 2.7. The first sub-domain starts at $-\frac{D_e}{2}$ that is assumed to be an equipotential given by the outer electrode and ends at the aperture entrance. This sub-domain represents the space outside the sensing tip, where only the spreading resistance contribution is relevant. The second sub-domain corresponds to the space inside the aperture, which is a cylinder of diameter d and length e along the x axis, where the electrical resistance is given by resistivity law of bulk solution. The third sub-domain corresponds to the portion of the conical part of the sensing tip situated between the aperture and the inner electrode at distance l . In this sub-domain, the value of the electrical resistance is approximated to either the value given by the resistivity law or the value of the spreading resistance, depending on the one that has the highest value. This allows taking in account the spreading resistance in close proximity of the aperture and the bulk solution resistance further away. Finally, the fourth sub-domain is the part of the tip of total length L where the inner electrode is present. In this sub-domain, the electrical resistance is assumed to be zero, as the resistivity of the metal is very low compared to that of the liquid medium contained in the tip.

In every sub-domain, the effective section is corrected by subtracting the particle section $S_{particle}$ obstructing it if a particle is presents. The particle is assumed to be a sphere of perfect dielectric material, with no current flowing through it. Equation 1 describes the infinitesimal electrical resistance dR for each infinitesimal section dx along the pipette length.

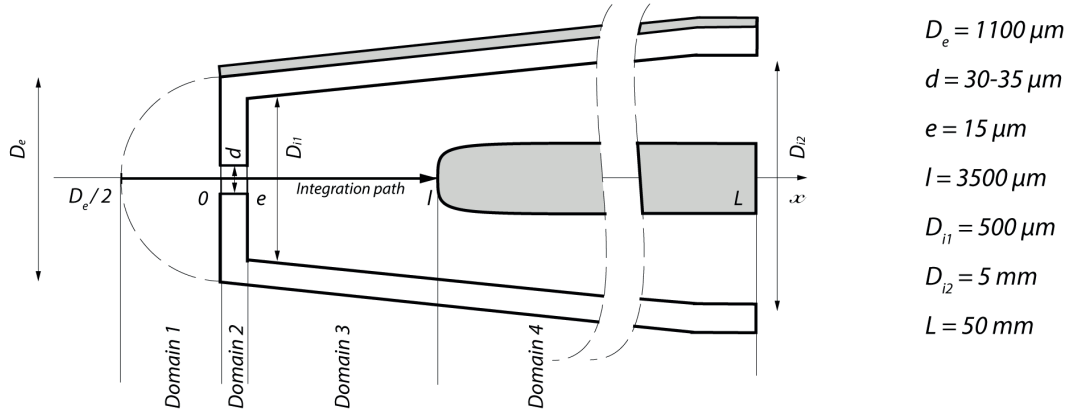


Figure 2.7 : Sketch of the sensing tip segmentation with dimensions defining the analytical model. Abbreviation are; D_e : Distal external tip diameter), d : Aperture diameter, e : membrane thickness, l : Membrane-electrode distance, D_{i1} : Distal inner tip diameter, D_{i2} : Proximal inner tip diameter, L : Tip length.

$$dR = \begin{cases} \frac{\rho \cdot dx}{2\pi(-x + \frac{d}{2})^2 - S_{particle}}, & -\frac{D_e}{2} < x < 0 \text{ (Domain 1)} \\ \frac{\rho \cdot dx}{(\frac{d}{2})^2 \pi - S_{particle}}, & 0 < x < e \text{ (Domain 2)} \\ \max \left(\frac{\rho \cdot dx}{\left(D_{i1} + \frac{(D_{i2} - D_{i1})x}{L} \right)^2 \pi - S_{particle}}, \frac{\rho \cdot dx}{2\pi(x - e + \frac{d}{2})^2 - S_{particle}} \right), & e < x < l \text{ (Domain 3)} \\ 0, & l < x < L \text{ (Domain 4)} \end{cases} \quad \begin{matrix} \text{Equation} \\ 1 \end{matrix}$$

The primitive integral of the differential resistance expression dR allows for the calculation of the magnitude impedance evolution along the structure as shown in Equation 2. The notation $|Z|_{Tip}(x)$ is selected to be coherent with experimental notation of impedance, although this value is assumed to be purely real according to this model.

$$|Z|_{Tip}(x) = \int dR \quad \text{Equation 2}$$

The total sensing tip magnitude impedance $|Z|_{Tip,tot}$ as physically measured between the two electrodes is obtained with the definite integral of the differential resistance dR as shown in Equation 3.

$$|Z|_{Tip,tot} = \int_{-\frac{D_e}{2}}^l dR \quad \text{Equation 3}$$

Similarly, the electrical potential evolution in the structure $U(x)$ is derived from the impedance evolution $|Z|_{Tip}(x)$, the voltage excitation U_{exc} and using Ohm's law.

$$I_{tot} = \frac{U_{exc}}{|Z|_{Tip,tot}} \quad \text{Equation 4}$$

$$du = dR \cdot I_{tot} \quad \text{Equation 5}$$

$$U(x) = \int du \quad \text{Equation 6}$$

The model is used to express the sensing tip sensitivity to particle sizes according to the different design parameters such as membrane thickness, aperture diameter, membrane diameter and electrodes position. The impedance peak magnitude $|\Delta Z|$ given by a particle is defined as total magnitude impedance $|Z|_{Tip,tot}$ when a particle is obstructing the aperture subtracted by the total magnitude impedance $|Z|_{Tip,Tot}$ when no particle are considered. The impedance variation is defined as the total magnitude impedance $|Z|_{Tip,Tot}$ when a particle is obstructing the aperture divided by the total magnitude impedance $|Z|_{Tip,Tot}$ when no particles are considered.

Even though this model is defined analytically, the solving is performed numerically using Python (Canopy, Enthouh Inc, US) to simplify the handling of such piecewise-defined functions and the variation of the numerous parameters. The Python code is shown in appendix (§7.2)

2.3 Results

2.3.1 Sensing tip characterization

This section presents a characterization and performances validation of the sensing tips used for cell detection.

2.3.1.1 Impedance & potential distribution

Using Equation 2 and Equation 6 of the analytical model, the sensing tip magnitude impedance $|Z|_{Tip}(x)$ and electrical potential $U(x)$ distributions are calculated for the actual sensing tip dimensions ($De = 1100 \mu m$, $d = 30 \mu m$, $e = 15 \mu m$, $l = 3500 \mu m$, $D_{i1} = 500 \mu m$, $D_{i2} = 5 mm$, $L = 50 mm$, $S_{Particle} = 0 \mu m$). Figure 2.8 a) shows the sensing tip magnitude impedance $|Z|_{Tip}(x)$ from the outer electrode along the tip structure and the electrical potential drop $U(x)$ along the same structure. This shows that 40% of the magnitude impedance increase and electrical potential drop are located within the second domain being the aperture region. When considering a region that extends by only $15 \mu m$ on both sides of the membrane that takes into account the spreading resistance in close proximity of the aperture, the impedance increase represents 60% of the total impedance magnitude. This $45 \mu m$ region centered on the membrane defines the sensitive volume of the tip. This typical behavior is expected from a Coulter counter topology where most of the impedance magnitude increase is localized in a sensitive volume of same order of magnitude as the particle volume to be detected. In this design, the sensitive volume being mainly located in the membrane forming the wall of the tip, no dead volume is left, which allows detecting each particle escaping or entering the tip by passing the membrane.

2.3.1.2 Sensing tip impedance spectra

Impedance spectra of a sensing tip manufactured with an aperture of $30 \mu m$ is measured using an impedance analyzer (Agilent 4294A, Agilent technologies, US). Figure 2.8 b) shows the sensing tip magnitude and phase impedance spectra. This measurement shows a wide resistive plateau in the frequency range starting below $1 kHz$ and extending up to $500 kHz$. This large plateau is obtained thanks to a design including large electrodes to allow a low electrodes cut-off frequency. Moreover, the thick walls of the tip allow to keep the stray

capacitance below 10 pF. These curves also show that the excitation frequency, which is chosen for impedance measurement, is not critical as long as it stays in the resistive plateau. An excitation frequency of 49 kHz is chosen to stay in the resistive plateau as well as below the cell beta dispersion frequency (Martinsen, 2011).

2.3.1.3 Aperture size and total impedance magnitude

The total magnitude impedance $|Z|_{Tip,tot}$ of sensing tips having different aperture sizes ranging from 30 μm to 46 μm in diameter are measured. As shown in Figure 2.8 c), impedance measurements (circles) follow the analytical model calculation (plain line) with errors comprised within +/- 15%. Measurement points having the same abscissa represent different measurements on the same tip. In this specific case, a significant part of the measurement errors are due to the successive connections of the sensing tip, which resulted in scratching the gold outer electrode.

Those considerations suggest that the analytical model is in acceptable agreement with the actual sensing tip impedance and can be used for design optimization as well as sensing tip quality check after fabrication by measuring the actual sensing tip impedance and comparing it with calculated values.

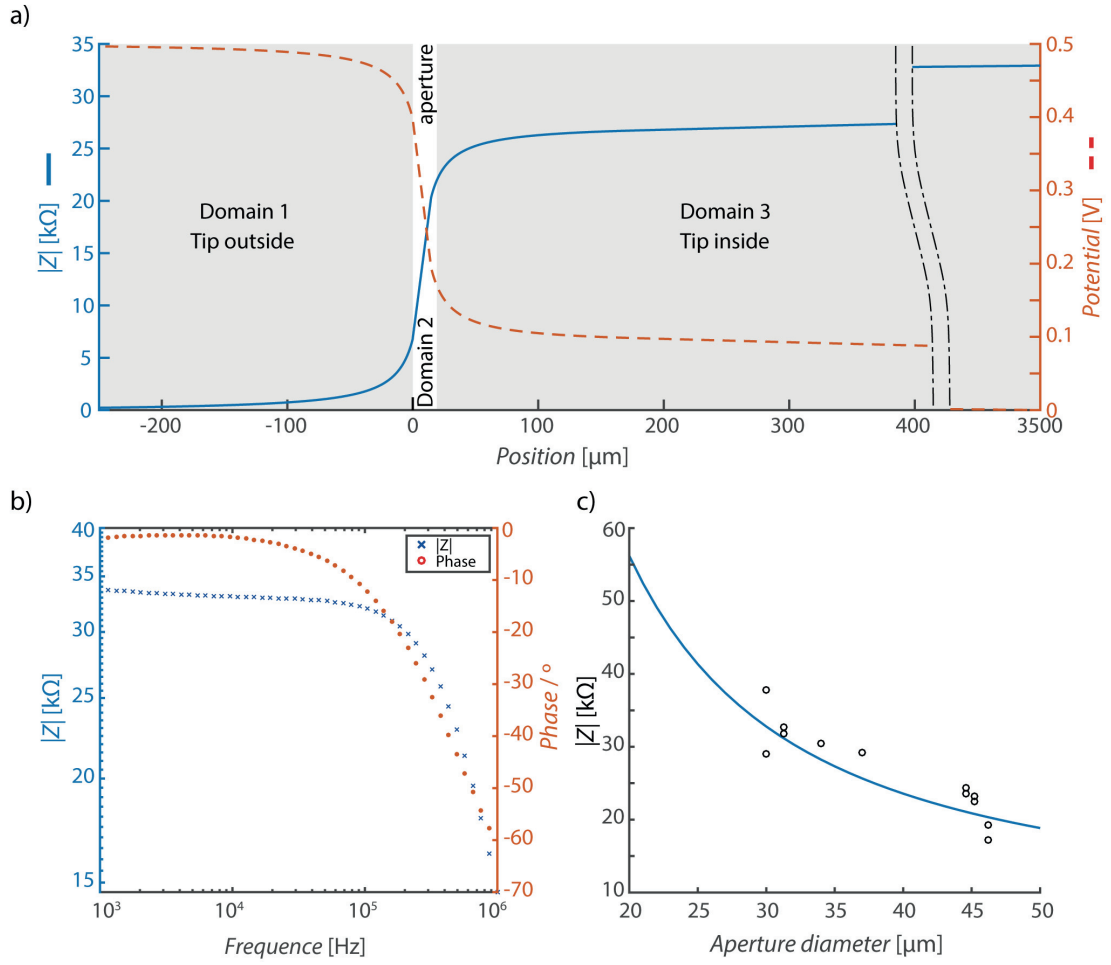


Figure 2.8 : Result of analytical model and experimental characterization of the sensing tip. a) Magnitude impedance and electrical potential along the sensing tip structure with a 30 μm aperture diameter according to the analytical model. It shows that the sensitive volume of the tip is located in the aperture and its close proximity (spreading resistance). b) Measurement of impedance magnitude and phase of a sensing tip. c) Total sensing tip impedance against the aperture diameter according to the analytical model (plain line) and sensing tip impedance measurements (circles).

2.3.1.4 Particle detection and sensitivity to particle size

To demonstrate the system ability to detect particles, a collection of 6, 10 and 15 μm diameter polystyrene beads were sequentially passed through sensing tip having an aperture around 33 μm . This experiment further allows determining the system sensitivity to dielectric particles size as well as the system resolution and limit of detection. Experimental data are also compared to the analytical model presented before.

Figure 2.9 a) shows the magnitude impedance given by the sequential passage of 6, 10 and 15 μm polystyrene beads through the sensing tip. Figure 2.9 b) shows the calibration curve relating the impedance value in arbitrary unit given by the instrumented pipette to an actual impedance value in ohm. To obtain this curve, 27 k Ω , 30 k Ω , 33 k Ω and 37.5 k Ω physical resistors replacing the sensing tip were directly measured with the system. Standard deviations of those impedance traces are also used to estimate the electrical instrumentation noise of this system. An impedance equivalent noise value is found to be 3.56 Ω for a 30 k Ω resistor plugged on the system.

Figure 2.9 c) shows the theoretical curve for particle size sensitivity obtained with the analytical model for a 35 μm aperture and other parameters as presented before as well as experimental data obtained with beads of a 6, 10 and 15 μm from Figure 2.8 a). As each bead's population was passed separately, the median value of the impedance peak prominence is used to determine the system sensitivity to a given bead size. The 6 μm , 10 μm and 15 μm beads population shows impedance variations of respectively 89.8 Ω , 382.9 Ω and 1346 Ω with standard deviation of 33 Ω , 94 Ω and 207 Ω in agreement with value anticipated from the analytical model. According to these results, the analytical model can be used for particle size determination using the impedance variation.

When no beads are passing the aperture, the impedance signal standard deviation is measured to estimate the equivalent impedance noise of the full system. This value is found to be 3.59 Ω meaning the total noise level is dominated by the instrumentation noise previously measured at 3.56 Ω with physical resistor. Assuming the limit of detection at 3 times the level of noise, and using the particle size sensitivity curve, the minimal particle that can be detected with this instrumented pipette is 3.2 μm . The spreading in particle size measurements including the actual bead size dispersion and the instrumented pipette noise for 6 μm , 10 μm and 15 μm is respectively 1.6 μm , 1.6 μm and 1.25 μm .

According to this experiment, 6 μm particle size can be detected and 15 μm particles are still flowing through the system without tip clogging. Given this particle size range, one can conclude that the system is well suited for mammalian cells dispensing as their typical size is between 6 μm and 15 μm . To guarantee single cell dispensing and avoid further dispensing in a well already containing a cell, it is more favorable to exceptionally interpret noise as a particle rather than missing a real particle. In such conditions, we chose a detection threshold $Z_{Th} = 20 \Omega$ for the dispensing procedure which is closer to the system

noise distribution $\sigma_{sys} = 3.59 \text{ } \Omega$ rather than the impedance peak magnitude $|\Delta Z|$ distribution. Assuming a Gaussian distribution of the noise centered at $\mu = 0 \text{ } \Omega$, the complement of the normal cumulative distribution function gives the probability $p = 1.3 \times 10^{-8}$ of a noisy sample exceeding the detection threshold as shown in Equation 7. This probability predicts the interpretation of a noisy sample as a particle passage in 1 over 7.9×10^7 samples. According to the system sampling rate of 2.4 kHz, this represents one false particle detection every 9 hours of the system use.

$$p = 1 - F(Z_{Th}|\mu, \sigma_{sys}) = 1 - \frac{1}{\sigma_{sys}\sqrt{2\pi}} \int_{-\infty}^{Z_{Th}} e^{\frac{-(t-\mu)^2}{2\sigma_{sys}^2}} dt = 1.3 \times 10^{-8} \quad \text{Equation 7}$$

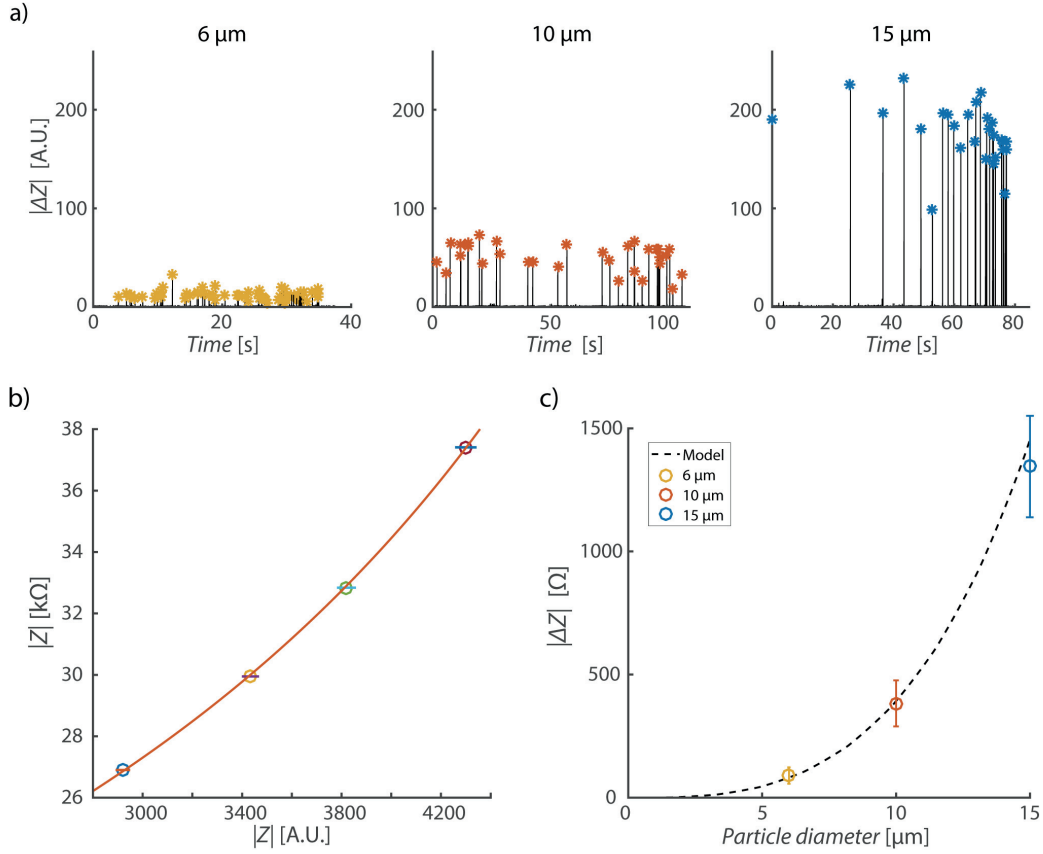


Figure 2.9 : Sensing tip sensitivity to dielectric particle size a) Impedance trace in arbitrary units (A.U.) for 6, 10 and 15 μm beads sequentially passed through the instrumented pipette using an acquisition sampling rate of 2.4 kHz (Same arbitrary units for the three beads populations). b) Calibration curve representing the actual impedance magnitude against the value read from the system in arbitrary units c) Sensing tip sensitivity to dielectric particle size according to the analytical model and experimental results with 6 μm , 10 μm and 15 μm beads.

2.3.1.5 Noise analysis & theoretical smallest particle detectable

In a Coulter counter and according to the hypothesis of purely resistive impedance, the fundamental noise contribution is given by the Johnson noise (Gillespie, 1996). This noise is linked to the thermal agitation of current carriers flowing through the aperture resistance. However, the total system noise also depends on the circuit used for the impedance measurement. Those aspects are discussed in the following section.

Figure 2.10 shows the simplest instrumentation allowing measuring the sensing tip impedance and consists of a voltage divider composed of a fixed resistance $R_{Measure}$ and the tip impedance R_{Tip} (as assumed purely resistive). An excitation voltage U_{Exc} is applied on this voltage divider. The voltage measured $U_{Measure}$ on the resistance $R_{Measure}$ contains the sensing tip impedance noise added with the measurement resistance $R_{Measure}$ noise. This voltage noise $v_{Measure,rms}$ is expressed in Equation 8. The voltage noise $v_{Tip,rms}$ occurring directly on the sensing tip impedance R_{Tip} is calculated using Equation 9. Dividing the sensing tip voltage noise $v_{Tip,rms}$ by the current flowing in the voltage divider gives the equivalent resistance noise $r_{Tip,rms}$ according to Equation 10. This noise can be compared with the impedance peak magnitude obtained by particle passage in the sensing tip according to the analytical model presented above (§2.2.6). This resistance equivalent noise is calculated for a sensing tip impedance R_{Tip} of 30 k Ω , a measurement resistance $R_{measure}$ of 30 k Ω and a bandwidth Δf of 2.4 kHz. The resistance equivalent noise $r_{Tip,rms}$ equals 0.093 Ω and defines the theoretical smallest noise level obtained with a 30 k Ω sensing tip impedance measured according to the topology presented in Figure 2.10.

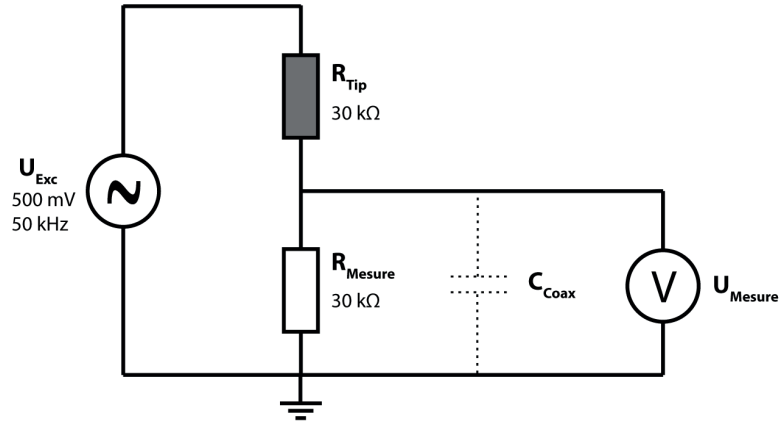


Figure 2.10 : Resistive bridge instrumentation allowing to measure the sensing tip impedance variation. It consists of a voltage divider composed of the sensing tip impedance and a measurement resistor on which voltage is measured.

$$v_{Measure,rms} = \sqrt{4k_B T (R_{measure} // R_{tip}) \Delta f} = 0.77 \mu V \quad \text{Equation 8}$$

$$v_{Tip,rms} = \sqrt{v_{Measure,rms}^2 \frac{R_{Tip}^2}{R_{Measure}^2}} = 0.77 \mu V \quad \text{Equation 9}$$

$$r_{Tip,rms} = \frac{v_{Tip,rms}}{I_{tot}} = \frac{v_{Tip,rms} * R_{tot}}{U_{exc}} = \frac{v_{Tip,rms} * (R_{Measure} + R_{Tip})}{U_{exc}} = 0.093 \Omega \quad \text{Equation 10}$$

The analytical model is then used to express the total magnitude impedance $|Z|_{Tip,tot}$ of sensing tip with different aperture diameters and the corresponding impedance peak magnitude $|\Delta Z|$ obtained for different particle sizes. These values are compared with the minimal level of noise using Equation 10 and the respective total magnitude impedance R_{Tip} . The minimal particle size detectable is defined as the particle diameter yielding an impedance peak magnitude at least 3 times (3σ) higher than the noise level.

Accordingly, Figure 2.11 shows the theoretical minimal particle diameter that can be detected for an aperture of chosen dimensions (black circles). Figure 2.11 also presents the performance of a commercial Coulter counter particle analyzer (blue crosses) according to their specifications (AZO, 2016) as well as the sensing tip performance (red cross) measured in the previous section (§2.3.1.4). This model predicts a theoretical limit of detection of 230nm, 420 nm and 950 nm for aperture of 20 μm , 30 μm and 50 μm respectively. As expected, those theoretical performances are slightly better than the actual commercial Coulter counter specifications defining minimal observable particle of 400 nm, 600 nm and 1 μm for similar aperture sizes.

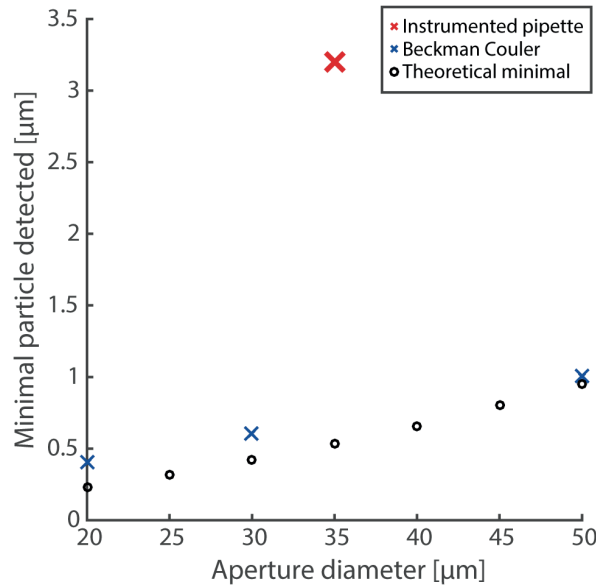


Figure 2.11 : Minimal particles size detectable for a given aperture size. Black dots shows the minimal particle size detectable according to the particle impedance peak magnitude estimated with analytical model and the Johnson noise given by the corresponding aperture resistance. Blue crosses show the minimal particle size detectable in a commercial Coulter counter according to the instrument guideline. The red cross shows the minimal particle size detectable with the current version of the instrumented pipette and a sensing tip with a 35 μm aperture.

The schematic proposed in Figure 2.10 becomes inefficient when the impedance to be measured is combined with an important parallel capacitance C_{Coax} induced by measurement cables as represented in Figure 2.10. In particular, it prevents the use of coaxial cable, long PCB traces or any fixture increasing the stray capacitance to connect the sensing tip to the

electronic instrumentation. Because of the sensing tip geometry and as the electronic instrumentation cannot be integrated in the tip, a connecting fixture is required and the stray capacitance is inevitably increased. For these practical reasons, an instrumentation topology based on a transimpedance amplifier more tolerant to stray capacitance is selected and presented in Figure 2.12. The voltage noise at the output of this amplifier $v_{Measure,rms}$ is calculated for a sensing tip resistance R_{Tip} of 30 k Ω , a transimpedance feedback resistance R_{Feed} of 47 k Ω and a bandwidth of 2.4 kHz according to Equation 11. The voltage and current noise of the operational amplifier (AD8065, Analog Device, US) are 7 nV/ \sqrt{Hz} and 0.6 fA/ \sqrt{Hz} respectively. With a similar development presented for the previous instrumentation but according to this topology, the resistance equivalent noise $r_{Tip,rms}$ is calculated using Equation 12 and equals 0.086 Ω .

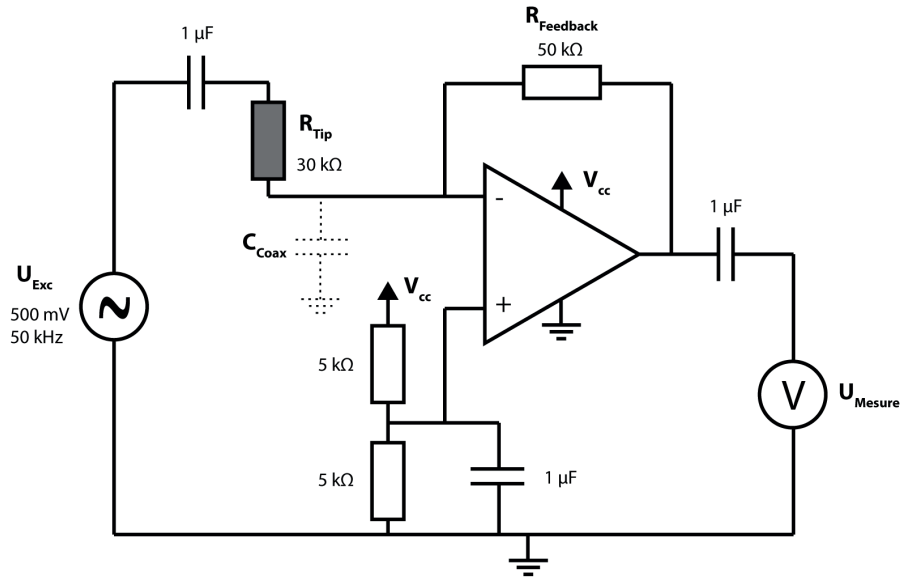


Figure 2.12 : Transimpedance amplifier instrumentation allowing to measure the sensing tip impedance variation. Compared to the resistive bridge, the transimpedance amplifier instrumentation is tolerant to a high line capacitance between the sensing tip impedance and the amplifier input.

$$\begin{aligned}
& v_{Mesure,rms} \\
&= \sqrt{\left((i_n R_{Feed})^2 + \left(e_n \frac{R_{Tip} + R_{Feed}}{R_{Tip}} \right)^2 + 4k_B T R_{Tip} \left(\frac{R_{Feed}}{R_{Tip}} \right)^2 + 4k_B T R_{Feed} \right) * \Delta f} \quad \text{Equation 11} \\
&= 2.4 \mu V
\end{aligned}$$

$$\begin{aligned}
r_{Tip,rms} &= \frac{v_{Tip,rms}}{I_{Tip}} = \frac{R_{Tip} \frac{v_{Feed,rms}}{R_{Feed}}}{\frac{U_{exc}}{R_{Tip}}} = \frac{R_{Tip} \frac{v_{Mes,rms}}{R_{Feed}}}{\frac{U_{exc}}{R_{Tip}}} = \frac{v_{Mes,rms} R_{Tip}^2}{U_{exc} R_{Feed}} \quad \text{Equation 12} \\
&= 0.086 \Omega
\end{aligned}$$

Table 2.2 shows a noise summary with theoretical noise calculated for the voltage divider and transimpedance instrumentation as well as experimental noise measured with the instrumented pipette and a sensing tip. The minimal voltage noise level is given by the voltage divider instrumentation with 0.77 mV. It represents a resistance equivalent noise of 0.093 Ω and allows theoretically detecting particle down to 560 nm in a 35 μ m aperture. The noise level calculated for the transimpedance instrumentation is 2.4 μ V. Despite a slightly higher voltage noise value, it represents a resistance equivalent noise in the same order of magnitude with 0.086 Ω and allows theoretically to detect particle down to 530 nm in a 35 μ m aperture.

As described in the previous section (§2.3.1.4), the instrumented pipette noise contribution from its electronic instrumentation was measured 3.56 Ω . The standard deviation of the instrumented pipette in dispensing condition was measured at 3.59 Ω and according to the sensitivity curve it represents a minimal particle size detectable of 3.2 μ m for 35 μ m aperture. Comparing those values with the theoretic smallest noise in a transimpedance topology shows that our electronic instrumentation could still be perfected to exhibit a noise level dominated by the fundamental aperture resistance Johnson noise instead of the instrumentation noise itself. This would allow increasing the aperture diameter while detecting the same particle population and consequently further decreasing the risk of clogging. Finally, the electrochemical noise arising at the electrode interface is neglected in this study. However, the proximity of the theoretical noise evaluation and the actual commercial coulter performances suggests that this assumption is acceptable.

Table 2.2 : Theoretical and experimental noise of the different impedance measurement instrumentations

	Theoretical minimal noise with transimpedance	Theoretical minimal noise with resistive bridge	Instrumented pipette noise measured with a physical resistor	Instrumented pipette noise measured during system operation
Noise level [μV]	2.4	0.77	-	-
Equivalent noise level [Ω]	0.086	0.093	3.56	3.59
Minimal particle size detectable in 35 μm aperture [μm]	0.530	0.560	3.2	3.2

2.3.1.6 Effect of the membrane thickness on the particle detection and size sensitivity

The analytical model is also used to evaluate the effect of the membrane thickness on the sensing tip sensitivity to particles. Figure 2.13 a) shows the ratio of the impedance variation created by the passage of a dielectric particle of given dimensions through the aperture versus the thickness of the membrane. The curves presented in this figure using the analytical model, correspond respectively to the passage of 6 μm , 10 μm and 15 μm particles. The optimum membrane thickness for detecting particle of a given dimension corresponds to the point where these curves are at a maximum. This predicts a membrane thickness that is slightly smaller than the actual particle size. This effect is related to the influence of the spreading resistance defining a sensitive volume slightly extending from the aperture as expected from Figure 2.8 a).

However, the time of particle passage in the aperture also depends on the membrane thickness. A compromise is chosen with a membrane thickness of 15 μm . This is not the absolute theoretical maximal impedance variation according to Figure 2.13 a) but allows for a reasonable particle dwell time in the sensitive volume and thus increases the number of points acquired. According to Figure 2.13 a), this optimization on the number of points acquired on a particle passage is obtained at a minimal cost of a few percent reduction in the impedance signal variation.

Figure 2.13 b) shows the averaged impedance time trace for the same three populations of 6, 10 and 15 μm polystyrene beads shown in Figure 2.9 a) for a sampling rate of 2.4 kHz. The averaged time traces have been superimposed and centered. Average impedance peaks for 15 μm , 10 μm and 6 μm beads are represented by respectively 15, 9 and 3 sampling points above the previously chosen threshold $Z_{\text{Th}} = 20 \Omega$.

The probability to miss a 6 μm particle correspond to the cumulative missing of the 3 points defining the 6 μm particle impedance peak. Considering the 3 points above the threshold with their respective impedance magnitude of $|\Delta Z_1| = 37 \Omega$, $|\Delta Z_2| = 89.8 \Omega$ and $|\Delta Z_3| = 37 \Omega$, and their standard deviation $\sigma_{6\mu\text{m}} = 33 \Omega$ the probability p equals 0.0016 using the normal cumulative distribution function according to Equation 13. It is equivalent to 1 particle missed every 632 dispenses.

$$F(X|\sigma) = \frac{1}{\sigma\sqrt{2\pi}} \int_{-\infty}^{Z_{\text{Th}}} e^{\frac{-(t)^2}{2\sigma^2}} dt$$

$$p = \left(1 - F(|\Delta Z_1| - Z_{\text{Th}}|\sigma_{6\mu\text{m}})\right) \cdot \left(1 - F(|\Delta Z_2| - Z_{\text{Th}}|\sigma_{6\mu\text{m}})\right) \cdot \left(1 - F(|\Delta Z_3| - Z_{\text{Th}}|\sigma_{6\mu\text{m}})\right) = 0.0016 \quad \text{Equation 13}$$

This represents the worst-case scenario for the dispensing of a population containing 6 μm particles only. The same probability drop to 1 event missed every 2.5×10^9 dispenses for 10 μm particles as more points with higher impedance magnitude are considered. In the context of single particle dispensing for mammalian cell isolation, this demonstrates the very low probability of missing an event that could lead to the dispensing of two cells in the same well without detecting it in the impedance signal.

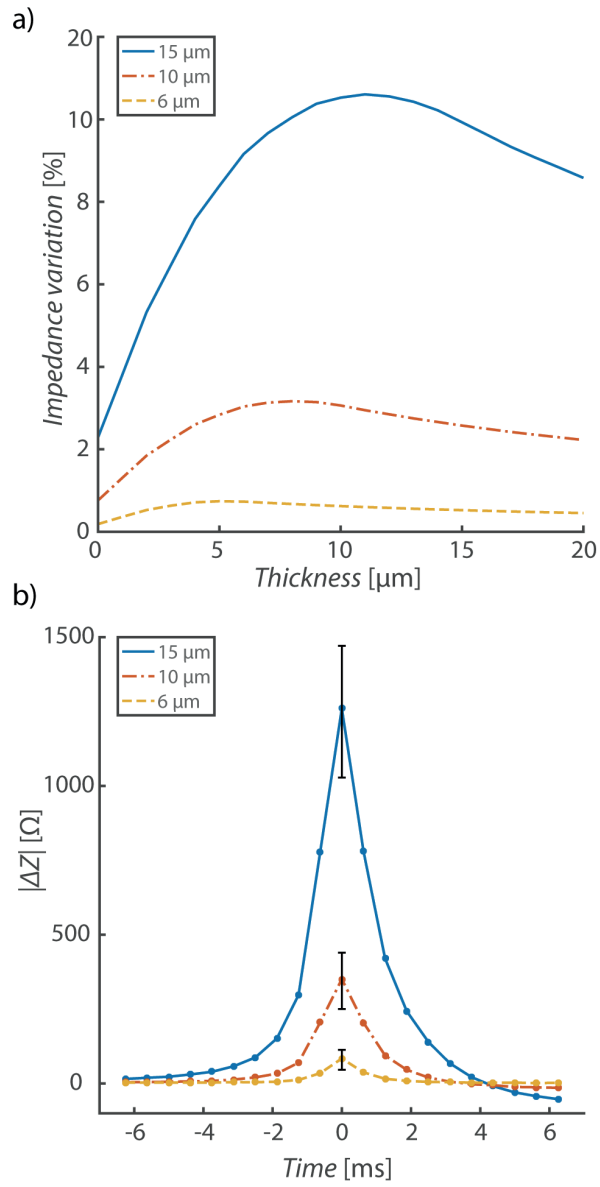


Figure 2.13 : Effect of the membrane thickness on the particle detection and size sensitivity. a) Membrane thickness impact on the impedance variation for beads populations of 6, 10 and 15 μm crossing the sensing tip aperture and obtained from the analytical model. b) Averaged impedance time trace on 56, 27 and 31 peaks for the three different sub-population of particles of 6, 10 and 15 μm travelling along the tip aperture.

2.3.2 Fabrication constraints allowing cost effective design

The goal of this section is to discuss the design constraints allowing for a cost effective fabrication process compliant with disposable devices.

2.3.2.1 *Effect of the electrodes placement*

Figure 2.14 a) shows the sensing tip total impedance magnitude against the inner electrode distance from the membrane according to the analytical model (plain line) and corresponding measurements performed with an impedance analyzer (Agilent 4294A, Agilent technologies, US). For the inner electrode placed at 1 mm from the aperture, the total impedance is 31 k Ω at 49 kHz. When the same electrode is then retracted at 3.5 mm and 5 mm away from the aperture, a total sensing tip impedance of respectively 37 k Ω and 37.8 k Ω is measured at 49 kHz. The impedance difference for the two electrodes extreme positions is 6 k Ω , which is in agreement with the analytical model and corresponds to less than 20%. This shows that, in this design, a large electrode displacement does not significantly affect the total impedance and the electrical potential distribution in and around the tip.

Additionally, Figure 2.14 b) shows the sensing tip impedance variation when 15 μm beads passing through the aperture versus the membrane to electrode distance for distal inner tip diameter of 60 μm , 150 μm and 500 μm according to the analytical model. For an aperture of 30 μm and a significantly larger distal inner tip diameter of 500 μm as chosen in this design, the impedance change due to 15 μm beads is expected to be 11% with a 100 μm membrane to electrode distance. When the same electrode is then retracted at 500 μm away from the aperture the impedance change is still 10% for 15 μm beads. On the other hand, for a smaller distal inner tip diameter of 60 μm , the same electrode displacement from 100 μm to 500 μm induces an impedance variation going from 10% to 3.5%. This demonstrates that the large ratio between the membrane and aperture diameters chosen in this design offers great flexibility of electrodes placement. Consequently, with our design, cost effective methods can be used for inner electrode placement and outer electrode deposition. In particular, photolithography can be avoided for electrode structuration, which would have been cumbersome and expensive for microfabrication on a 3D object such as a tip. This limited electrode position sensitivity also limits noise induced by electrode movement or vibration. Moreover far electrode placement prevents aperture clogging with bubble formed at electrode in a case high electric potential is used.

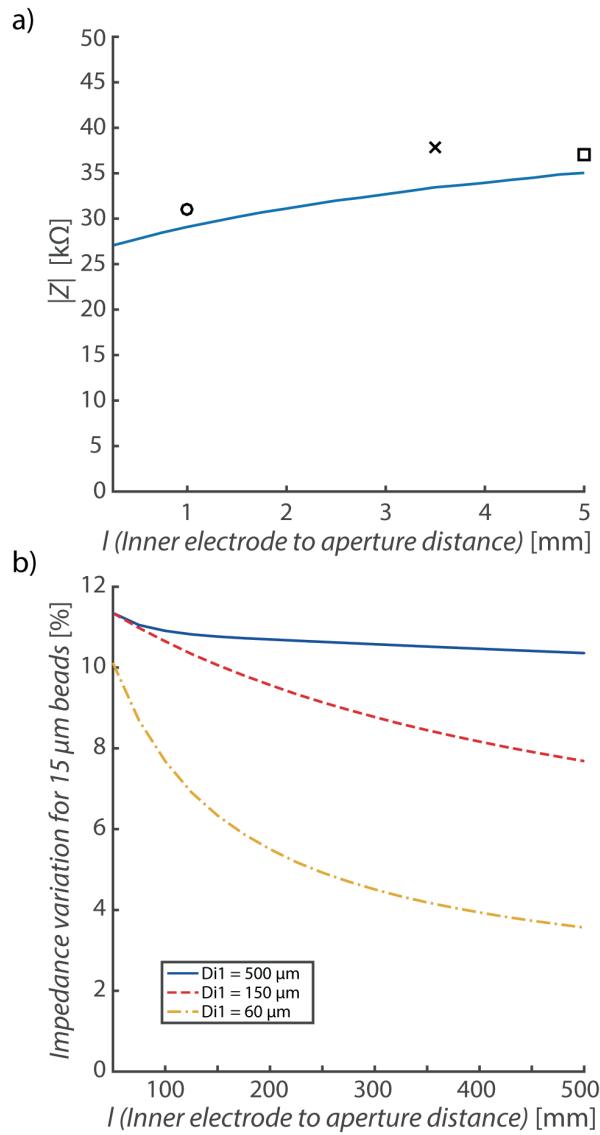


Figure 2.14 : Effect of the electrode placement. a) Total impedance magnitude versus inner electrode distance to the membrane according to the analytical model and measurements. b) Effect of electrode distance to the membrane on the impedance change due to the passage of a 15 μm bead.

2.3.2.2 Effect of the aperture size

Figure 2.15 shows the impedance peak magnitude for 6, 10 and 15 μm particles against the aperture diameter according to the analytical model (§2.2.6). As expected intuitively, the sensitivity to particle size decrease with the increase of the aperture size. However, the aperture has to presents a sufficiently important diameter to prevent particle clogging. The 6 μm particle curve shows an impedance variation decreasing from 81 Ω to 73 Ω when the

aperture size is increased from 35 μm to 36 μm . Even reduced by 10%, the impedance variation for 6 μm particle is still largely detectable with the instrumented pipette. On the other hand, if the aperture size is decreased by 1 μm , the impedance variation will be increased by 14%, which facilitates the detection. Moreover, a 34 μm aperture is still acceptable to prevents clogging with a particle size distribution comprised between 6 μm and 20 μm . It demonstrates a system tolerance to aperture variation of at least $\pm 1 \mu\text{m}$ to allow for the particles detection. Particle sizing is also tolerant to aperture variation provided that the sensing tip total impedance magnitude baseline is measured to deduce the aperture size and calibrate the system accordingly.

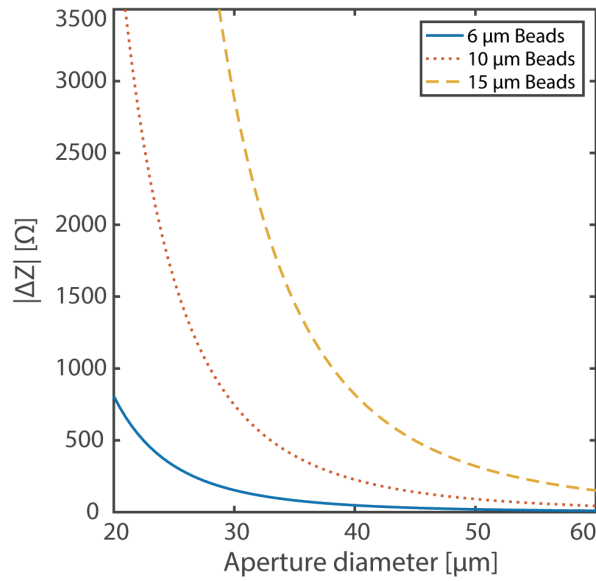


Figure 2.15 : Effect of the aperture diameter on the particle detection. The impedance peak magnitude due to the passage of 6, 10 and 15 μm particles decrease with the increase of the aperture diameter.

2.3.2.3 Summary on fabrication tolerances

The effect of aperture size variation is evaluated in the previous section (§2.3.2.2) and shows a tolerance up to $\pm 1 \mu\text{m}$ on the 35 μm aperture inducing an impedance peak magnitude decrease of maximum 10% for 6 μm particles.

According to the Coulter counter principle, the aperture position in the membrane does not influence the detection performances as long as the aperture is not too close to the membrane boundary. If the aperture is positioned too close to the tip wall, the aperture

spreading resistance might be increased. Avoiding this boundary effect leaves freedom in the aperture placement of +/- 200 μm .

The effect of membrane thickness variation is evaluated in a previous section (§2.3.1.6). A tolerance of +/- 2 μm on the 15 μm thick membrane, reduce the impedance variation by a maximum of 6 % for 6 μm beads.

The effect of inner electrode position variation is evaluated in a previous section (§2.3.2.1) and shows a tolerance up to +/- 1 mm on the 3.5mm electrode position inducing an impedance variation reduction of 3% for 6 μm beads. The same section shows that the tip distal diameter defining the membrane section has a negligible effect on the impedance variation due to particle passage as long as significantly larger than the aperture section.

The main constrains on the electrode surface is the electrode cut-off frequency that need to be kept at least 100 times smaller than the signal excitation frequency of 49 kHz as shown in Equation 14 to avoid the electrode capacitance contribution in the sensing tip total impedance. Under this constraint, the minimal electrode surface can be calculated considering a tip real impedance R_{Tip} of 30 k Ω , a water outer helmoltz plane distance d_{OHP} of 0.5 \AA , an absolute permittivity of 8.85×10^{-12} F/m and relative permittivity for water of 12.4 (Meissner, 2012). Equation 15 shows a minimal electrode surface of 0.048 mm^2 to avoid the impedance contribution from the electrode capacitance.

$$f_{cut-off,electrode} = \frac{1}{2\pi R_{Tip} C_{electrode}} < \frac{f_{excitation}}{100} < 500 \text{ Hz} \quad \text{Equation 14}$$

$$S_{electrode} = \frac{C_{electrode} \cdot d_{OHP,water}}{\epsilon_o \epsilon_r}$$

$$> \frac{1}{2\pi R_{Tip} f_{cut-off,electrode}} \cdot d_{OHP,water} = 0.048 \text{ mm}^2 \quad \text{Equation 15}$$

These different considerations about fabrication tolerances for the sensing tip design parameter are summarized in Table 2.3. It shows that only two parameters require a precise fabrication control, which are the aperture size and the membrane thickness. The aperture

size depends on the laser beam shape that is expected to be consistent over the different production batches after initial adjustments and calibration. The membrane thickness mainly depends on the parylene chemical vapor deposition process, which can be adjusted and consistently repeated over batches. The 3D shape of the tip does not affect those fabrication parameters. Other parameters such as aperture and electrode positions are very tolerant to displacements and permits avoiding photolithography. The inner electrode can be inserted by hand or with a robot. The outer electrode can be deposited through a far field shadow mask. The low requirement on the distal inner tip diameter also shows that the full process can be performed on an existing pipetting tip.

Table 2.3 : Summary on the sensing tip design parameter tolerances

	Nominal	Prototype realization (n=9)	Desired tolerances on production	Effect with desired tolerances (Worst case)
Aperture size d	35 μm	$\mu_d = 39.2 \mu\text{m}$, $\sigma_d = 3.3 \mu\text{m}$	+/- 1 μm	Impedance variation reduced by 10 % for 6 μm particles
Aperture position	Centered	Eccentricity $\mu_E = 5.76 \mu\text{m}$, $\sigma_E = 2 \mu\text{m}$	Eccentricity < 200 μm	No effect as long as not to close to the boundary of the membrane
Membrane thickness e	15 μm	N/A	+/- 2 μm	Impedance variation reduced by 6 % for 6 μm particles
Electrode position l	3.5 mm	$\mu_l = 3.52 \text{ mm}$, $\sigma_l = 0.5 \text{ mm}$	+/- 1 mm	Impedance variation reduced by 3 % for 6 μm particles
Distal inner tip diameter D_{ii}	500 μm	$\mu_{Dii} = 515.9 \mu\text{m}$, $\sigma_{Dii} = 29.9 \mu\text{m}$	$D_{ii} > 10 * d$ > 350 μm	Little effect as long as bigger than 10 times the aperture diameter
Electrode surface (3mm immersed)	~1 mm ²	$\mu_S = 1.63 \text{ mm}^2$, $\sigma_S = 0.25 \text{ mm}^2$	Surface > 0.048 mm ²	No effect as long as bigger than 0.048 mm ²

2.3.3 Sensing tip fluidic behavior

The fluidic behavior of the sensing tip is characterized and a corresponding model is proposed to determine important dispensing parameters.

2.3.3.1 Fluidic characterization

Figure 2.16 presents an experiment where liquid (DPBS 1x, Sigma Aldrich, US) is aspirated and dispensed in cycle with a sensing tip having an aperture of ~30 μm . The well containing

the liquid to be aspirated and dispensed with the sensing tip is placed on a precision microbalance (PA214, OHAUS, US) allowing to determine the tip loaded volume by measuring the well weight with a sampling rate of 1 s. Successively, the negative and positive pressures are applied at - / + 10 mbar, - / + 5 mbar, - / + 2 mbar and - / + 1 mbar and tip loaded volume is measured along time as shown in Figure 2.16 a). Using the derivative of the tip loaded volume against time, the liquid flowrate is calculated on the same data set. The flowrate against the tip loaded volume is shown in Figure 2.16 b) for the different aspirating and dispensing pressures.

Figure 2.16 b) shows a non-constant liquid flowrate over the tip loaded volume for a given pressure. This demonstrates that the hydrostatic pressure has a non-negligible influence in the fluidic behavior of the sensing tip and need to be taken in account to control the liquid flowrate. Also, the effect of the hydrostatic pressure prevents to use the full tip volume when using small pressures as shown in Figure 2.16 a).

This experiment also shows that the liquid level at equilibrium with no external pressure applied is above the well liquid level. It demonstrates the influence of the capillary pressure on the sensing tip. Furthermore, two different liquid height equilibrium are observed if the liquid is filling or leaving the tip. With no external pressure applied, the liquid height equilibrium is measured at 11.5 mm when the liquid is loading in the tip. When the liquid is leaving the tip, the liquid height equilibrium is measured at 14 mm. This also suggests a capillary pressure difference between the liquid aspiration and dispensing phases.

Because of the low hydraulic resistance of the tip, the hydrostatic, capillary and external applied pressures have contributions of the same order of magnitude on the liquid flowrate. Hence, all those different contributions need to be taken in account to control the flowrate. The consequence is that the dispensing protocol needs to be fixed and respected during the dispensing phase to determine the actual liquid height giving the hydrostatic pressure and the flow direction giving the capillary pressure.

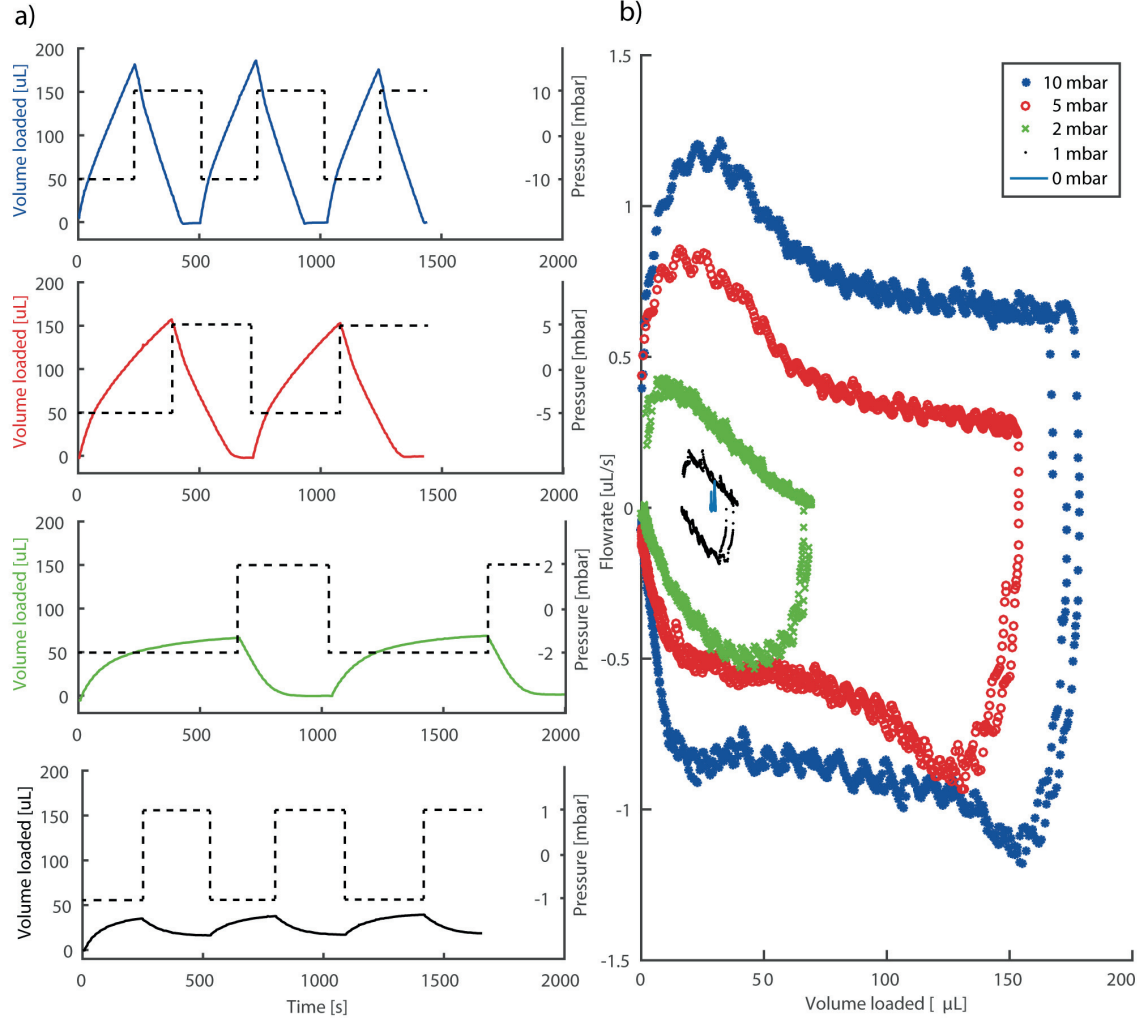


Figure 2.16 : Sensing tip fluidic characterization with cycles of liquid aspiration and dispense. a) Shows the volume contained in the sensing time against time for aspirating and dispensing pressure of ± 10 mbar, ± 5 mbar, ± 2 mbar, ± 1 mbar. b) Shows the liquid flowrate against time of the same data set.

2.3.3.2 Fluidic Model

Based on the previous sensing tip fluidic characterization (§2.3.3.1), a fluidic model taking in account the different contribution of hydrostatic, capillary and external applied pressures is proposed. This model is represented with an electrical-hydraulic equivalent circuit as shown in Figure 2.17.

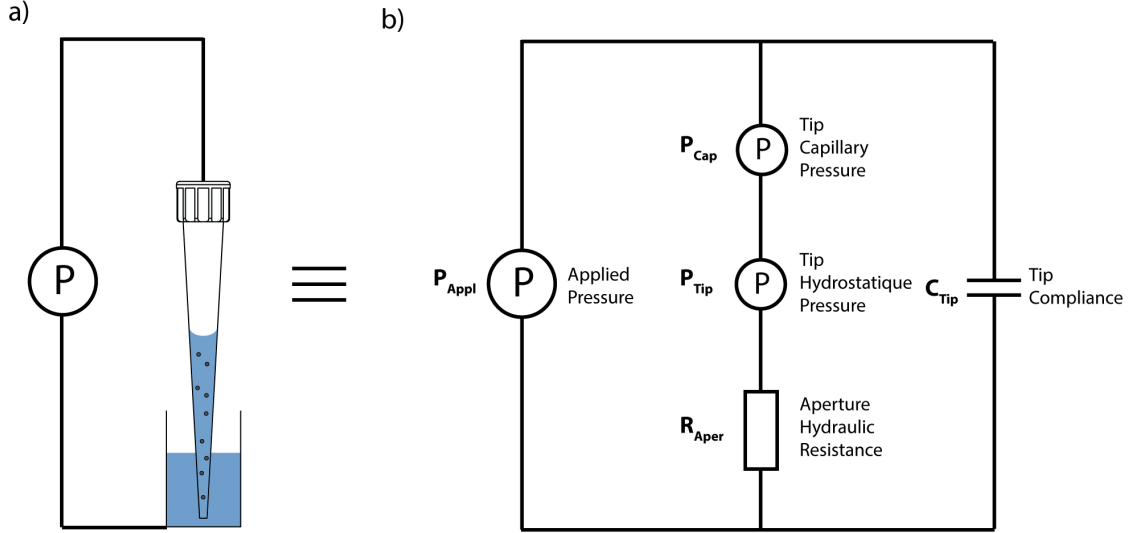


Figure 2.17 : Fluidic model of the sensing tip. The fluidic model is defined by the external pressure applied to the sensing tip in addition to the tip capillary pressure, tip hydrostatic pressure, aperture hydraulic resistance and tip compliance.

The tip hydrostatic pressure is defined by the liquid height in the tip $h_{liquid,Tip}$ and the depth at which the tip is immersed in the well $h_{immersed}$ according to Equation 16 as well as the gravity $g = 9.81 \text{ m/s}^2$ and density of the liquid $\rho = 1000 \text{ kg/m}^3$.

$$P_{Hydro}(t) = \rho g (h_{liquid,Tip}(t) - h_{immersed}) \quad \text{Equation 16}$$

Considering the geometry of the sensing tip which is a truncated cone, the liquid height $h_{liquid,Tip}$ can be calculated in function of the liquid volume contained inside the tip V_{Tip} using the tip length $L = 50 \text{ mm}$, its proximal diameter $D_{i2} = 5 \text{ mm}$, its distal external diameter $D_e = 1.1 \text{ mm}$ as well as the truncated length of the cone $l_{truncated} = 7.5 \text{ mm}$.

$$h_{liquid,tip}(t) = \sqrt[3]{\frac{3(L + l_{truncated})^2 \left(V_{Tip}(t) + \frac{1}{3} \left(\frac{D_e}{2} \right)^2 \pi l_{truncated} \right)}{\left(\frac{D_{i2}}{2} \right)^2 \pi}} - l_{truncated} \quad \text{Equation 17}$$

The tip capillary pressure is defined experimentally in liquid aspirating and dispensing conditions according to measurements on the previous section (§2.3.3.1) and results in Equation 18.

$$P_{Capillary}(t) = \begin{cases} -140 \text{ Pa} & \text{if liquid dispensing} \\ -115 \text{ Pa} & \text{if liquid aspirating} \end{cases} \quad \text{Equation 18}$$

The effective pressure difference on the aperture is defined as the sum of all the pressures contributions given in Equation 19.

$$P_{Aperture}(t) = P_{Applied}(t) + P_{Hydro}(t) + P_{Capillary}(t) \quad \text{Equation 19}$$

Assuming a laminar conditions and a Poiseuille flow inside the aperture, the hydraulic resistance is calculated using with the liquid viscosity $\mu = 1 \times 10^{-3} \text{ Pa} \cdot \text{s}$, the thickness of the membrane $e = 15 \text{ } \mu\text{m}$ and the aperture diameter $d = 30 \text{ } \mu\text{m}$ as shown in Equation 20.

$$R_{Aperture} = \frac{8\mu e}{\pi d^4} = 4.7 \times 10^{10} \frac{\text{Pa} \cdot \text{s}}{\text{m}^3} \quad \text{Equation 20}$$

The flowrate can be calculated with the quotient of the total pressure applied on the aperture $P_{Aperture}$ and the aperture hydraulic resistance $R_{Aperture}$ as shown in Equation 21.

$$Q(t) = \frac{P_{Aperture}(t)}{R_{Aperture}} \quad \text{Equation 21}$$

The tip volume variation $\frac{dV_{Tip}}{dt}$ defined by the aperture flowrate $Q(t)$ depends on the loaded tip volume $V_{Tip}(t)$ itself and consequently Equation 22 is a differential equation. This equation is numerically solved using Using Matlab (R2016a, Mathworks, US) to find the tip loaded volume along time as shown in Equation 23.

$$F(t) = \frac{dV_{Tip}}{dt} = \frac{P_{Aperture}(V_{Tip}(t))}{R_{Aperture}} \quad \text{Equation 22}$$

$$V_{Tip}(t) = \int_0^t F(t)dt \quad \text{Equation 23}$$

2.3.3.3 Model validation

An experimental validation of the model was performed to validate the Poiseuille flow assumption and the empiric values chosen for the capillary pressure. Before the experiment, a sensing tip with a 30 μm aperture is loaded with 80 μL of liquid (DPBS 1x, Sigma Aldrich, US). Then, during the first 400 seconds of the experiment, the tip is kept in the air above a well. After 400 seconds, the tip is immersed by 3mm in a well containing the same liquid. No external pressure is applied in this experiment. By filming the sensing tip and the liquid level during the experiment, the liquid height and tip loaded volume along time were extracted using ImageJ (NIH, US). Using the same experimental parameters, the expected tip volume along time is also evaluated with the fluidic model presented in the previous section (§2.3.3.2). Theoretical results are superimposed with experimental data in Figure 2.18 a). The two curves are in good agreements and suggest that the fluidic model can be used for the sensing tip fluidic behavior description if initial conditions are well controlled. Thanks to the model, other parameters such as the flowrate, hydrostatic pressure and capillary pressure are also evaluated and represented in Figure 2.18 b). Those results illustrates the important flowrate variation during the dispensing ranging from 2 $\mu\text{L/s}$ to 0.25 $\mu\text{L/s}$ due to the change in liquid height. This experiment also shows that the flowrate is negligible when the tip is not immersed in water which is an advantage to avoid particle loss in hanging droplets during non-immersed phase of the dispense.

Based on those data, the Reynolds numbers for the aperture $d = 30 \mu\text{m}$ and the tip section $D_{i1} = 500 \mu\text{m}$ are calculated for a flowrate $Q = 2 \times 10^{-9} \text{ m}^3/\text{s}$.

$$Re_{Aperture} = \frac{\rho V d}{\mu} = \frac{4 \rho Q}{\pi \mu d} = 84.9 \quad \text{Equation 24}$$

$$Re_{Tip} = \frac{4 \rho Q}{\pi \mu D_{i1}} = 5.09 \quad \text{Equation 25}$$

The Reynold numbers found in the tip and aperture validate the hypothesis of laminar flow. Because of the limited thickness of the aperture, the fluid flow is arguably not fully developed in this region. However, in this limited pressure range, the hypothesis of a Poiseuille flow yields to acceptable results for flowrate estimation as shown experimentally.

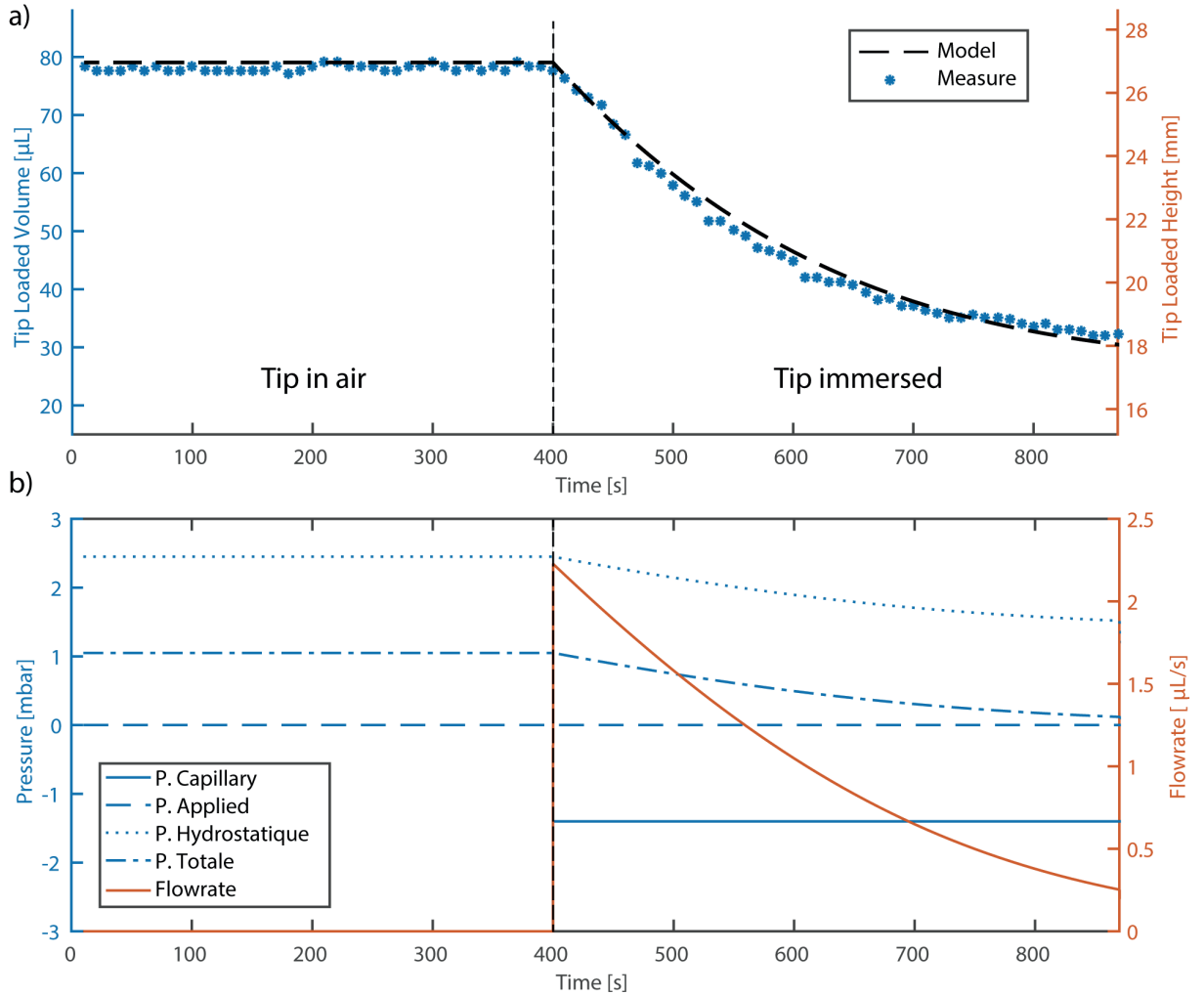


Figure 2.18 : Fluidic model validation with liquid dispensing experiment. a) Presents the dispensing of liquid with a sensing tip and shows the tip loaded volume against time according to the fluidic model and a validation experiment. b) Shows the corresponding pressure and flowrate values obtained with the fluidic model.

2.3.3.4 Model parameters for cell dispensing

The choice of the dispensing pressure P_D is limited by the particle speed that requires to be adapted to allow at least 3 to 15 samples of impedance measurement to be acquired when the particle pass the sensitive volume. During single particle dispensing experiment (§2.3.4),

this dispensing pressure is manually adjusted to find the value where particles start to flow and impedance peaks are detected accordingly. Taking in account the capillary and hydrostatic pressure, it defines an effective pressure drop at the membrane comprised between 0 mbar and 0.5 mbar.

Assuming that the liquid flow is laminar in the sensing tip structure imposes no time dependence on the fluid speed field. Thus, the only phenomena preventing to re-aspirate particles if the pressure is reversed is the particle sedimentation speed. It is assumed that the dispensing pressure P_D is chosen to have a pressure drop at the membrane of 0.2 mbar and the holding pressure P_H chosen 100 times smaller at -2 μ bar. The escape distance l_{escape} from which the particle cannot be aspirated anymore because of the cell sedimentation speed can be estimated by the point where the fluid speed is equal to the cell sedimentation speed $v_{cell,seim}$ estimated at 3 μ m/s (Muller, 2016). Because of the mass conservation, the holding flowrate Q_H given by the holding pressure P_H is constant and the flow speed decrease with the increase of the surface through which the fluid streamline converge toward the tip as shown in Figure 2.19. This surface is defined as the half sphere of radius l_{escape} . Accordingly, the escape distance l_{escape} for cells can be estimated at 472 μ m using Equation 27.

$$Q_H = v_{cell,seim} \cdot 2\pi l_{escape}^2 \quad \text{Equation 26}$$

$$l_{escape} = \sqrt{\frac{F_H}{2\pi v_{cell,seim}}} = 472 \mu m \quad \text{Equation 27}$$

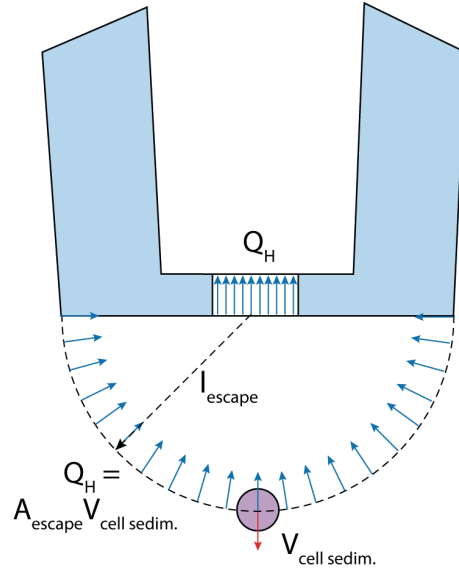


Figure 2.19 : Sketch illustrating the concept of particle escape distance. Particles have to reach this escape distance where their sedimentation speed equals the liquid flow speed to avoid re-aspiration in the sensing tip due to the holding pressure.

On the other hand, during the dispensing phase, the distance traveled by the particle can be calculated by integrating its speed over time. The particle speed is the sum of the cell sedimentation speed and the flow speed. For the dispensing pressure $P_D = 0.2$ mbar, the corresponding flowrate Q_D of $0.42 \mu\text{L/s}$ is conserved along the structure. The flow speed v_{flow} is calculated by the mass conservation with the ratio of the aperture section and the sphere defined by cell position l . Consequently, the flow speed at the particle position l is self-dependent of the particle traveled distance l . Hence, the particle traveled distance expression is a differential equation (Equation 28) that is numerically solved using Matlab (R2016a, MathWorks, US) and presented in Figure 2.20.

$$\begin{aligned}
 l(t) &= \int v_{particle} dt = \int (v_{cell, sedim} + v_{flow}) dt \\
 &= \int \left(v_{cell, sedim} + \frac{Q_d}{A_{aperture} + 2\pi l} \right) dt
 \end{aligned}
 \tag{Equation 28}$$

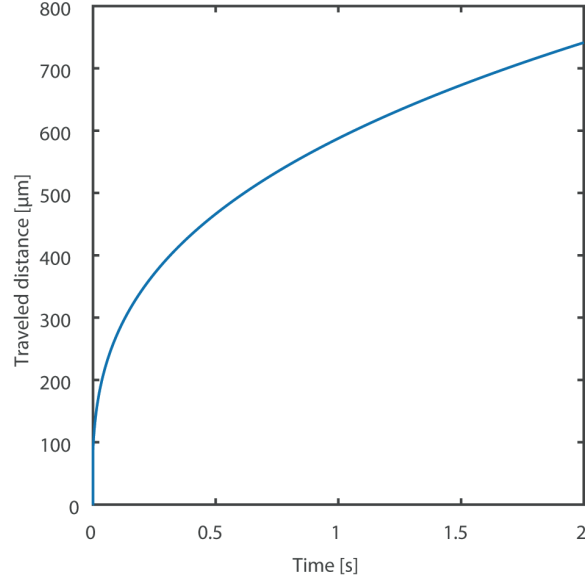


Figure 2.20 : Distance traveled by the particle when leaving the sensing tip. This curve shows the time required for the particle to reach the 472 μm escape distance. This determines the time delay of 0.5 s to be waited before the pressure switch to avoid particle re-aspiration.

Figure 2.20 shows that at least 0.5 second should be waited before switching from the dispensing pressure P_D to the holding pressure P_H to allow the cell to reach its escape distance of 472 μm . This defines the time delay t_{delay} to wait before switching the pressure in order to avoid the particle re-aspiration.

Considering this time delay t_{delay} of 0.5 s, a dispensing flowrate Q_D of 0.42 $\mu\text{L/s}$ and a particle concentration $C = 1000$ cells/mL, the probability of having further particles dispensed during this delay can be calculated by Poisson's distribution:

$$\lambda = C \cdot V_{\text{dispensed}} = C \cdot Q_D \cdot t_{\text{delay}} = 0.21 \text{ cells} \quad \text{Equation 29}$$

$$P(k > 0) = \sum_{k=1}^{\infty} \frac{\lambda^k}{k!} e^{-\lambda} = 0.181 \quad \text{Equation 30}$$

Equation 30 shows that, on average, 18% of the wells will be populated with more than a single cell because of the time delay before the pressures switching. These 18% of wells

containing two cells does not represents a reliability problem as they can be discarded based on the impedance time trace showing the passage of two cells. However, it defines the maximal ratio of wells that can effectively contains a single cell and represent a maximal filling plate rate of 82%.

To compare this results with the standard serial dilution and using the Poisson's distribution (Equation 31), Figure 2.21 shows the probability of having k cell per well for different cell concentration and a dispensed volume fixed at 100 μL per well.

$$P(k) = \frac{\lambda^k}{k!} e^{-\lambda} \quad \text{Equation 31}$$

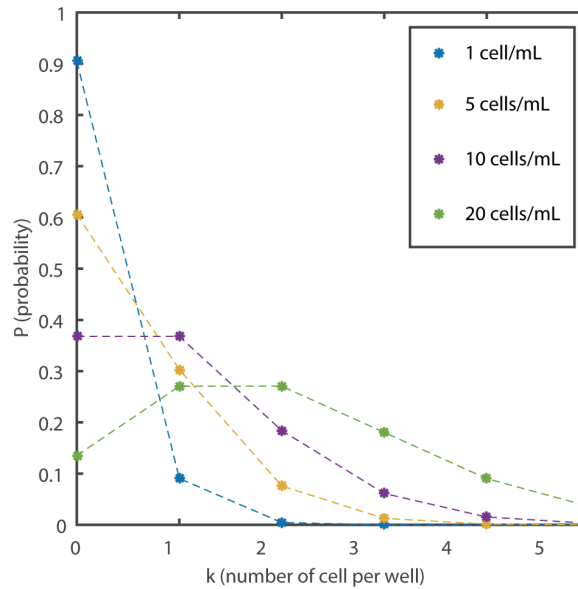


Figure 2.21 : Poisson distribution defining the average number of cell dispensed per well by serial dilution. This graph defines the highest probability to have single cell at 36.8%. This case happens for a cell concentration of 10 cells/mL and a dispensed volume of 100 μL representing, on average, one cell per dispensed volume.

According to the Poisson's distribution, the highest probability of having 1 cell per well is given when λ equals 1 cell per dispensed volume and yield at a maximum of 36.8%. This defines the highest plate filling rate that can be achieved by serial dilution and show that the feedback of the instrumented pipette, although not perfect, can permits a higher plate filling rate of 82%.

2.3.4 Single particle dispensing validation

The system was used to dispense 10 μm fluorescent beads (FluoroBrite, PolySciences, US) in well plates (96 & 1536 multiwell plate, Corning, US) to demonstrate its dispensing capability. Prior to dispensing, 20 μL of DPBS (DPBS 1x, Sigma Aldrich, US) containing 5×10^3 beads / mL were loaded in the sensing tip. To dispense a single bead, the tip was manually immersed in a well containing 150 μL DPBS for 96 wells plates and 6 μL DPBS for 1536 wells plates. The dispensing pressure of -0.3 mbar was applied in addition to the hydrostatic and capillary pressure. Once an impedance peak was detected above the threshold $Z_{Th} = 20 \Omega$, the system waited for the time delay $t_{delay} = 500 \text{ ms}$ to avoid re-aspiration of the bead and automatically switched to the holding pressure of -0.9 mbar to avoid further bead dispensing. The sensing tip was then manually extracted from the well and the impedance trace was recorded together with the well number.

Figure 2.22 a) shows an optical microscopy pictures (DM IL, Leica, GE) combining fluorescent (400 nm excitation) and bright field illumination of a well containing one single fluorescent bead successfully dispensed with the system. Figure 2.22 b) shows a typical impedance trace obtained during the dispense and displays the evidence of a single particle deposition with only one impedance peak between the entrance and escape of the well.

This dispensing was performed in 47 wells. Of these wells, 24 were rejected because the impedance traces showed more than one peak or insufficient impedance signal quality. The remaining 23 wells were selected as the impedance traces showed one single peak. All of these wells contained effectively only one single bead when observed under the microscope.

At this stage, the plate filling rate is not perfect with 49% ($n = 47$) of wells presenting the evidence of a single particle in the impedance trace. According to the previous section (§2.3.3.4) this is explained by the fluidic control that still has to be perfected to dispense single particles at higher yield. However, the important feature is the ability to define and qualify wells containing effectively a single particle with high confidence based on the impedance time trace. This was achieved with 100% ($n = 23$) of wells presenting effectively a single bead when the impedance time trace showed one impedance peak. This capability is made possible because there is no dead volume between the cell sensing volume and the receiving well. Consequently, each single particle leaving the sensing tip is detected and is necessarily in the well.

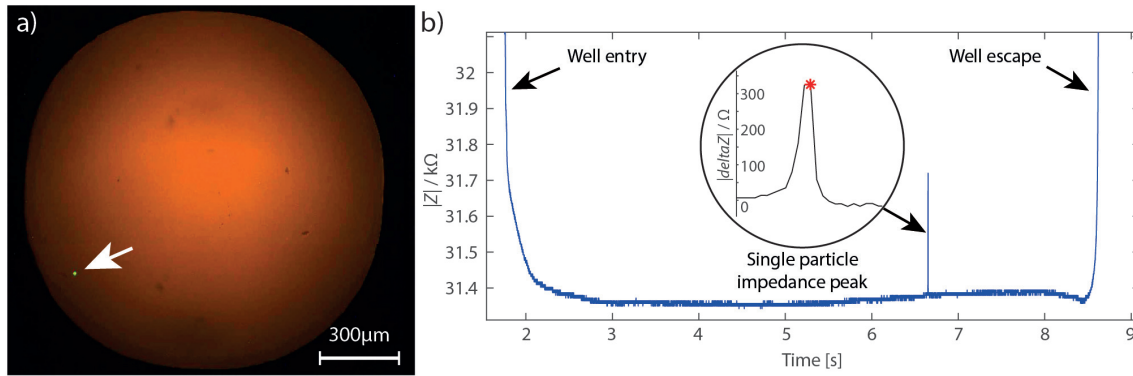


Figure 2.22: Demonstration of the system capability to isolate single particle in wells. **a)** Pictures of a well containing a single 10 μm fluorescent bead dispensed with the instrumented pipette and the sensing tip. **b)** Typical impedance trace (before low pass filtering) of a single particle dispensed in a well showing the impedance drop due to the entrance in the well, the single particle impedance peak due to the single particle dispensing and the impedance increase when leaving the well. As only one impedance peak is detected between the well entrance and exit, the system provides evidence of a single particle dispensed in the well.

2.3.5 Single particle dispensing reliability and plate filling rate

This section summarizes the different scenarios that can affect the single particle dispensing reliability and the plate filling rate. The ultimate goal of this system is to allow the dispensing of single particle on demand and to provide an impedance trace to attest on the number of dispensed particles in each well for traceability. The most important factor of such a system is the single particle dispensing reliability that is defined as the yield of well where one particle is observed when one particle has been detected in the impedance trace. This case is defined in Table 2.4 as the expected case. In the same table, all the other cases are exposed.

Critical cases for reliability consist of having more than one particle in a well when one impedance peak has been detected in the impedance trace. Those cases need to be avoided imperatively in the context of cell cloning where the uniqueness of the cell progenitor needs to be guaranteed (§2.1.1).

Different causes could lead to such a scenario. A particle impedance peak can be missed because its magnitude is below the detection threshold. In the previous section (§2.3.1.6), the probability of such an event for 6 μm particle and a threshold at $Z_{Th} = 20 \Omega$ is evaluated at

0.0016. If the population contains smaller particle or if this probability is not acceptable, the solution consists of decreasing the aperture size or decreasing the threshold level (§2.3.2.2). The flowrate should also be adequate to avoid a too fast particle passage preventing its detection (§2.3.1.6).

Alternatively, two or more aggregated particles could pass simultaneously the aperture leading in a doublet dispensing while one particle was detected. Two different approaches can prevent this case. The sample containing the cells should be adequately strained before the dispensing to avoid as much aggregates as possible. In addition, a second threshold at high value allowing discriminating particles with larger volume could inform on aggregated particle dispensed. Finally, a particle could be transferred from the previous well in addition to the particle being dispensed in the current well. Similarly, a particle could be dispensed while the sensing tip is outside the well. A simple workaround for these situations consists of washing the sensing tip prior every dispensing.

All the others scenario defined by no cell or more than one cells detected in the impedance trace do not affect the single cell reliability yield as the well can be discarded based on the impedance time trace. However, these cases decrease the plate filling rate defined as the number of well containing effectively a single particle over the total number of wells. The following causes lead to this situation. The noise in the impedance signal can be interpreted as a particle impedance peak. The probability of such an event was evaluated in a previous section (§2.3.1.4) at 1.3×10^{-8} occurrence per impedance sample. If the particle concentration is too high or if the system holding pressure is set at a too low value, particles can be dispensed during the delay of pressure switching. Also, if the system holding pressure is set at a too high value or if the delay before pressure switching is too short, the dispensed particle can be re-aspirated by the system. Those examples illustrate the need of a reliable fluidic control to ensure a good plate filling rate. Many other obvious factors can lead to low plate filling rate such as a dusty solution, clogged aperture, no particle in solution or a signal containing an excessive amount of noise or artifacts.

Table 2.4 : Single particle dispensing reliability and plate filling rate

Outcome	Particle detected	Particle observed	Results	Cause	Probability	Mitigation
Selected wells	1	1	Expected case			
		0	Decreases plate filling rate	Noise interpreted as particle	1.3×10^{-8}	Increase detection threshold, Decrease noise level
				Dust interpreted as particle	-	Medium filtration
				Missing a 6 μm particle peak Missing a 10 μm particle peak	0.0016 4×10^{-10}	Decrease detection threshold, Decrease aperture size, Decrease flow rate
		> 1	Single-cell reliability issue	Doublets (2 cells aggregated)	-	Cell preparation, Cell straining, Fix an upper threshold to discriminate big aggregate
				Particle transferred from previous well	-	Avoid cell sticking to the tip, Tip washing between wells
				Particle dispensed when the tip is outside the well	-	Tip washing prior dispensing Better fluidic control
Rejected wells	0	X	Decreases plate filling rate	No particle in solution	-	Increase particle concentration Wait longer in each well
				Aperture clogged	-	Decrease particle concentration, Increase aperture size, Cell preparation
				Flowrate too low	-	Better fluidic control
	> 1	X	Decreases plate filling rate	Multiple dispense after first detection	0.18	Decrease pump switching time, Decrease concentration, Better fluidic control
				Dispense during back pressure phase	-	Increase back pressure, Better fluidic control
				Particle re-aspiration	-	Increase pump switching time, decrease back pressure, Better fluidic control
	Signal with artifacts or excessive noise	X	Decreases plate filling rate	Fault during operation, Electromagnetic interferences	-	Increase protocol robustness, System electromagnetic shielding

2.3.6 Cell viability

When the cells cross the aperture of the sensing tip, they are exposed to an electric field and a fluidic shear stress. Potential adverse effects are discussed in this section.

As described in literature (Zimmermann, 1974), in an electric based cell detection system, the electric field applied to cells can have an effect on the cell viability by breaking down the lipid membrane. The membrane dielectric breakdown happens around a potential of 0.9 V on the cell membrane. Initial effects are a reversible opening of the cell membrane allowing ions or molecules to pass through the cell as defined by electroporation. Higher electric field values will induce a permanent destruction of the cell membrane leading to cell apoptosis (Zimmermann, 1974; Neumann, 1982). Both these effects need to be avoided in the instrumented pipette. Even though the reversible opening should not lead to cell apoptosis, a bias will be induced in the effective impedance change measurement because current will flow through the cell and thus induce an error on the cell size interpretation. Secondly, this effect could also lead to the intake of external molecules inside the cell as voluntarily performed during electroporation. Intake of foreign molecules is to be avoided as it could have a negative impact on the future cell life.

The passage of a 15 μm bead in the sensing tip induces a variation of 1340 Ω for a total impedance magnitude of 30 k Ω according to Figure 2.9. As this impedance variation during cell passage represents only 4.4% of the total sensing tip impedance, the potential distribution (§2.3.1.1) is assumed to be constant during cell passage. According to the potential distribution in the sensing tip structure from Equation 6, the maximal potential difference is estimated at 225 mV for a 15 μm cell when centered in the aperture as shown in Figure 2.23 a). Consequently the maximal electrical potential across the cell membrane could not exceed 225 mV, which is far from the 0.9 V expressed from (Zimmermann et al., 1974) and can be considered safe for the cells.

Considering a Poiseuille flow in the sensing tip aperture of diameter $d = 35 \mu\text{m}$ with a maximal flowrate $Q = 2.5 \mu\text{L}$ during dispensing (§2.3.3.3), the maximal shear stress applied on the cell when passing the aperture can be calculated using Equation 32 (Kirby, 2010) and according to the situation showed in Figure 2.23 b).

$$\tau_{Cell,Max} = -\mu \left. \frac{du}{dy} \right|_{y=R} = -\mu \left. \frac{d \left(\frac{2Q}{\pi R^4} (R^2 - y^2) \right)}{dy} \right|_{y=R} = \frac{4Q\mu}{\pi R^3} \quad \text{Equation 32}$$

Results are shown in Table 2.5 for the sensing tip as well as a comparison with the maximal shear stress observed in FACS for a flow speed of 10 m/s and a capillary diameter of 75 μm (Davies, 2007; Ormerod, 2008). Those results shows that both the sensing tip and FACS maximal shear stresses are in the same order of magnitude and suggests that the shear stress applied in the sensing tip is acceptable for the cells.

Table 2.5 : Maximal shear stress in the sensing tip and FACS during operations

	r [μm]	v [m/s]	Q [$\mu\text{L/s}$]	$\tau_{Cell,Max}$ [Pa]
Sensing tip	17.5	1.04	2.5	5.94×10^2
FACS	37.5	10	11	2.67×10^2

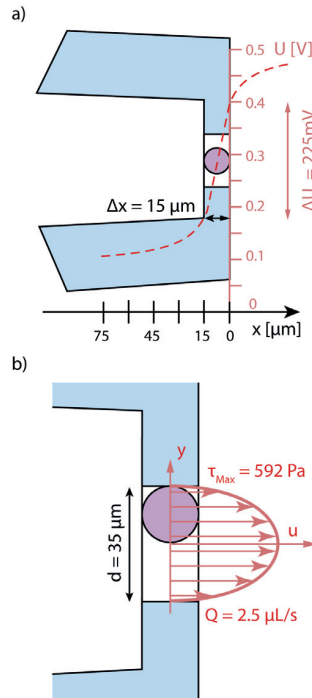


Figure 2.23 : Estimation of the electric field and shear stress applied on cells during dispensing. a) Using the sensing tip analytical model, the maximal potential drop on a 15 μm cell centered in the aperture is estimated at 225 mV. b) Assuming a Poiseuille flow and a flowrate of 2.5 $\mu\text{L/s}$, the maximal shear stress on a cell touching the aperture wall is estimated at 592 Pa.

To ensure these effects do not disrupt the cells, a cell viability assay was performed in which 3T3-J2 murine fibroblasts were stained with a viable dye (1 μ M Calcein AM, Thermofisher, US). In a first well (Grainer, Sigma Aldrich, US), one hundred cells were dispensed by serial dilution using a conventional pipette as positive control. In a second well, one hundred cells were dispensed using the instrumented pipette and the sensing tip. In the last well containing 20% ethanol, another hundred cells were dispensed by serial dilution as negative control. Each of the conditions were repeated in triplicate. The cells were then let to sediment for 30 min, allowing calcein to diffuse out of dead cells. The wells were imaged under an inverted fluorescent microscope (Axiovert 200M, Zeiss, DE). Images were analyzed and the number of green (living) cells versus unstained (dead) cells was manually counted. The ratio of those two counts was calculated for every condition in order to estimate cell viability.

Figure 2.24 shows the results of the viability assay. After dispensing the cells with the instrumented pipette through the sensing tip, a portion of 94% of cells (standard deviation: 3 %, n=3, average: 62 cells in observable area) were counted as living cells. This result shows no significant difference in terms of viability with the positive control where 95% of the cells were found alive. In the negative control samples containing 20% ethanol, only 4% of the cells were green (living) confirming the efficacy of this test and a sufficient incubation time to allow the calcein to exit the dead cells. According to this experiment, cell viability is not affected by the instrumented pipette and the dispensing through the sensing tip.

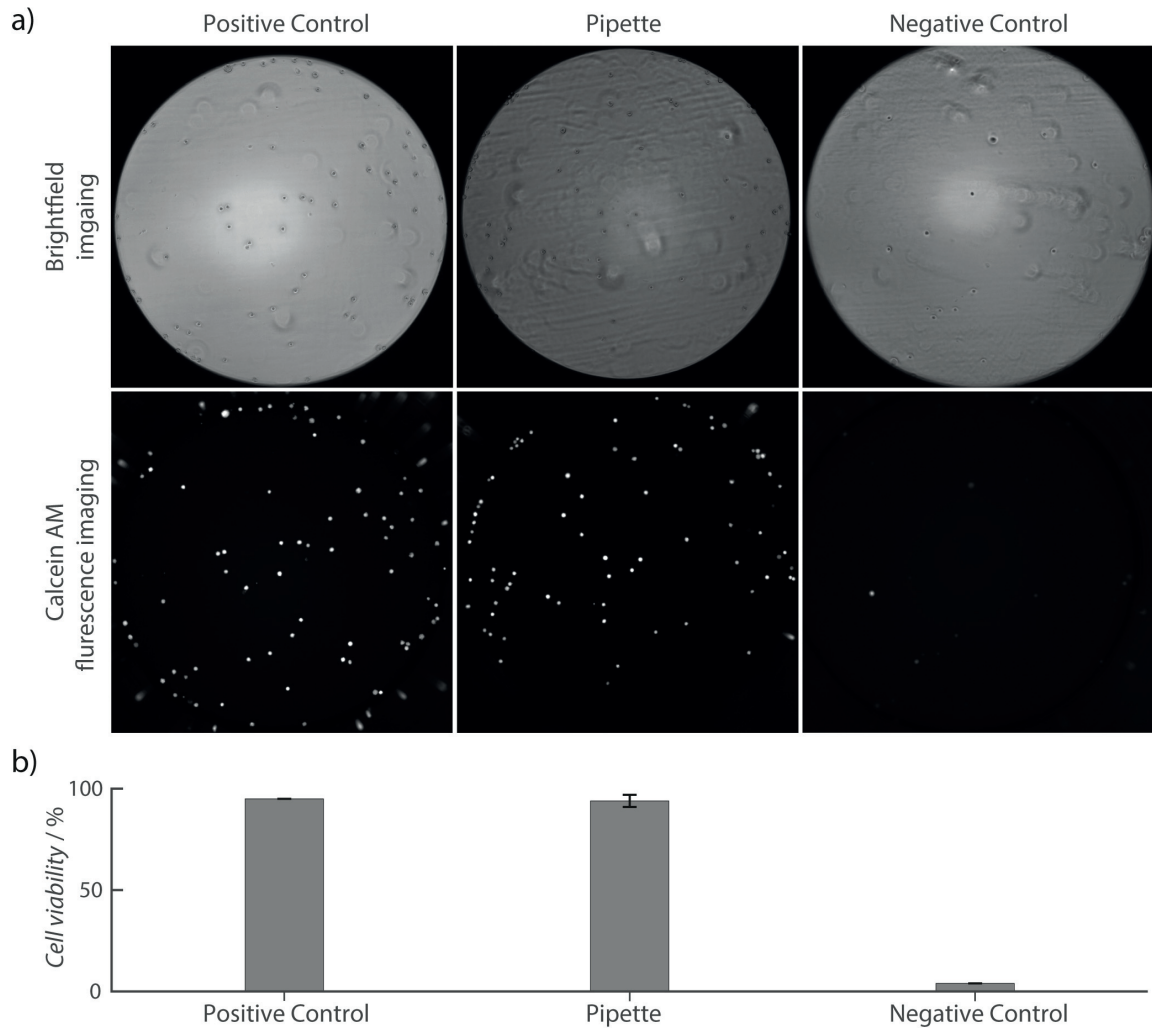


Figure 2.24 : Cell viability assay after cell dispensing performed with the instrumented pipette. a) Bright field and fluorescent images of the well containing the dispensed cells in the 3 conditions; positive control, instrumented pipette treatment, negative control. b) Cell viability for the same three conditions. This shows that the use of the instrumented pipette does not significantly alter cell viability.

2.4 Discussion

The tool proposed and designed in this study is effectively capable of detecting and sizing particles down to the single particle resolution. Thanks to the analytical model developed and validated with experiments, the sensing tip parameters such as membrane thickness

and aperture diameter have been optimized for reliable particle detection in a range from 6 μm to 15 μm in diameter. The instrumented pipette combined with the sensing tip have a limit of detection in terms of particle size of 3.2 μm for a sensing tip aperture of 35 μm . According to the system noise and the selected detection threshold, the probability to miss a particle bigger than 6 μm is smaller than 0.2% and becomes negligible for particle bigger than 10 μm . These performances are key to enable highly reliable single cell dispensing with most of the mammalian cells.

The choice of the Coulter counter topology fabricated at the extremity of a standard pipette tip is also determinant for single cell isolation. The dispensing of single cells is possible as the cell sensor is effectively formed by the tip membrane and thus leaves no dead volume between the particle detection volume and the receiving well. Performances of the system and its dispensing capabilities were validated using fluorescent beads. They showed to be highly reliable with 100% of single cells observed in the wells when a single peak is measured in the impedance time trace. Combined with the recording of the impedance time trace, it allows to provide evidence of the single cells isolation by quantifying the full content of the receiving well. Even though gene-editing techniques might permit in the future to remove the constraint of single cell isolation for cell line establishment, regulating agencies require today this isolation step and a proof of thereof for all the bioprocesses in the context of drug production.

Thanks to the simplicity of the Coulter counter topology, the sensing tip fabrication is cost-effective as most of the process steps are treated in batch and no photolithography or precise alignment procedures are required. This allows producing disposable sensing tips compatible with cell culture for a reasonable cost and in sufficient quantity for experimentation.

The ability of the cell sensor to be fabricated on an existing pipette tip ensures a design and materials choice compatible with cell handling. The sensing tip can be sterilized by gamma irradiation. Moreover, maintaining cells in the large sensing tip reservoir also prevents quick temperature and pressure changes, as it could be the case for microchannels or flying droplets. Similarly, the choice of designing such a tool in a pipette format prevents significantly disrupting biologists habits and should speed up its acceptance.

A cell viability assay using fibroblast showed that the instrumented pipette has no detrimental effect on cells when compared with standard pipetting. Further evidence of the

gentleness of this instrument and the corresponding approach was demonstrated by the cloning of single stem cells that were cultured and transplanted without loss of function by my colleague Georges Muller (Appendix §7.1)(Muller, 2016).

However, the experiments performed during this work, highlighted two main limitations of this initial version of the instrumented pipette. As demonstrated, the fluidic control is not optimal because of the limited sensing tip hydraulic resistance. The range of applied pressure has the same order of magnitude than the tip hydrostatic and capillary pressure complicating the flowrate control.

Even though this weakness does not impact the reliability of the method experimentally measured at 100% (§2.3.4) and defined as the wells contained effectively one particle when one impedance peak was observed in the impedance time trace, it leads to a sub-optimal plate filling rate. The theoretical maximal plate filling rate is estimated at 82% but also assumes a pressure control with the microbar precision in addition to the measure or estimation of the actual tip loaded volume. In the current instrument embodiment, experiments showed a plate filling rate of 49%.

Both these theoretical and experimental plate filling rates are higher than the maximal plate filling rate obtained by serial dilution which is 37%. Nevertheless, a perfect fluidic control permitting the total stop of the flowrate with a short response time could allow reaching a plate filling rate close to 100%. This could be easily improved by increasing the fluidic resistance of the sensing tip.

Chapter 3 : Cost Effective and Large Scale Manufacturing of Flow Cytometers

This chapter is adapted from the following work and publications:

D. Bonzon, T. Braschler, Luc Aeberli, Marc Lany, Guillaume Petit-Pierre, P. Renaud. (2017). Assessing the use of Printed Circuit Board production lines for BioMEMS prototyping and production. *Article in preparation*.

Bonzon, D., Lany, M., Van Neyghem, N., Aeberli, L., Choppe, J., Muller, G., & Renaud, P. (2017). Method For Manufacturing A Microfluidic Sensor. *Patent application PCT/IB2017/051385*

3.1 Introduction

The previous chapter showed the ability to produce a sensing tip for single single cell dispensing in batches of hundred pieces or more and for a cost below 10 CHF per parts. During this work, this achievement was critical in order to produce enough sensing tip to use them as consumable parts. This consumable aspect is a fundamental requirement to be compatible with cell culture.

During the experimental part of this thesis, every simple dispensing experiment was requiring between 2 to 5 sensing tips per repeat and test condition. The consumption of sensing tip in large-scale biological validation is expected to be even more important. Furthermore, the ability to produce the sensing tip at low cost and large volume would be critical in an industrial context or a clinical use of the sensing tip.

The previous chapter highlighted the strength of the sensing tip for particle detection but suggested possible improvement in the fluidic control currently achieved with the sensing tip. One option to decrease the influence of uncontrolled factors such as capillary or hydrostatic pressure on the flowrate is to simultaneously increase the applied pressure and the hydraulic resistance. High hydraulic resistances are conveniently achieved in conventional planar microfluidic chip by designing channels of sufficient length.

In this chapter, alternative planar flow cytometer designs are proposed and fabricated using the Printed Circuit Board (PCB) fabrication capabilities to enable large volume and cost effective production as required for disposable devices.

Since its invention in the early 1900s, PCB fabrication has become a robust standard in the electronic industry and led to a continuous development of this technology. At the end of the 20th century, PCB tracks resolution were reaching the 100 μm and fabrication process was sharing many similarities with MEMS fabrication including photolithography and etching techniques. Consequently, researchers started to take advantage of PCB technologies to create microsystems. Nguyen *et al.* demonstrated a micropump based on a commercial PCB supplemented by piezo discs soldered onto the copper pads (Nguyen, 2001). Wego *et al.* demonstrated the possibility to create fluidic channel by directly using the PCB copper tracks with a laminated polymeric foil on the top (Wego, 2001). Alternatively, some

microfluidic chips were also fabricated in PDMS by soft lithography using the PCB copper tracks as master (Li, 2003). Other researchers used existing PCB materials such as the photostructurable dry film resists to define the master for softlithography (Stephan, 2007) or to directly create the microfluidic network on a custom substrate such as glass or silicon (Vulto, 2005). Other microfluidic chips were based on a PCB substrate on which a microfluidic layer made of SU-8 (Kontakis, 2009; Guo, 2014) or PDMS (Marshall, 2012) was subsequently added.

If purely electro-mechanical MEMS including pressure sensor, accelerometers and gyroscope are largely based on CMOS compliant process and largely benefited from the CMOS design and process standardization (Hierold, 1996; Pakula, 2004), it is far from being the case for BioMEMS. BioMEMS is a growing family of microsystems targeting biological and medical applications (Bashir, 2004). Amongst many applications, examples of BioMEMS are flow cytometer chips, liquid handling chips and electrode arrays. Flow cytometers are used for cell counting, analyzing and sorting with main applications in rapid analysis of a large cell population such as hematology (Givan, 2001; Gawad, 2001). Electrode arrays are used for tissue electrical signal recording or stimulation. Rigid multi-electrode array (MEA) where first developed, on which cells were cultured (Gross, 1977) and more recently, electrodes made on flexible probes steered this technology towards direct implantation (Boppart, 1992; Cheung, 2007). Even though the BioMEMS family was inspired from the initial MEMS in term of design, they have their own specificities and constraints. The microchannels they accommodate are generally in the range of tens of micrometers in width, such that they can be used with cells in suspension. Fluidic in- and outlets are much bigger than the electrical pads used for wire bonding in CMOS chips. Polymeric flexible substrates are the material of choice to interface cells and soft tissues. BioMEMS chips generally have a total surface in the order of square centimeters which is much larger than integrated electronic chip. On the other hand, BioMEMS can generally be produced with far lower resolutions than standard CMOS processes. Even if BioMEMS fabrication can benefits from well-established manufacturing technique such as injection molding, hot embossing and metal deposition methods (Greener, 2006; Attia, 2009), the wide range of design and materials as well as their specific function makes it difficult to define standardized process for manufacturing. Current efforts are going toward design (van Heeren, 2015) and process standardization to facilitate BioMEMS commercialization (Volpatti, 2014; Temiz, 2015).

In the last decade PCB tracks resolution decreased toward 20 μm thanks to photoresist material improvement and new exposition techniques such as Laser Direct Writing. Microvias also emerged using Direct Laser Drill techniques. The use of flexible substrate such as polyimide has become a standard. Consequently, PCBs are now sharing many similarities with BioMEMS; feature size are in the same order of magnitude (20 μm – 200 μm), their total surface can largely exceeds the range of square millimeters and the substrate can be flexible and biocompatible using polymers such as polyimide. Researcher recognized those advances and started to make microfluidic chips by stacking two or more standard PCBs and polymer layers (Wu, 2010). Recently, this technique was used by Vasilakis et al. (Vasilakis, 2016) to combine multiple PCBs and dry film resist layers to define at the same time electrodes and microfluidic channels.

Similarly to CMOS foundries, the PCB production lines use standardized processes to produce different PCB designs. However, to be compliant with a PCB production line many constraints are imposed on the design and materials to be used. In this chapter, we examine the possibilities and limitations of using a standard PCB fabrication line to produce a BioMEMS both for prototyping and production. The goal of this work is to employ the standard PCB production line to fabricate a BioMEMS, and in particular flow cytometer, integrating fluidic channels defined by the same dry film resist used for the PCB fabrication. To exemplify such process different BioMEMS chips were produced; an electrode array placed on a flexible probe tip and flow cytometers with two different topologies. These chips have a design adapted to PCB production constraints. The electrode array probe is presented and the compatibility of the different material used in the fabrication process with biological application is discussed. Flow cytometer chips are used to evaluate the PCB fabrication capability in term of resolution for microfluidic channel and metallic tracks. Finally, operations of flow cytometers are demonstrated with polystyrene beads and the design constraints for its fabrication in a PCB production line are discussed.

3.2 Materials & methods

The fabrication consists of a standard PCB process (Mitzner, 2009) in which two steps are repeated in order to add the fluidic layer to a PCB on which metallic tracks have been patterned to form the recording electrodes. The repeated steps for microfluidic channels definition are based on standard equipment and parameters as in the conventional PCB fabrication steps and are performed on the full PCB panel.

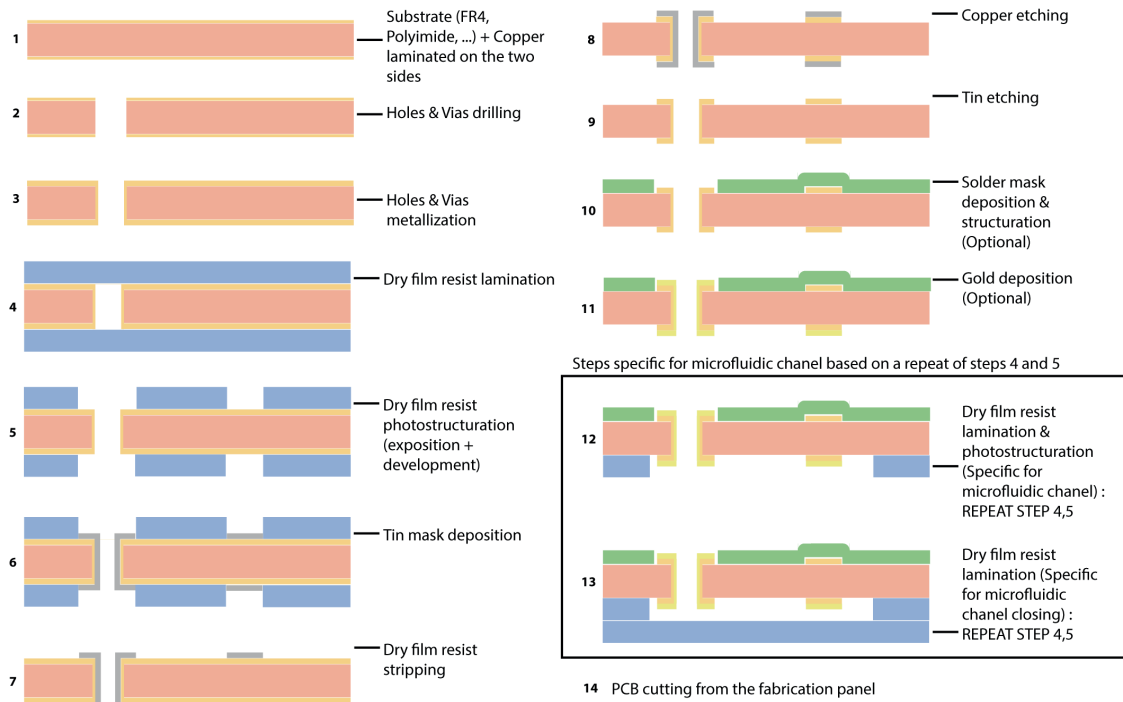


Figure 3.1 : Fabrication process used for manufacturing BioMEMS using a PCB fabrication line. Steps 1 to 11 are common to standard PCB fabrication. Step 12 and 13 are repeated from steps 4 and 5 to create microfluidic channels

The standard PCB process used in this work is presented in Figure 3.1 and starts with a 100 μm Kapton film covered by 18 μm of copper on both side (1) (Pyrallux, DuPont, US). Holes and vias are drilled by CNC machining (2) and metallized with 18 μm copper using electroless deposition (3). Dry film resists (KOLON Pk 1640, LifeStyle Innovator, KR) are laminated on both sides (4) and structured by photolithography followed by the resist development (5). In this PCB process, tin is deposited as mask (6) through which the dry film resist and copper are etched (7 & 8). The tin mask is then etched (9). Optionally, a

photosensitive epoxy based insulating mask (Elpemer, Lackwerke Peters, DE) later called solder mask is deposited by serigraphy and subsequently photostructured (10). Also optionally, a layer of $\sim 5\ \mu\text{m}$ nickel and subsequently $\sim 50\text{nm}$ gold is chemically deposited (Hofstetter PCB Plating, CH) to cover the copper traces and pads (11). At this stage, a conventional PCB is complete with a substrate for mechanical stability in addition to metallic tracks, via and pads as well as a solder mask for the electrical insulation. Before the PCB cutting from the fabrication panel (14) and in order to fabricate the microfluidic layer of our BioMEMS chips on the same fabrication line, another layer of dry film resist is laminated and photostructured with similar equipment and parameters than used for the step (5). This repeated step defines the fluidic channels. The same step is repeated once again (5) but without photostructuration to deposit a layer of dry film resist to close the microfluidic channel. To demonstrate its compliance with a standard PCB fabrication line, all the PCB fabrication process, including the fluidic channel layer was outsourced to a PCB workshop at the exception of the last closing layer that was laminated in the lab to test different solutions for the channel closing.

3.3 Results

3.3.1 PCB production line fabrication capabilities

In order to produce BioMEMS containing fluidic channels and electrodes to interact with cells or tissue, we investigated the minimal channel and metallic track width that can be produced with the selected production line at EPFL.

Figure 3.2 illustrates the fabrication capabilities and limit of resolution of a standard PCB fabrication line. Figure 3.2 a) shows the liquid electrode flow cytometer design (§3.3.4.1). The chip design is embedded in a Gerber file, a standard format for PCB fabrication, including the two metallic layers (red & blue) for tracks and electrodes definition as well as the microfluidic layer (purple). Figure 3.2 b) shows a liquid electrode flow cytometer chip fabricated with the PCB process and used for analysis of process resolution described in this section. Figure 3.2 b) shows the PCB process resolution for microfluidic channel openings in the dry film resist (KOLON Pk 1640, LifeStyle Innovator, KR). Figure 3.2 c) shows the PCB

process resolution for metallic tracks made in the copper layer. Fabricated features were systematically 10-20% bigger than the design dimensions for features smaller than 100 μm and this effect was more pronounced for smaller features. Out of three chips of different batches, the minimal channel opening that was completely developed measured in average $45 \mu\text{m} \pm 0.5 \mu\text{m}$ with a design dimension given at 40 μm . Smaller dimensions down to 20 μm were usually not completely developed forming a u-shaped channel but probably usable to perfuse liquid with limited access to underlying electrodes. Similarly and out of 3 chips, the smallest metallic tracks width, with a spacing of similar dimensions between them, was on average 43 μm with a standard deviation of 1.8 μm for a given design dimension of 50 μm . In this later case, fabricated features were systematically 10-20% smaller than the design dimension.

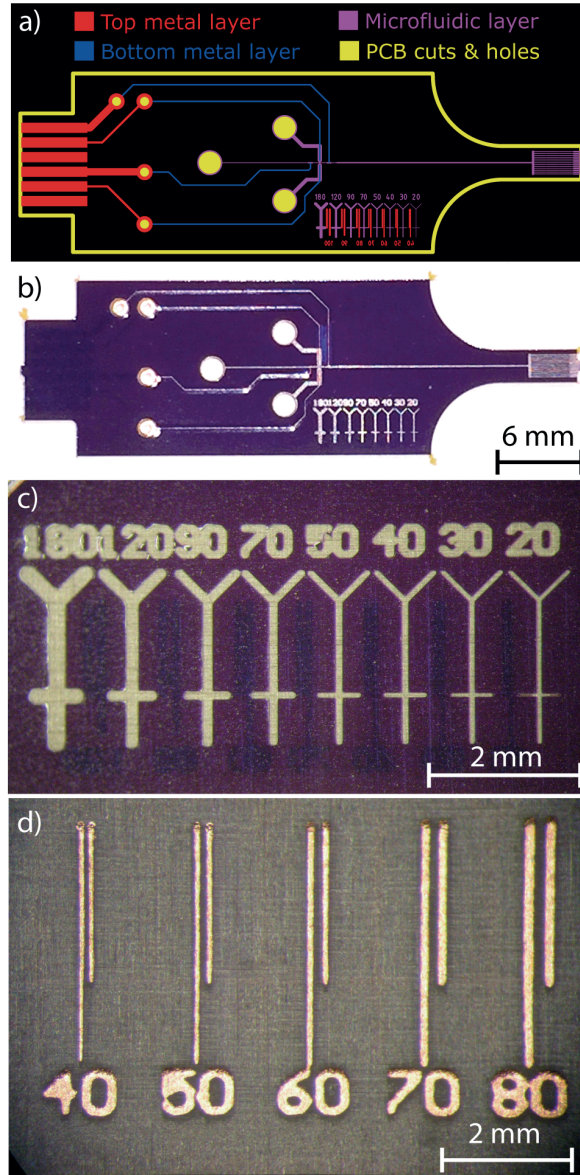


Figure 3.2: Fabrication capabilities of a standard PCB fabrication line used for BioMEMS applications. a) Gerber files defining a flow cytometer chip with top (red) and bottom (blue) metallic layers as well as the microfluidic layer (purple). b) Optical micrograph of the flow cytometer chip made with the PCB process. c) Test patterns allowing to identify the smallest feature obtained for dry film resist channels. d) Test patterns allowing to identify the smallest feature obtained for the metallic tracks.

3.3.2 Electrodes array probe fabrication and characterization

A flexible Multielectrodes Array (MEA) was designed in which the electrodes are patterned on a needle shape flexible substrate in view of its insertion in a biological tissue. The probe is 20 mm long and 1.2 mm in width. It includes six distal microelectrodes with a diameter of

200 μm and connected to proximal connection pads with 70 μm width conductive tracks as presented in Figure 3.3 a). Figure 3.3 b) shows the probe resulting from the standard PCB fabrication process with a 18 μm thick copper tracks and electrodes patterned on top of a 100 μm thick standard Kapton layer. Figure 3.3 c) is a SEM image showing probe tip details before the insulating layer (solder mask) deposition. Figure 3.3 d) shows the final probe tip details once the solder mask is deposited and structured to define the electrodes openings and provide electrical insulation of the tracks.

Electro-chemical behavior of the microelectrodes was characterized under physiological conditions. For this purpose, impedance spectroscopy was performed in a Phosphate Buffer Solution (DPBS 1x, Sigma Aldrich, US) against a macro copper counter electrode using an impedance analyzer (Agilent 4294A, Agilent technologies, US). Impedance magnitude and phase were recorded at frequencies between 1 kHz to 30 MHz. Figure 3.3 e) shows the equivalent electric circuit of the electrode–electrolyte interface with the DPBS solution. The interfacial capacitance can be approximated by a constant phase element (CPE) which describes the double layer behaviour while the charge transfer resistance (RCT) is the resistive element and models the electron-ion exchange at the electrode surface (Mercanzini, 2009; Altuna, 2012). These two elements are further combined in series with a spreading resistance (R_s) and a bulk resistance (R_{bulk}). Figure 3.3 f) shows the impedance spectra for the copper (continuous line) and gold covered 200 μm electrodes (dashed line). The resistive plateau located around 1 MHz dominated by the spreading resistance R_s for microelectrodes is measured at 3.2 k Ω . These spectra are similar to devices previously described in literature and characterized with the same method (Mercanzini, 2007; Merrill, 2005).

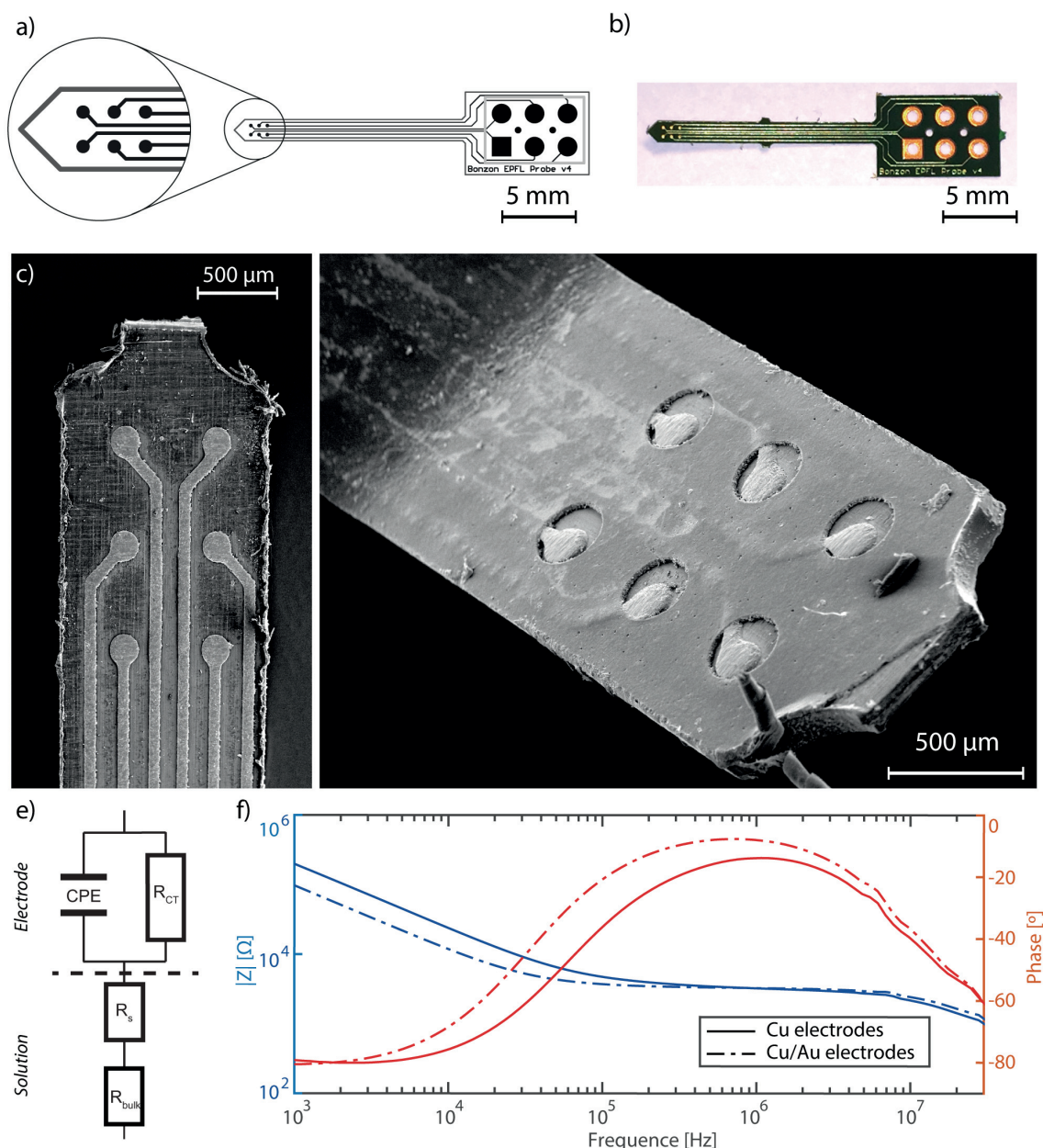


Figure 3.3 : Electrodes array probe. a) Design of the probe. b) Optical micrograph of fabricated probe. c) & d) SEM of the fabricated probe tip details showing the six microelectrodes. e) Equivalent electric schematic of the microelectrodes f) Impedance magnitude and phase of copper and gold covered microelectrode in DPBS.

3.3.3 Cell toxicity assay with the electrodes array probe

An assay for cell compatibility with the different materials used in the standard PCB fabrication process was performed. The electrode array probes shown in Figure 3.3 were fabricated in different batches with adapted designs to exhibit only certain features and

materials of the final probe. The first batch consists of the polyimide substrate only (PI). The second presents copper tracks patterned on the polyimide substrate (PI/Cu). The third has nickel-gold deposited on the copper tracks (PI/Cu/Au). The fourth has the solder mask as final step (PI/Cu/Au/SO). The following combination of materials were also produced; polyimide with copper tracks and solder mask but without gold deposition (PI/Cu/SO) and polyimide with the dry film resist only (PI/RI) as well as polyimide with solder mask only (PI/SO). All batches went through the complete PCB fabrication process and were consequently in contact with all the chemicals used for the entire process except the nickel-gold deposition that was performed on one panel only. PCBs of each batch were placed in one well containing 1 mL of cell culture media (DMEM + 10% FBS) and seeded with 20'000 cell/mL human foreskin fibroblasts, passage 10 as illustrated in Figure 3.4 a). Every combination was triplicated. Three wells were prepared as control with fibroblasts only.

Figure 3.4 b) shows the culture growth after 5 days of incubation at 37 °C using Alamar Blue (Invitrogen, DAL1025, diluted 1:10 in DMEM/FBS + 33mM HEPES pH 7.4) and an automatic plate reader (Spectramax Paradigm, Molecular Devices, fluorescence with kinetics mode, reads every 30 s, excitation 535 nm, emission 595 nm). The cell numbers were determined by comparison of the slope of the fluorescence signal from 10 to 30 minutes of incubation at 37°C to controls with known amounts of cells seeded 4h prior to the Alamar blue test. The cell growth was then defined as the number of cells observed after 5 days divided by the number of cells seeded (fold increase). The control showed a cell growth of 2.5 fold. In the wells containing the PCB made of polyimide only (PI), the cell density increases even more and reached 2.8 fold. This may be related to the extra surface offered by the probe in the well but essentially shows that the cell growth rate is not affected by the polyimide substrate that has passed through the whole PCB fabrication process. Similarly Figure 3.4 b) shows that the PCB batch made of polyimide with the solder mask only (PI/SO) does not affect the cell growth with an increase of 2.7 fold. Figure 3.4 d) & e) also shows that the cell morphology of the fibroblast cultured with the control and (PI/SO) batches do not significantly differ. Copper is cytotoxic and could be leached from the metallic tracks. We therefore quantified the concentration of Cu^{2+} ions in the cell culture media by use of a modified Bicinchonic acid assay (BCA, detection of Cu^{2+} via formation of a bicinchonic acid- Cu^+ complex in the presence of adipic dihydrazide as a rapid reducing agent). When bare copper is in contact with cell solution (PI/Cu), almost all of the cells died and nearly 2mM of free Cu^{2+} is measured as shown in Figure 3.4 c). Figure 3.4 g) presents the morphology of cells in the

(PI/Cu) batch showing that they do not adhere anymore and suggesting they died. Copper leaching can be substantially reduced by covering the tracks excepted the electrode, by a solder mask, and indeed, the cell growth is close to normal, with 2.2 fold increase over the 5 days of culture, which is only 20% lower than the control. Finally, adding a nickel-gold layer on top of copper (PI/Cu/Au) avoids microscopically evident electrode corrosion as shown in Figure 3.4 i) compared with bare copper electrodes shown in Figure 3.4 h), and strongly decreases concentration of copper in solution after 5 days as shown in Figure 3.4 c). Further, the combination of nickel-gold coating with a solder mask coverage (PI/Cu/Au/SO) for non-active areas allows restoring cell growth to slightly below control level (1.7 fold). Figure 3.4 f) also shows cells morphology obtained with the (PI/Cu/Au/SO) batch is similar to the cell morphology observed in the control well.

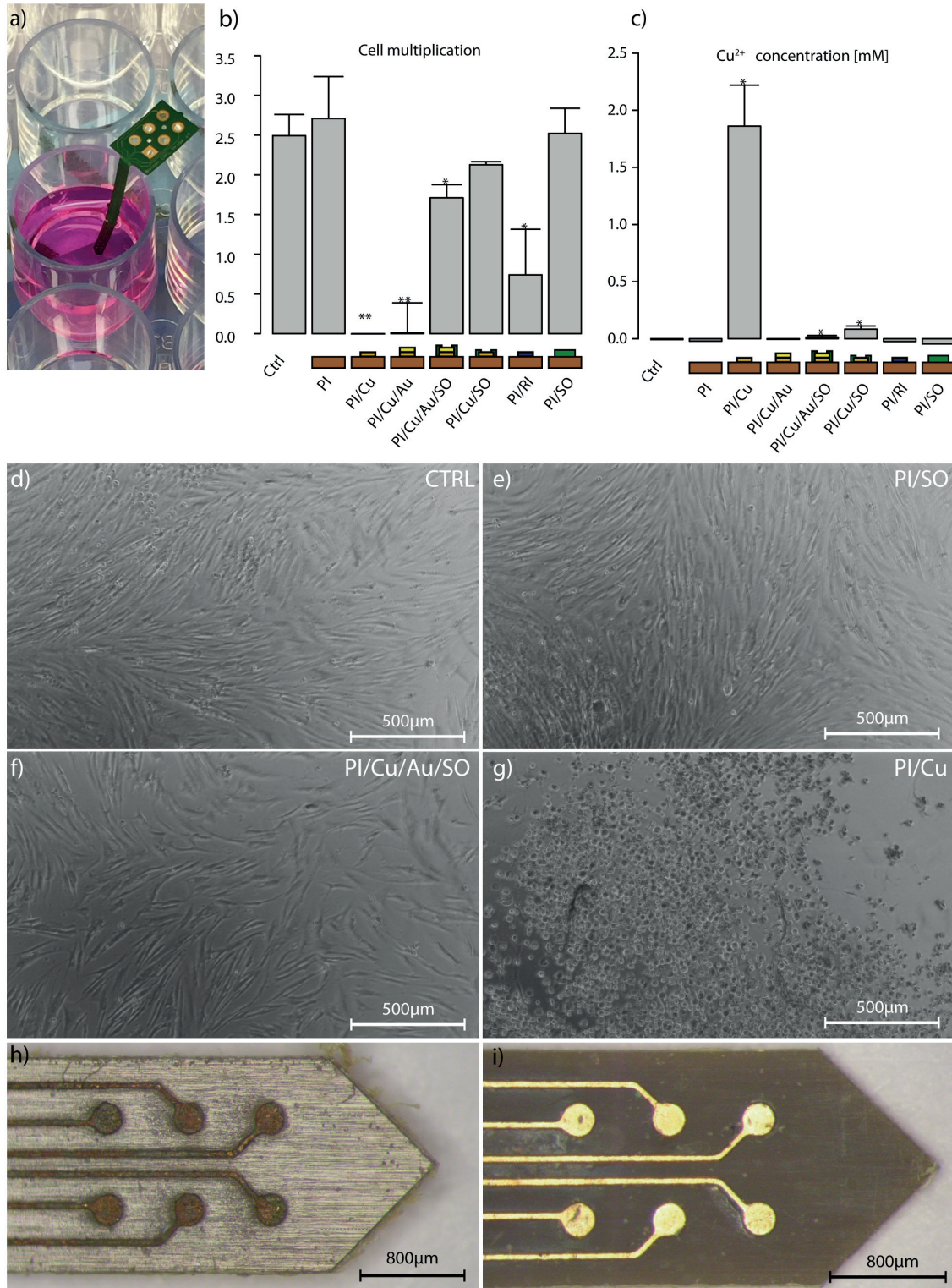


Figure 3.4 : Cell compatibility assay with PCB made test probes. a) Illustration of the test probe immerse in culture media. b) Fibroblasts growth after 5 days incubation with 7 different combinations of material used for PCB fabrication and the control without PCB. c) Copper concentration in the well for the 7 combinations of materials after the 5 days incubation. d) Optical micrograph of the fibroblast culture in the control well after 5 days incubation e) Optical micrograph of the

fibroblast culture with the polyimide and solder mask batch after 5 days incubation. f) Optical micrograph of the fibroblast culture with the bare copper batch after 5 days incubation. g) Optical micrograph of the fibroblast culture with the polyimide; copper, gold and solder mask batch after 5 days incubation. h) Bare copper and i) gold covered electrode optical micrograph after 5 days incubation.

3.3.4 PCB made flow cytometers and beads detection

3.3.4.1 Liquid electrode design

As a proof of concept for a BioMEMS fabricated in a PCB production line, a flow cytometer based on liquid electrodes topology (Demierre, 2007) is fabricated and presented in Figure 3.5. As shown in Figure 3.5 a), the chip design consists of metal electrodes placed in recessed cavities orthogonal to the main channel and filled with liquid. This topology allows constricting the electric current along the recessed channel to the flow cytometer sensitive volume in the main channel where it is used to detect particles. By limiting the resolution requirements to the microfluidic fabrication step, this minimizes the alignment problems between the metallic tracks and the fluidic channel. The main channel, in which particles will flow, has a width of 40 μm , whereas the perpendicular side channel that defines the liquid electrode is 28 μm in width and connects larger cavities in which the copper electrodes are provided. Despite an imprecise alignment of the copper electrodes with the side channel, this has no influence on the electrical current constriction and the electric field created in the flow cytometer sensitive volume. Figure 3.5 b) shows a Scanning Electron Micrograph (SEM) image of the fabricated chip.

To examine the functionality of the flow cytometer chip, 20 μm polystyrene beads dispersed in DPBS (DPBS 1x, Sigma Aldrich, US) were flown along the microfluidic main channel by applying a pressure of -2mbar at the chip outlet. One polystyrene bead passing the flow cytometer sensitive volume is illustrated in Figure 3.5 c). The impedance was measured using the lock-in demodulation principle and performed with an integrated lock-in (SI-QSD, Sensima, CH). On one electrode, an excitation frequency of 49 kHz with amplitude of 0.5 V_{pp} is applied, while on the second electrode, the current is amplified using a transimpedance amplifier (OPA2350, TI, USA). This amplified current is measured and the impedance is determined using the acquisition, demodulation and filtering capability of the integrated lock-in. The impedance signal is then recorded with a computer and filtered using a band pass filter between 0.1 Hz and 3 Hz according to the beads impedance peak signal bandwidth to be observed.

Figure 3.5 d) shows the impedance magnitude trace over time obtained when 20 beads of 20 μm diameter flows in the 40 μm microfluidic channel of the flow cytometer. Figure 3.5 e) shows the detail of two 20 μm beads impedance peaks comprising more than hundred measurement points each. The performances of the flow cytometer are illustrated by the scatter plot presented in Figure 3.5 f) showing a population of 20 identified events representing the beads and the other events representing the signal noise. Beads are defined by an average impedance magnitude of 61 Ω and a coefficient of variation (cv) of 11% and an average dwell time of 200 ms. The noise has a standard deviation of 4.6 Ω . In this context, placing a threshold at 28 Ω for particle detection and assuming a Gaussian distribution of the noise means that only 1 over 1.7×10^9 samples could be interpreted as a bead peak sample while being actually noise (see similar development §2.3.1.4). Similarly, the probability to miss an effective bead peak sample is less than 1 over 2×10^6 events.

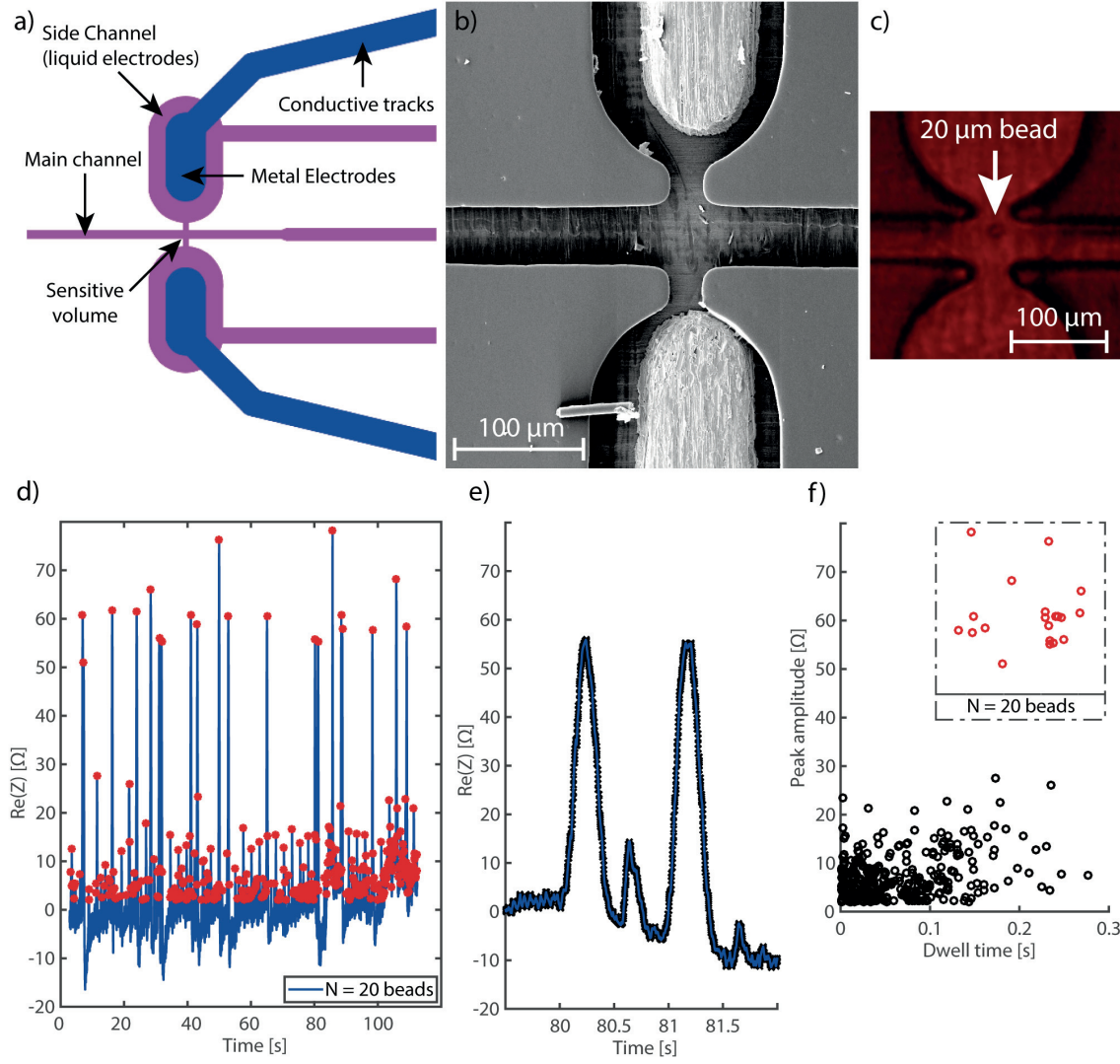


Figure 3.5 : Liquid electrode flow cytometer chip as proof of concept for a BioMEMS fabricated in a PCB production line. a) Design and b) SEM of the flow cytometer chip with liquid electrodes. c) Optical micrograph of the chip with a 20 μm bead flow in the sensing area d) Impedance magnitude signal over time of 20 μm beads suspended in PBS and flowing in the 40 μm microfluidic channel of the fabricated flow cytometer. e) Detail of impedance peak representing the passage of 20 μm beads in the sensing area. f) Scatter plot with the peak amplitude and dwell time of the 20 μm beads and noise measured with the liquid electrode flow cytometer.

3.3.4.2 Coulter counter design

One advantage of the liquid electrode based flow cytometer described above (§3.3.4.1) is its full compliance with standard PCB process. This fabrication process compatibility allows benefiting from the low cost and high volume capability of the PCB industry. However, its main drawbacks are the limitations in term of resolution and alignment between layers. This

restricts the design and topology choices. Even though, the liquid electrode design was satisfying as flow cytometer, adding an excimer laser (LSV3, Optec, BE) ablation step to the finished PCB allows solving part of these constraints by enabling the fabrication of specific features with smallest resolution.

The flow cytometer presented in this section is also fabricated on a PCB production line with fluidic channels made in the dry film resists. However, a similar topology as the one used in the sensing tip cell sensor is selected here. Similarly to the original Coulter counter, the flow cytometer described in this section is composed of an aperture separating two liquids filled volumes as shown in Figure 3.6 a). The upper liquid chamber consists of the chip gasket containing the chip inlet and outlet. This gasket is laser machined (H-Series, Full Spectrum Laser, US) in PMMA and glued on top of the PCB using double-sided tape (FLEXmount 25 μm , FLEXcon, US). The lower liquid chamber consists of a 100 μm wide and 80 μm height channel directly structured in the dry film resist during the PCB fabrication process. The pair of electrodes presents on each side of the substrate is part of the PCB and is created according to the PCB fabrication process. Using a laser excimer (LSV3, Optec, BE), the 100 μm polyimide substrate is thinned down to form a 12 μm thick membrane on a 196 μm diameter circular surface as shown in Figure 3.6 b). This ablation is performed with 615 laser pulses of 2 mJ, a beam attenuated at 50%, a shooting frequency of 50 Hz and through a 196 μm diameter circular mask. Using the same laser, a 15-20 μm elliptical aperture is opened in the membrane with 3000 pulse of 2 mJ, a beam attenuated at 18%, a shooting frequency of 25 Hz and through a 20 μm diameter circular mask as shown in Figure 3.6 c). These last two laser steps define by themselves the sensitive volume of this flow cytometer based on the Coulter counter topology.

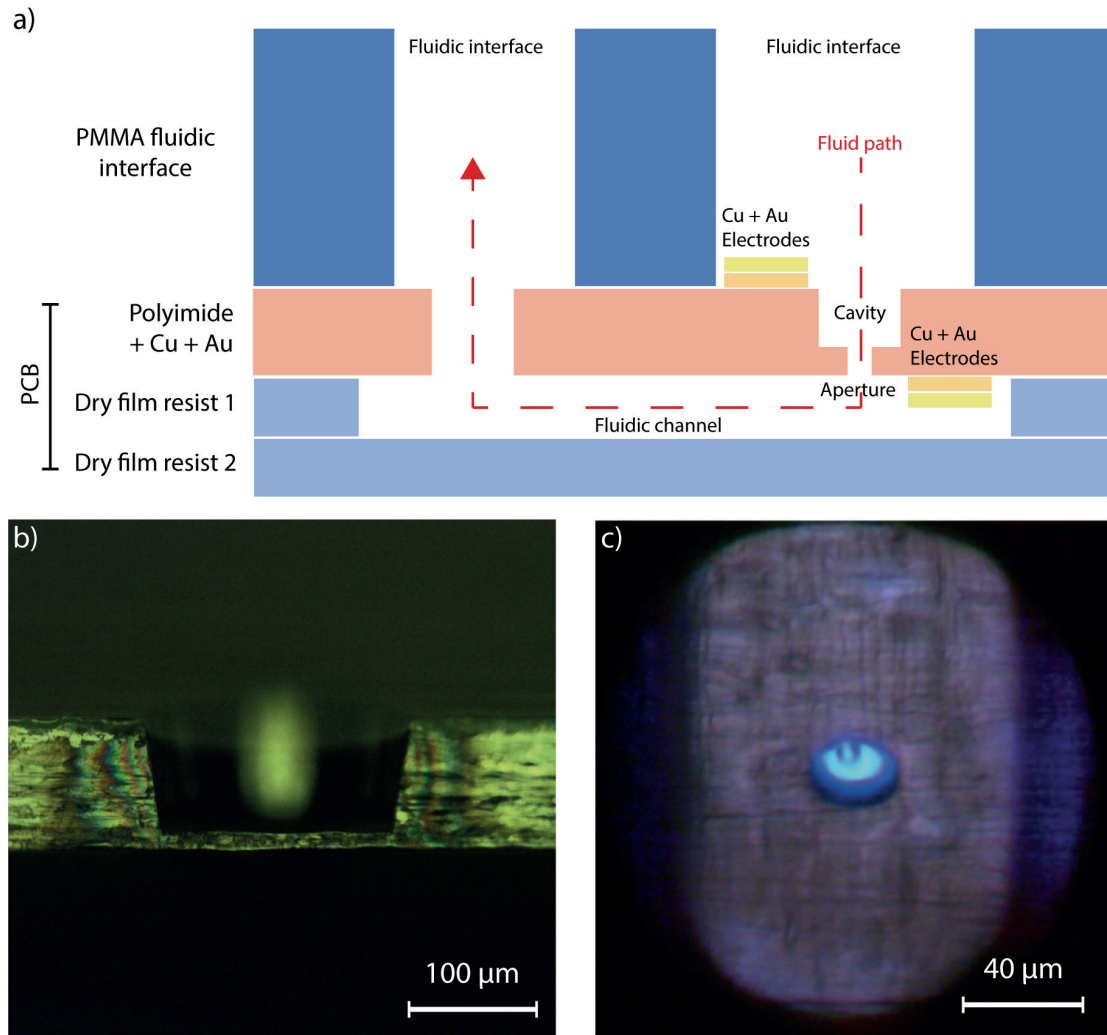


Figure 3.6 : PCB based Coulter counter. a) Design of the Coulter counter based on a PCB comprising two compartments and electrodes separated by a membrane. The upper cavity is defined by the chip gasket and the lower cavity is defined by a microfluidic channel embedded in the PCB. b) To define a flow cytometer sensitive volume adapted to the particle to be detected, the membrane is thinned by laser ablation in the PCB substrate. c) The Coulter counter aperture is opened in the membrane by laser ablation.

3.3.5 Performances & comparison with previous designs

In this thesis, three different topologies of flow cytometers are implemented and tested. The first implementation consists of the sensing tip integrating a Coulter counter (§2.2.1) as represented in Figure 3.7 a). The second implantation consists of the liquid electrodes based flow cytometer (§3.3.4.1) represented in Figure 3.7 b) and the last implementation consists of a Coulter counter made on a PCB (§3.3.4.2) represented in Figure 3.7 c).

Figure 3.7 d) shows the impedance time trace (real part) of 6 μm polystyrene beads passing the 35 μm aperture of the sensing tip. Figure 3.7 e) shows the impedance time traces of 20 μm beads passing in the 40 μm width channel of liquid electrode flow cytometer. Figure 3.7 f) show the impedance time trace of 8 μm beads passing in the 15 μm x 20 μm ellipsoidal aperture of Coulter counter made on a PCB. Those time traces also exhibits the noise level encountered in each implementation.

Figure 3.7 e), f) and g) shows respectively the averaged impedance time trace (real part) for each implementation. Those curves allow extracting the mean impedance peak magnitude and the particle dwell time for each flow cytometer topology.

Table 3.1 summarize the impedance peak magnitude of the three different topologies and their respective dwell time. The impedance baseline and noise of each solution is also experimentally measured and the bandwidth selected to obtain the signal shown in Figure 3.7 is reported. The volume fraction is defined by the volume of the bead divided by the sensitive volume of each flow cytometer. The ratio of the mean impedance peak magnitude divided by the volume fraction defines the sensitivity of each topology to particle volume.

This sensitivity to particle volume is found to be 12800 Ω and 26900 Ω in the case of the sensing tip and the Coulter counter on PCB. The liquid electrode topology presents a much lower sensitivity to particle volume with 654 Ω . The excellent sensitivity to particle volume of the sensing tip and Coulter counter topology is explained by the very low access resistance between the electrodes and the sensitive volume, the well controlled confinement of the electric current in the sensitive volume and the shape of the sensitive volume adapted to the particle morphology.

On the other hand, the sensing tip topology presents a dwell time of 2 ms that is very small compared to the 200 ms of the liquid electrode topology. A short dwell time requires an instrumentation with a much higher bandwidth to acquire a sufficient amount of points per impedance peak and results in a more noisy signal. The explanation is the low hydraulic resistance of the sensing tip because its only fluidic restriction is given by the aperture while the liquid electrode benefits from an important hydraulic resistance obtained with long fluidic channels. An interesting compromise is achieved with the Coulter counter on PCB with a higher sensitivity to particle volume than the sensing tip combined with an extended hydraulic resistance and particle dwell time. Furthermore, the hydraulic resistance of the

planar version of the Coulter counter can easily be increase with a design comprising longer channels.

Table 3.1 : Performances comparison of the different flow cytometer topologies: Sensing tip, liquid electrode and Coulter counter on PCB

	Coulter counter on Sensing tip	Liquid Electrode on PCB	Coulter counter on PCB
Particle size (volume)	6 μm (0.11 fL)	20 μm (4.2 fL)	8 μm (0.27 fL)
Aperture size (Sensing volume)	35 μm (14.4 fL)	40 μm (64 fL)	15-20 μm (2.9 fL)
Volume fraction (Particle / Aperture volume ratio)	7.8×10^{-3}	6.5×10^{-2}	9.3×10^{-2}
Mean peak magnitude	100 Ω	60 Ω	2500 Ω
Sensitivity to particle volume (Mean peak magnitude / Volume fraction)	12800 Ω	654 Ω	26900 Ω
Dwell time	2 ms	200 ms	15 ms
Bandwidth	1200 Hz	6 Hz	250 Hz
Noise	3.9 Ω	4.5 Ω	36 Ω
Baseline	33 k Ω	36 k Ω	80 k Ω
SNR	70.3 dB	43.2 dB	57.5 dB

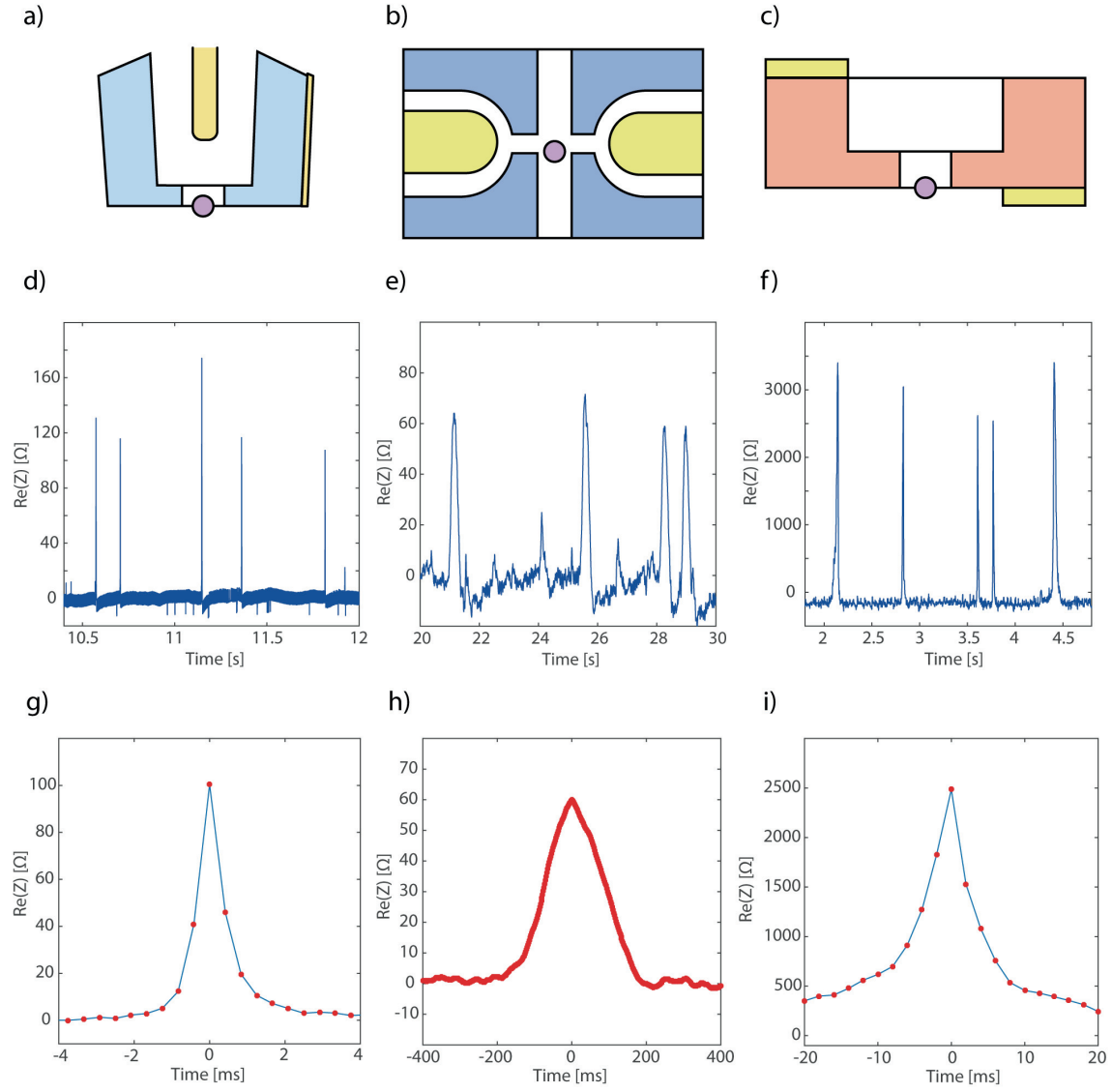


Figure 3.7 : Performances comparison between the different flow cytometer topologies. a), b) & c) presents the sensing tip, liquid electrode flow cytometer and PCB based Coulter counter. d), e) & f) shows an example of impedance peak obtained with the respective flow cytometer topologies. g), h) & i) shows the average impedance peak obtained with the respective flow cytometer topologies

3.3.6 Cost analysis

The production costs for the different flow cytometers are evaluated and summarized in Table 3.2. Details of the sensing tip fabrication costs are covered in a previous section (§2.2.5). Fabrication costs of planar flow cytometers such as the liquid electrode chip presented above (§3.3.6) are evaluated based on their surface in CMOS-compliant MEMS and PCB production settings. The planar flow cytometer based on liquid electrodes has a

total surface of 360mm² to accommodate the different fluidic features and outlets. The price per surface for CMOS-compliant MEMS process is evaluated based on the cost of the MEMS accelerometer for smartphone ADXL362. With a selling price of 5.90 CHF in large volume, its fabrication cost is evaluated at 10% of the price. This represents 0.59 CHF for a 4mm² die and yield 212 CHF for the 360mm² corresponding surface of the liquid electrode flow cytometer presented in this chapter. During this work, the liquid electrode flow cytometer chip was produced at the EPFL PCB workshop for 6.70 CHF per chip and is evaluated at 1.10 CHF per chip in an industrial PCB production line for a volume starting at 100 pieces.

Table 3.2 : Fabrication costs of the different flowcytometer topology using different fabrication processes

	Sensing Tip	Liquid electrode flow cytometers : (30mm x 12mm = 360mm ²)		
Process	Custom	CMOS compliant MEMS	PCB (EPFL workshop)	PCB (Industry)
Assumptions	(\$2.2.5)	ADXL362 4 mm ² die price 5.90CHF (1000 chips) cost: 0.59 CHF	200 mm x 150 mm pannel 30 chips cost: 200 CHF	100 chips cost : 109 CHF
Price per flow cytometer	CHF 7.99	CHF 212.00	CHF 6.70	CHF 1.10

3.4 Discussion

3.4.1 PCB fabrication processes for BioMEMS and flow cytometers

BioMEMS and flow cytometers presented in this chapter use a state of the art PCB fabrication facility with a resolution of 45 μm for both metallic tracks and fluidic channels made of dry film resist. Although this resolution is far from the processing capability of the CMOS industry or clean room processing, it is good enough for many BioMEMS applications. In these applications, features size are dictated by the object to be analyzed, which is a biological cell with dimensions in the range of 20 μm or a biological tissue that is even larger. In this context, the PCB resolution is well suited for a range of simple BioMEMS applications and in particular flow cytometers. During this work, using the EPFL PCB workshop to produce planar flow cytometer enabled to produce a sufficient amount of chips at a sufficiently reasonable cost to be treated as consumable device for the experiments. This approach showed to be efficient form the prototyping a disposable devices. Nowadays, some PCB manufacturers announce a resolution capability for metallic tracks down to 20 μm , two folds smaller that resolution presented in the present study.

However, as shown in this study, different constraints arise from the use of a PCB fabrication line to fabricate BioMEMS. The design needs to take these aspects into account to circumvent inherent technological limitations. PCB fabrication processes often use a mechanical pinning alignment system instead of an optical mask aligner, resulting in alignment tolerances in the range of tens of micrometers. For this reason we chose a flow cytometer topology inspired from the liquid electrode concept (Demierre, 2007) instead of the standard design with two electrodes in the channel (Gawad, 2001) to avoid the alignment constrains between the metallic tracks and the fluidic channel. In the liquid electrode topology, the fluidic channel geometry defines the detection performances which allows the use of larger electrodes and minimizes the importance of their placement. The current fabrication capability of the PCB process is not directly suited for any BioMEMS fabrication, but by adapting their design it is good enough for producing components that can be used for many BioMEMS application such as flow cytometers, which are of particular interest in this study.

Another important constraint of using the standard PCB fabrication line to produce BioMEMS is the restricted choice of materials. The polyimide substrate which is standard in PCB fabrication is a biocompatible material and frequently used in different neural interfaces (Lee, 2003; Lacour, 2008). This study also confirmed that a polyimide substrate that went through the full PCB fabrication process and its related chemicals kept its cell compatibility. However, the most common material for metallic trace in a standard PCB process is the copper, which is toxic for the cells and can consequently be used only when the performed BioMEMS analysis is an end-point measurement. The choice of material becomes critical when BioMEMS are in contact with a living tissue. The use of a solder mask which presents a good compatibility with cells and covers copper tracks significantly reduce copper cytotoxic effects. Surprisingly, an additional nickel-gold coating layer did not significantly further improve the cell compatibility. Even though the amount of copper released in solution strongly decreased with the nickel-gold coating, the cell growth did not improve. Nevertheless, the nickel-gold layer limits the electrodes corrosion. The problems of biocompatibility of the metallic tracks in PCBs can however be solved by using alternative PCB manufacturing methods that use noble metal only for metallic tracks and biocompatible material such as polyimide or liquid crystal polymer (LCP) as substrates. This configuration provided PCB-based implant with excellent properties for direct implantation at substantially reduced costs (Schulze, 2014).

For every BioMEMS application that can accommodate those constraints, advantages are numerous. First, PCBs are processed in large panels and the production is driven by the important electronic market. PCB fabrication costs are typically below 1 cent per square millimeter for small batches of 100 pieces or more. The combination of volume capabilities and production cost enable the production of consumable device. This cost is certainly interesting compared with the one of MEMS foundries. Moreover, only a small number of components need to be produced to reach this level of price compared with injection molding. Thus the PCB industry also represents an interesting alternative for prototyping of disposable BioMEMS devices such as flow cytometers with potential for large scale production.

Finally another interesting advantage that BioMEMS production could inherit from PCB industry is their standardization in the design-to-production pipeline. Similarly, in the CMOS industry, an IC designer focuses on the design and rely on a standard and well defined process. As long as the design is CMOS process compliant and, thanks to the

standardization of this technology, the steps from the designing phase to the production are simplified, as no process development has to be undertaken. A similar advantage appeared in this work for the chips produced on the PCB production line. The chip design was adapted to be compatible with the standard PCB process and consequently no effort had to be conducted on the process development. The production of the chip is then fully defined by the standard Gerber files and can be performed by different PCB manufacturers without process specific instructions except the repeat of the dry film resist deposition and structuration of the microfluidic layer, which are already existing steps in the line. This is certainly an advantage when the end goal of a research project is to reach industrial applications. Along with the simplicity of production management, comes the advantage of outsourcing the production to partners being already certified for their production line and processes.

3.4.2 Planar flow cytometers

In a more general fashion and irrespective of the method of production, planar designs of flow cytometers studied in this chapter present different advantages over the sensing tip described in the previous chapter (§2.2.1).

On a planar microfluidic design, high hydraulic resistances are easily achieved simply by increasing the channel length. As demonstration, the liquid electrode flow cytometers presents a limited and controlled flowrate with particle dwell time of 200 ms allowing the acquisition of more than 400 impedance measurement samples during particle passage at a sampling frequency of 2.4 kHz.

The specific design of the liquid electrode flow cytometer shows a smaller sensitivity to particle size and consequently a higher limit of detection than the sensing tip. This difference in performance is explained by a higher access resistance and a sensitive volume shape less adapted to the particle morphology to be analyzed.

However, the advantage of the high hydraulic resistance achieved on planar design and the high particle sensitivity observed for the sensing tip can be combined together as demonstrated in the planar Coulter counter integrated on a PCB substrate. This planar Coulter counter topology is also more suited to place the flow cytometer sensitive volume at the interface of the chip, to avoid dead volumes and enable reliable single particle dispensing as performed with the sensing tip. However, this topology requires an additional

process step of laser ablation that is not yet a standard in PCB production lines but that could be performed by PCB manufacturers equipped with technologies allowing for laser ablation of microvias.

Integrating the sensing tip principle on a planar substrate could also further decrease the chip stray capacitance as smaller area of liquid at different potential are facing each other. This could enable impedance spectroscopy in frequencies ranges above the 500 kHz observed in the sensing tip and permit label free analysis of parameters such as cell viability during their isolation. A planar fabrication could also allow the integration of more complex features such as cell sorting mechanism to dispense only cells of interest while staying cost effective and disposable devices.

Chapter 4: Impedance Spectroscopy for Active Cells Analysis

This chapter is adapted from the following work and publications:

Bonzon, D., Bargeton, B., Benton, R., & Renaud, P. (2016). Xenopus Laevis oocyte based Biosensors. *Nano-Tera Annual Meeting 2016*

Bonzon, D., Bargeton, B., Benton, R., Giovanna, Z., & Renaud, P. (2014) Xenopus Laevis oocyte based Biosensors. *Nano-Tera Annual Meeting 2014*

4.1 Introduction

For more than three centuries, different methodologies were developed to investigate electrophysiology and understand fundamental phenomena such as information transmission in nerve, action potential mechanism in cells and related conductivity modulation of membrane ionic channels (Verkhatsky, 2006; Martina, 2014). Modern electrophysiology and the current instrumentation principles were initiated with the discovery of the giant squid axon (Young, 1936). In the 1930s, a major step was achieved with the first insertion of microelectrodes in squid axons for direct measurement of resting and action potentials (Hodgkin, 1939). A technique called voltage clamp was developed based on an instrumentation allowing to measure electric current while imposing an electric potential at the cell membrane (Cole 1949, Marmont 1949). This technique was used for membrane current measurement at rest and during action potential allowing to perform a break-through in the understanding of membrane excitability and the related modulation of the different ion channel families (Hodgkin, 1952). Nowadays, this method is still a gold-standard for ions channel characterization as it allows clamping the cell to a non physiological electric potential and measuring the current-voltage dependence which is of primary importance for voltage gated channels. This technique also presents a good accuracy and a sufficient time resolution required to record fast ion channel modulation.

After long years of development and improvement (Hamill, 1981), the patch-clamp technique was provided with the unique capability of measuring the current of a single ion channel opening thanks to an giga-ohm sealing between the glass patch-clamp pipette and the cell membrane. Amongst many discoveries, this allowed to measure the current in a single ion channel such as the acetylcholine receptors. In addition, this technique opened the possibility to conduct electrophysiological recordings in small cells. Moreover, the high seal impedance and low impedance of the recording electrode allows conducting voltage clamp experiments with a single electrode.

In parallel, thanks to Micro Electro Mechanical Microsystem (MEMS) advances, microfabricated array integrating hundreds of microelectrodes (MEA) were developed to decorate the floor of tissue culture chamber. This allowed the simultaneous and long-term measurement of a large number of neurons with the ability to pickup the firing activity of

one single unit (Gross, 1977). This principle allowed to further understanding the neural network development and its respective function.

Both patch-clamp and MEA techniques allow cell electrophysiology recording without the need of inserting an intracellular electrode. However, this novel feature was provided at the cost of cell membrane segmentation and a high seal impedance defined between the membrane segments (Hamill, 1981; Spira 2013).

The collection of methods described above permits a large part of the current understanding in electrophysiology while staying methods mainly suited for laboratory and experimental studies as the procedure is often delicate, cumbersome, time consuming and invasive. However, membrane ion channels are implicated in a wide range of disorders and represents interesting targets for drug discoveries (Dunlop, 2008). Consequently, new needs emerged for high-throughput ion channel screening targeting the drug discovery or potential drug side effects assessment. For this purpose, the cellular models *Xenopus laevis* oocytes has established as gold-standard because of its ability to express a wide range of proteins combined with its large size that facilitate its handling (Barnard, 1982; Miledi, 1982; Dascal, 1987; Gudron, 1971; Weber, 1999). To perform the recording, a method called Two-Electrodes Voltage Clamp (TEVC) was adapted from the voltage clamp technique with the use of one pairs of electrodes allowing to sustain larger currents required for large cells such as *Xenopus Laevis* oocytes (Stühmer, 1998). For high-throughput drug screening, the procedure needs to be quick, efficient and reliable. This problem was solved by automation of the classical TEVC method performed on *Xenopus laevis* oocytes. One example is the OpusXpress 6000A (Axon Instrument) that performs automatically the TEVC recording of 8 oocytes in parallel. Another examples used nowadays in industry are the Robotcyte (MCS) and the HiClamp (MCS) that fully automatize the oocyte loading, electrode impalement and electrophysiological measurement allowing to serially test up to 96 oocytes against 96 chemicals compound in one run (Fejtl, 2003).

More recently, biosensors development started to benefit from advances in electrophysiology. The basic principle of a biosensor is involving a molecular recognition system instead of a simple physical adsorption as recognition principle for the sensor. The use of this molecular recognition system solves intrinsically the sensor selectivity issue. One of the first examples of biosensor is the enzyme electrode based disposable glucose sensor largely used nowadays for people suffering from diabetic condition (Updike, 1967). Lately, more complex biosensors evolved toward bioreporters whose molecular recognition system

is constituted of a living organism such as a cell (Werlen, 2004). King et al. (King, 1990) provided one of the first demonstrations where naphthalene was detected using bioluminescence of a genetically modified *P. fluorescens* bacteria. Bioreporters offer many advantages with the use of living organism as part of the transduction mechanism. In addition to the high specificity obtained with the molecular recognition, the living organism directly constitutes a natural amplification of the signal. This solves a part of the transduction requirement and dramatically expand the limit of detection (Van der Meer, 2010). However, the main drawback of this principle is the long induction time (Merulla, 2010) (Buffi, 2010) required by cellular signaling or regulator pathways to take place for the signal transduction.

Another kind of biosensors enabling faster time response by taking advantage of electrophysiology was proposed by Shear et al. (Shear, 1995). His biosensor was based on a *Xenopus laevis* oocyte microinjected with RNA expressing ligand-gated ion channels chosen to recognize a specific chemical compound. When this chemical compound binds to the ion channel ligand-gating domain, the ion channel opens and changes the membrane ionic permeability. Permeability changes are detected using the classical TEVC method. The time response of this system is fast as defined by the kinetic of the ligand-gated ion channels, which is usually within ten to hundreds of milliseconds. This concept was further explored by Misawa et al. (Misawa, 2010) by developing a selective odorant sensor with detection limit as small as a few parts per billions for volatile compounds. This principle is promising for highly sensitive, specific and fast biosensors but remains the problem of the classical TEVC method and oocyte electrode insertion that prevents building fully integrated and long-term capable electrophysiology based biosensor. To perform electrophysiology on longer time scale ranging from hours to days, the method needs be non-invasive without causing modifications of the intracellular conditions of the cell. Micro-electrodes impalement that is not tolerant to acceleration and shocks should be avoided.

An method without electrode impalement for cell electrophysiology measurement was proposed by (Siegel, 1997). This method consists of genetically encoding a fluorescent probe as membrane protein allowing to measure trans-membrane potential by fluorescence in single cell. Modified Green Fluorescent Proteins (GFP) were fused into voltage-sensitive potassium channels to induce a cell fluorescence depending on the voltage-dependent rearrangement of the channels and allowing a characterization of the cell membrane

potential. Recently, this technique allowed measuring single action potential and sub-threshold electrical events in neurons (Jin, 2012).

Dahan *et al.* (Dahan, 2007; Dahan, 2008) proposed another approach toward none-invasive oocytes measurement based on an Ussing-like chamber where an oocyte is immobilized by suction on a conical hole. The upper part of the oocyte membrane is permeabilized using ionophore such as nystatin. The reduction of the electrical impedance in this permeabilized region provides the electrical access to the inside of the cell. Hence, the standard TEVC measurement method can be performed without the need of inserting microelectrodes inside the oocyte. This method eliminates the problem of delicate electrodes insertion and their stability during measurements but still require the chemical permeabilization of the oocyte membrane. In the context of long term oocyte measurement, the chemical permeabilization of the membrane is to be avoided as it engenders modifications of the cytosol.

Schaffhauser *et al.* (Schaffhauser, 2011) performed another step, where the chemical permeabilization was replaced by a strong asymmetry between the upper and lower membrane patch defined by the shape of its Ussing-like chamber. The large ratio between the two membrane sections was sufficient to sustain the current to be measured in the small patch section without further membrane opening. This principle resembles to the whole-cell patch clamp method (Hamill, 1981). The instrumentation used in his experiment is still the conventional TEVC and four electrodes are required to perform the measurement.

The next step that is proposed in this study is also based on the membrane segmentation but the conventional TEVC method is replaced by an impedance spectroscopy approach. Impedance spectroscopy allows characterizing cell dielectric structure as well as ion transport phenomena (Martinsen, 2011). As impedance spectroscopy use alternative voltage excitation and, provided that the electrodes have a bigger capacitance than the oocytes, it is possible to use only external macro electrodes by avoiding the important microelectrode faradic resistance and the related junction potential. The alternative current that is circulating through the oocyte passes through the electrode capacitance instead of the electrode faradic resistance and consequently removes the need of using silver chloride electrodes. In a similar fashion, the large membrane patch section presents a smaller resistance and a larger capacitance than the small membrane patch section allowing the measurement of the impedance to be dominated by small membrane patch. Based on this hypothesis, the aim of this study consists of determining if ion channels modulation can be

detected using impedance spectroscopy on oocytes. This would provide a simplified instrumentation for long term, miniaturized and integration of biosensors based on electrophysiology measurements.

4.2 Models for non-invasive measurements of electrically active cells

This section evaluates different solutions using impedance spectroscopy as a non-invasive method for cell electrophysiology measurements and detection of ions channels activity in the context of biosensor development.

First, a discrete impedance based model derived from the Hodgkin-Huxley model is proposed. According to this model, different approaches of cell segmentations allowing to access cell internal parameters in absence of intracellular electrodes are discussed.

Second, as impedance spectroscopy allows characterizing the spatial arrangement of conductive and dielectric layers and because ions are rearranged during the process of channel opening or closing, a second model based on the spatiotemporal ion distribution is developed and discussed.

These two models are used to identify physical properties linked to the opening and closing of over-expressed ligand-gated sodium channel in cell allowing to propose and discuss different non-invasive electrophysiology measurements possibilities.

4.2.1 Discrete impedance membrane model

The electrical behavior of electrically active cell membranes has already been widely studied and a model was proposed by Hodgkin-Huxley (Hodgkin, 1952). As shown in Figure 4.1, this model takes into account the resistance of the ion channel, the capacitance associated to the lipid membrane and the equilibrium potential of each ion species depending on their respective concentrations and membrane permeability. This model introduces a discrete electrical equivalent comprising a voltage source, a capacitance and a resistance-like element

as showed in Figure 4.1 b). The resistance-like element is however not linear and has voltage and time dependencies. Using the Goldman-Hodgkin-Katz equation shown in Equation 33, this model allows to evaluate the membrane potential and trans-membrane currents. Based on this electric equivalent model, a discrete impedance equivalent model is proposed where voltage sources are replaced by a short-circuit and current sources by an open circuit according to their definition (Sadiku, 2009). The discrete impedance equivalent model is shown in Figure 4.1 c).

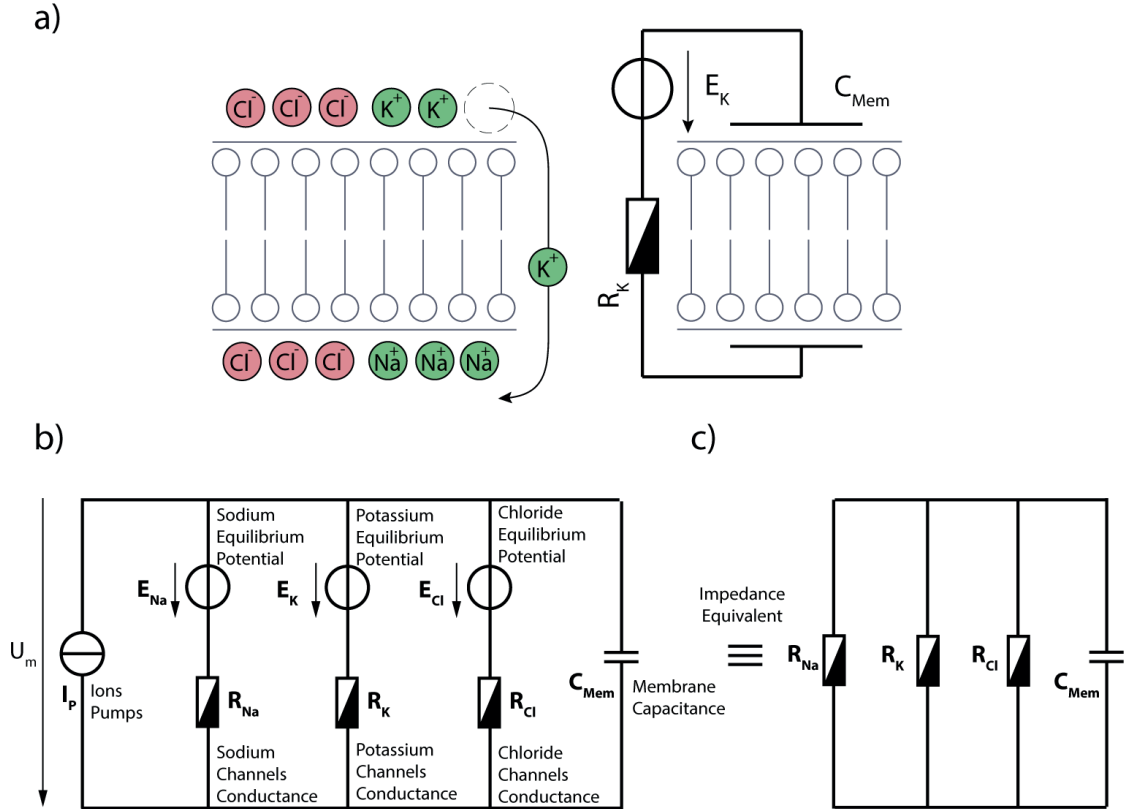


Figure 4.1 : The Hodgkin-Huxley model for cell membranes. a) Specific schematic example for potassium channels b) Electrical equivalent schematic generalized for sodium, potassium and chloride ions. c) Discrete impedance equivalent schematic. Figure adapted from (Hodgkin, 1952).

$$U_m = \frac{RT}{F} \ln \left(\frac{P_{Na^+}[Na^+]_{ext} + P_{K^+}[K^+]_{ext} + P_{Cl^-}[Cl^-]_{ext}}{P_{Na^+}[Na^+]_{int} + P_{K^+}[K^+]_{int} + P_{Cl^-}[Cl^-]_{int}} \right) \quad \text{Equation 33}$$

4.2.2 Cell impedance segmentation to access local membrane parameters

The electrical equivalent model presented in Figure 4.1 describes the voltage and currents of a cell membrane without specifying any membrane geometry and arrangement. A biological cell is a closed volume defining an intracellular and extracellular compartment. Recording the trans-membrane potential or measuring the cell impedance requires either inserting an intracellular electrode inside the cell volume or segmenting the cell membrane with a region where the local membrane resistance is smaller than extracellular resistance separating the different segmented domains of the cell.

This concept is illustrated by different examples showed below. Figure 4.2 a) shows a classical experiments of the recording of the compound action potential in a nerve bundle that we conducted as preliminary trial. It consisted in recording the action potential travelling along nerve axons bundle. Figure 4.2 b) shows the equivalent electric schematic of the axons in addition to the recording electrodes. This schematic illustrates that the local measurement of the action potential U_{Mem2} is provided simply by reading U_2 because the local membrane resistance R_{Mem2} is significantly smaller compared with the leak resistance R_{Leak2} between the different recording electrodes. In this specific experiment, the high leak resistance R_{Leak2} was obtained using a sufficient distance without any conductive media between the recording electrodes.

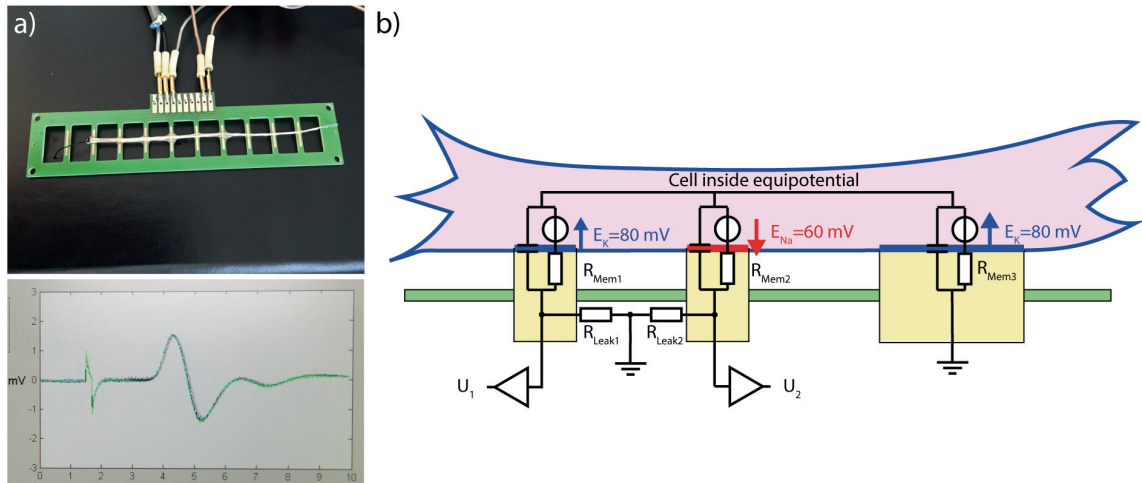


Figure 4.2 : Nerve bundle recording. a) Recording of the compound action potential in a nerve bundle b) Equivalent electric schematic of a nerve axon and recording instrumentation to illustrate the cell segmentation required to record the extracellular activity.

Similarly, Figure 4.3 a) show the equivalent electric schematic of a cell adhering on a microelectrode array (MEA). The action potential of a cell can be recorded from the outside microelectrodes because the sealing resistance R_{Leak} between two adjacent electrodes underneath the cell is large compared to the local membrane resistance. This concept of cell segmentation is well illustrated by the important efforts deployed to increase the leak resistance with different electrodes shape, material and arrangement in MEA (Spira, 2013) as shown in Figure 4.3 b)

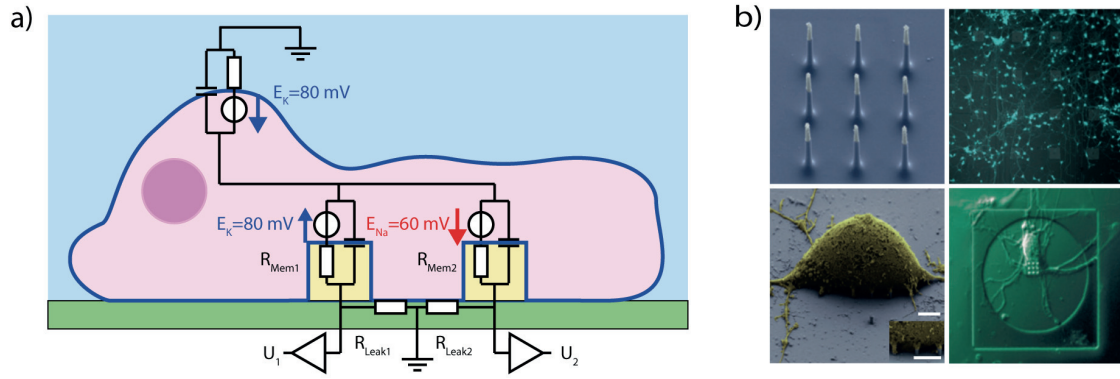


Figure 4.3 : Neuron recording with a MEA. a) Cell action potential recording with a MEA as illustration of cell segmentation with controlled leak resistance to record the cell inside potential. b) Microstructures to increase the leak resistance. Figure adapted from (Spira, 2013).

Another interesting example of cell segmentation is the Torpedo electrocyte shown in Figure 4.4 from (Tanaka, 2016). With different ion channel activated on each cell side of the cell, the membrane exhibits a different voltage on each side of the cell. Because those cells have an important surface compared to their thickness, the current leak path between the two cell sides represent an important resistance and allows to sustain a net voltage between each cell side.

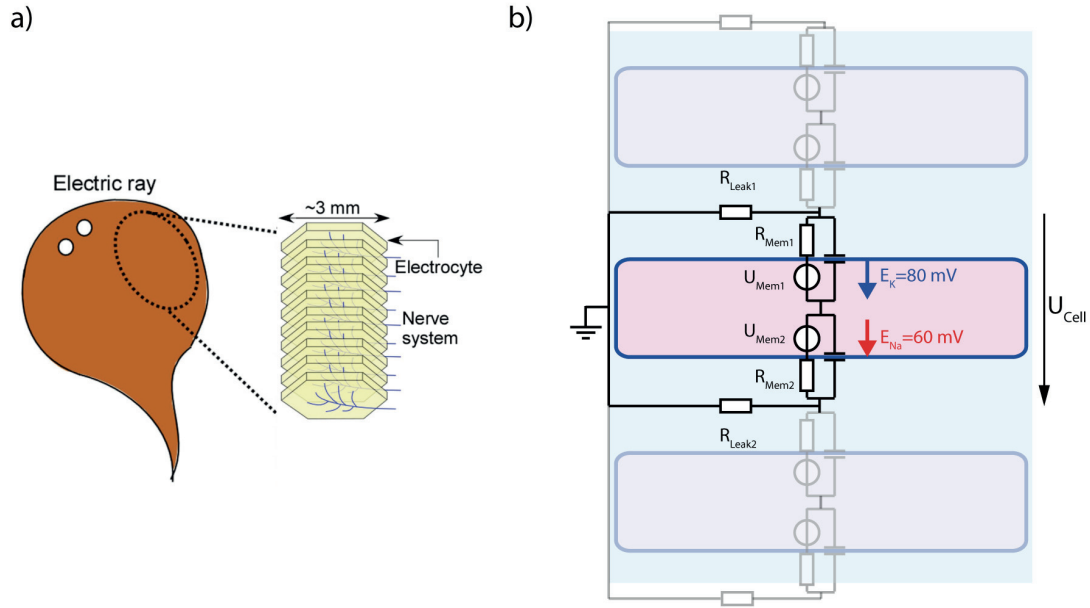


Figure 4.4 : Torpedo electrocyte exhibiting a trans-cell voltage. These electrocytes are another example of cell segmentation with increased leak resistance due to their aspect ratio allowing to sustain a total trans-cell voltage. Figure adapted from (Tanaka, 2016).

From the examples described above, a generic electric equivalent for a cell segmented into two different compartments is proposed in Figure 4.5 a). It comprises a voltage potential U_{Mem} , a membrane resistance R_{Mem} and a membrane capacitance C_{Mem} for each segment of the membrane as well as a leak resistance R_{Leak} linking the two compartments defined by the cell segmentation. This model is applicable to any cell and allows calculating the cell inside voltage and the membrane current depending on the external potential applied on each compartment as well as their ion concentration according to the Hodgkin-Huxley model. If the cell segmentation provides an upper membrane resistance R_{Mem1} far smaller than the lower membrane resistance R_{Mem2} and if the leak resistance R_{Leak} is sufficiently large, then the cell inside potential is defined by the potential of the upper compartment U_2 . Reciprocally, the cell inside potential can be obtained measuring the upper compartment voltage U_2 . This measurement scenario can typically be achieved with a strong membrane area asymmetry as demonstrated by (Schaffhauser, 2011) and in a more general fashion with the cell attached patch-clamp (Hamill, 1981). From an impedance perspective, this discrete electrical model derives to the impedance equivalent schematic proposed in Figure 4.5 b). Assuming a strong asymmetry between the upper and lower cell segmentation as well as a

sufficiently important leak resistance R_{Leak} , the total impedance is dominated by the lower membrane section impedance defined by R_{Mem1} and its respective capacitance C_{Mem1} .

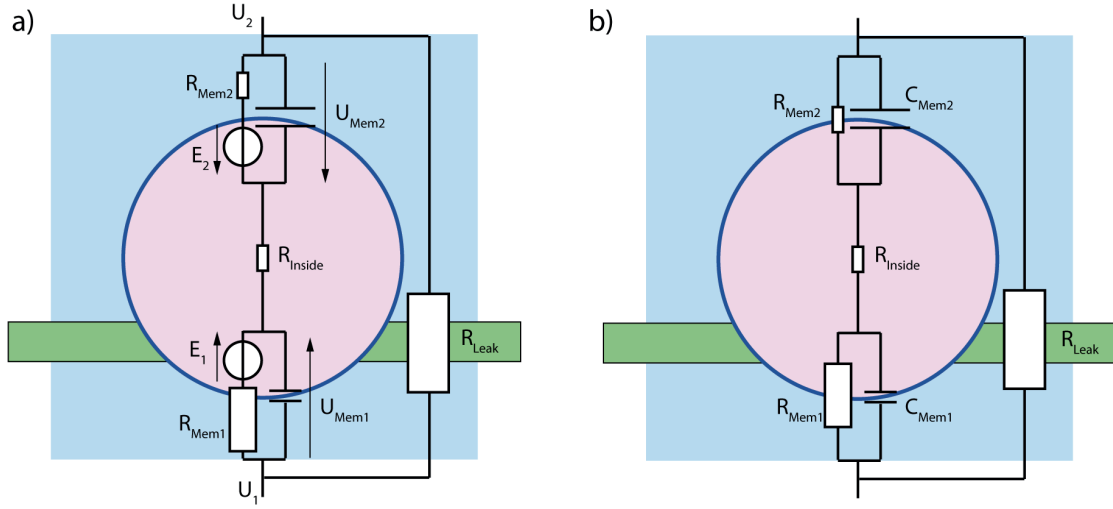


Figure 4.5 : Generalized cell segmentation concept. a) Discrete electric equivalent schematic and b) discrete impedance equivalent schematic for a segmented cell.

4.2.3 Spatiotemporal ion distribution model for electrically active cells

Unlike resistance characterization by continuous voltage application and current monitoring, impedance spectroscopy consists of applying an alternative voltage excitation covering a range of frequencies. This allows characterizing the spatial arrangement of conductive and dielectric layers that are linked to ions transport and re-arrangement as exploited in semiconductor or electrochemical structures analysis such as dye solar cells (Kern, 2002; Wang, 2005). In the context of cell membranes, some ion species are crossing the membrane to induce a potential difference and as consequence the ion distribution has to vary locally to induce a potential change as illustrated in Figure 4.6. To evaluate these local variations and determine if they can be realistically measured using impedance spectroscopy, we propose a second model as an extension of the discrete circuit-like Hodgkin-Huxley model to evaluate spatial distribution of ions, charges, electric field and potential along the cell structure including the channels permeability modulation in time.

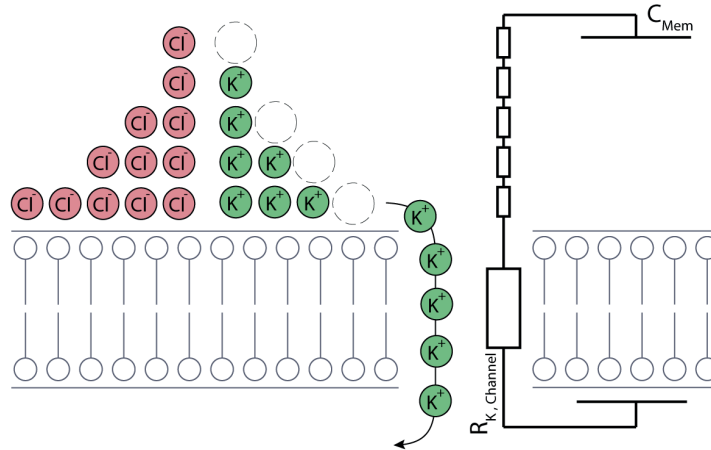


Figure 4.6 : Ions distribution around the cell membrane. Illustration of local variation of potassium ion concentration around the membrane induced by their displacement through a channel inducing the membrane equilibrium potential.

4.2.3.1 Model & assumptions

This analysis consists of a one-dimension radial symmetric model of the cell as shown in Figure 4.7 a) & b). This model describes the ions concentration, charge, electric field as well as potential along the cell structure. To simplify the model and the subsequent analysis, the simple scenario of a cell presenting ligand-gated sodium channels whose permeability can be controlled in addition to natural leaky potassium channel is proposed. Two different cases are studied. Closed sodium ligand-gated channels and open potassium leak channels define the first case. The second case is defined by both the sodium ligand-gated channels and the potassium leaky channels in the open state.

In this model, only highly abundant ions being sodium, potassium and chloride are considered. Cell inside is usually also composed of non-permeant charged protein that balance the total charge to respect the global electroneutrality of the cell. In this specific resolution and as neither chloride ions nor the non-permeant charged proteins are allowed to cross the membrane, they are both accounted as chloride ions with same valency.

Both the cytosolic and membrane parts of the cell are represented by an infinitesimal element defined by the local ion concentration of each species, their mobility as well as the effective cross section allowing the displacement of each different ions family in the respective element and as illustrated in Figure 4.7 c). For the membrane elements, the cross section parameter is tuned for each ion family according to the membrane channel state and

its respective ionic permeability. In cytosol element, the effective cross section has always a unity value meaning ions can travel freely according to their respective mobility.

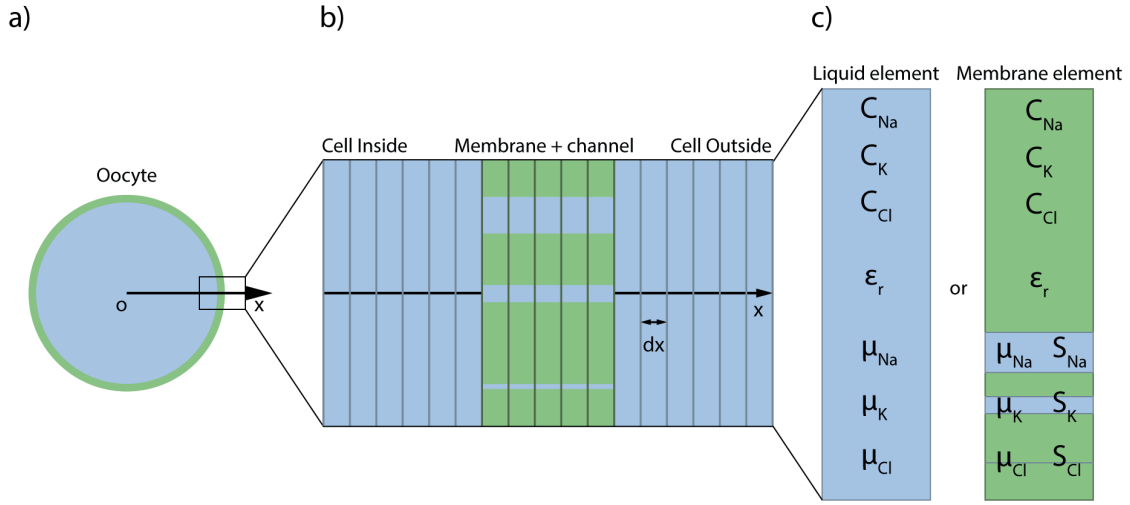


Figure 4.7 : Construction of the spatiotemporal ion distribution model. a) One-dimension radial symmetric model with axis origine at the cell center. b) Infinitesimal elements constituting the cell interior, exterior and the membrane. c) Definition of the infinitesimal element with the ions concentration, ion mobility, ion channel effective cross-section and relative permittivity.

As the model is monodimensional, the total ion displacement is accounted as an average for the full membrane section even though the reality is that each family of ions are effectively travelling through an other family of channel. It is assumed that the time for ions to move between the channels is faster than the time to move across the channel resulting in a homogeneous ion concentration inside a finite element. In this model, it is assumed that the inside and outside cell media has globally the same total osmotic concentration. Moreover, it is assumed that aquaporine leave water molecule crossing freely the membrane (Agre, 1993) thus no hydraulic pressure differences are taken in account.

Forces acting on ions are primarily electrical and diffusion forces due to electrical potential and ion concentration gradient in the structure. The total ion current density $J_i(x)$ resulting of both the diffusion and electrical drift acting on every ion accordingly to Nernst-Planck Equation (Johnston, 1995) is presented in Equation 34 and illustrated in Figure 4.8.

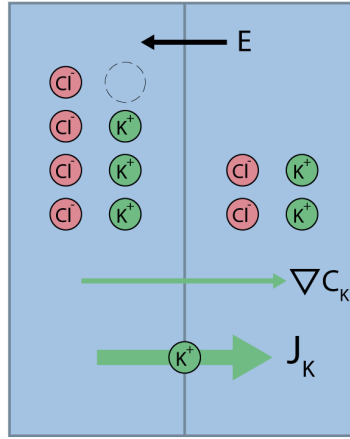


Figure 4.8 : Ion current between elements. Considering the Nernst-Planck equation, the total ion current between elements results from the ions diffusion and electrical drift.

$$J_i(x) = |z_i|q\mu_i C_i(x)E(x) - \frac{z_i}{|z_i|}kT\mu_i \frac{\partial C_i(x)}{\partial x} \quad i \in \{Na, K, Cl\} \quad \text{Equation 34}$$

Under those assumptions, the problem becomes very close to the description of charges carriers behavior that are dominated by drift and diffusion forces in physics of semiconductor (Sze, 2006) and similar model used for electrostatic analysis of ion channel (Chen, 1997) (Eisenberg, 1998). However, there is some specificity of this biologic model compared with a semiconductor model. First, there are three different charge carriers being the Na, K, Cl ions. Second, in this model, all the carriers are mobiles and no space charges due to doping are considered. Finally, no ions generation or recombination is considered in the structure and the ion exchange due to the sodium potassium pump (ATPase) is also neglected.

For each time step N , the following system is evaluated with state variables being the three different concentrations $C_i(x)$ of each different ions (Na, K, Cl) defined at every place in the structure (Equation 35). The number of ions per cubic meter defines those concentrations. The charge $Q(x)$ is then calculated in the structure by summing every different ions, taking in account their respective valence Z_i and the elementary charge q as shown in (Equation 36)

The electric field $E(x)$ is evaluated in every point of the structure using Gauss theorem integrating the amount of charges $C_i(x)$ (Equation 37). The electric potential $\phi(x)$ is

evaluated as the primitive integral of the electric field $E(x)$ (Equation 38). The current density is evaluated taking in account both the diffusion and electrical drift forces respectively influenced by the ion concentration and electrical field (Equation 39). Finally, for each time step, the concentration of ions at each position of the structure $C_{i_{N+1}}(x)$ is recalculated using the continuity equation (Equation 40) without any generation or recombination considered but only ions movement. Along the time steps, different conditions on channel opening and closing are taken in account with the variation of each channel cross section $S_{eff_i}(x)$. Physical values used for the different model parameters are listed in Table 1 where the different physiological constants such as ions concentration are adapted from (Weber, 1999).

$$C_i(x) \quad i \in \{Na, K, Cl\} \quad [1/m^3] \quad \text{Equation 35}$$

$$Q(x) = q \sum_i Z_i C_i(x) \quad [C/m^3] \quad \text{Equation 36}$$

$$E(x) = \int \frac{Q(x)}{\epsilon_0 \epsilon_r} dx \quad [V/m] \quad \text{Equation 37}$$

$$\varphi(x) = - \int E(x) dx \quad [V] \quad \text{Equation 38}$$

$$J_i(x) = S_{eff_i}(x) \left(|z_i| q \mu_i C_i(x) E(x) - \frac{z_i}{|z_i|} kT \mu_i \frac{\partial C_i(x)}{\partial x} \right) \quad [A/m^2] \quad \text{Equation 39}$$

$$C_{i_{N+1}}(x) = C_{i_N} - \frac{1}{z_i q} \frac{\partial J_i(x)}{\partial x} \Delta t \quad [1/m^3] \quad \text{Equation 40}$$

Table 4.1 : Parameters selected for the spatiotemporal ion distribution model

Membrane thickness	t	10 nm
Sodium initial concentration inside cell	$C_{Na,IN}$	10 mM
Sodium initial concentration outside cell	$C_{Na,OUT}$	90 mM
Sodium initial membrane concentration	$C_{Na,MEM}$	0 mM
Sodium valency	Z_{Na}	+1
Sodium mobility	μ_{Na}	$4.98 \times 10^{-8} \text{ m}^2/\text{Vs}$
Potassium initial concentration inside cell	$C_{K,IN}$	90 mM
Potassium initial concentration outside cell	$C_{K,OUT}$	10 mM
Potassium initial membrane concentration	$C_{K,MEM}$	0 mM
Potassium valency	Z_K	+1
Potassium mobility	μ_K	$10.12 \times 10^{-8} \text{ m}^2/\text{Vs}$
Chloride initial concentration inside cell	$C_{Cl,IN}$	100 mM
Chloride initial concentration outside cell	$C_{Cl,OUT}$	100 mM
Chloride initial membrane concentration	$C_{Cl,MEM}$	0 mM
Chloride valency	Z_{Cl}	-1
Chloride mobility	μ_{Cl}	$6.88 \times 10^{-8} \text{ m}^2/\text{Vs}$
Potassium channel cross section (leaks)	S_{eff_K}	1/10
Sodium channel cross section (closed)	$S_{eff_{Na,C}}$	0
Sodium channel cross section (open)	$S_{eff_{Na,O}}$	1/2
Absolute permittivity	ϵ_0	$8.85 \times 10^{-12} \text{ F/m}$
Relative permittivity	ϵ_r	5
Elementary charge	q	$1.602 \times 10^{-19} \text{ C}$
Boltzmann constant	k	$1.38 \times 10^{-23} \text{ J/K}$
Temperature	T	300 K

4.2.3.2 Numerical solving

The set of equation presented above is numerically solved using a Matlab (R2016a, Mathworks, US) script shown in appendix (§7.3). The resolution consists of a loop running over the time steps N and taking in account the changes of the different ions channel permeability by modulating the different channel cross section S_{eff_i} .

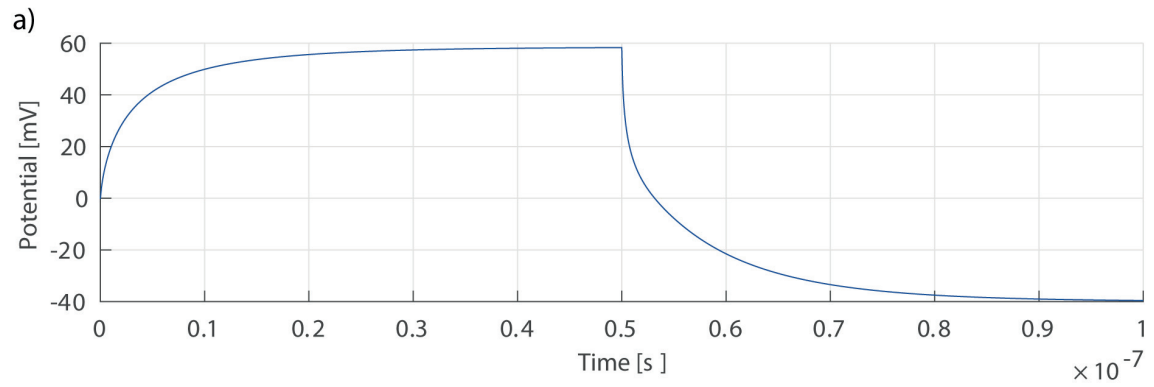
For each iteration, the charge, electrical field and potential are evaluated along the cell structure based on the actual ion concentration. Based on those values, the ion flux is

calculated and continuity equation is used to redistribute ion accordingly in the structure. Considering the important amount of iterations and in order to accelerate the solving, native Matlab vectors and the corresponding vectorial functions such as gradient or cumulative sum are used.

The spatial structure is defined with the origin at the center of the cell. Boundary conditions are set with zero electric field and potential at the center of the cell as it is convenient for numerical solving to use vectors with initial value set by boundary condition. For this reason, all the voltage expressions have an opposite sign to the electrophysiology convention that places the ground at the exterior of the cell. The hypothesis of a zero electric field at the center of the cell is only valid if no current is flowing at the center of the cell. This hypothesis is verified if the system is not placed outside of equilibrium by the application of an external potential on the cell and if the total lengths of the evaluated structure is far bigger than the actual membrane thickness. For this reason, the system was evaluated on a total length 25 times bigger than the actual 10 nm membrane thickness.

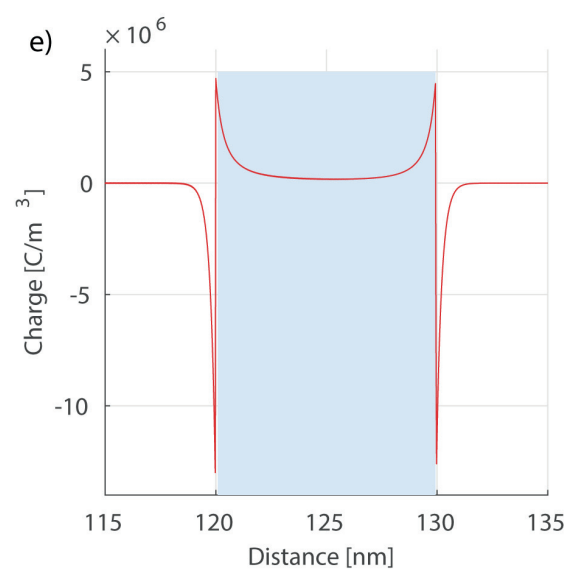
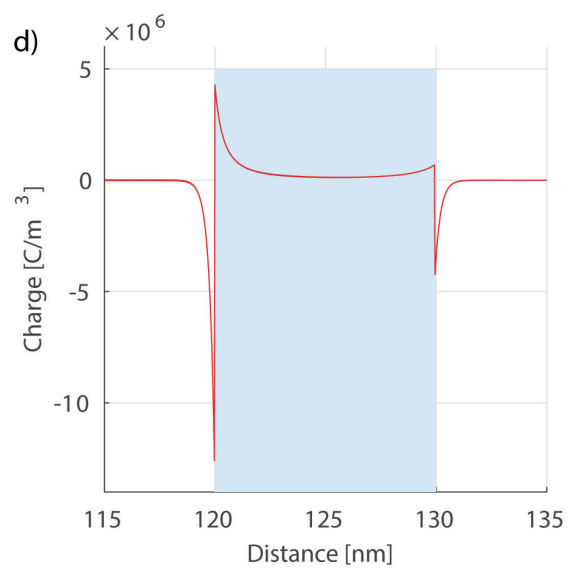
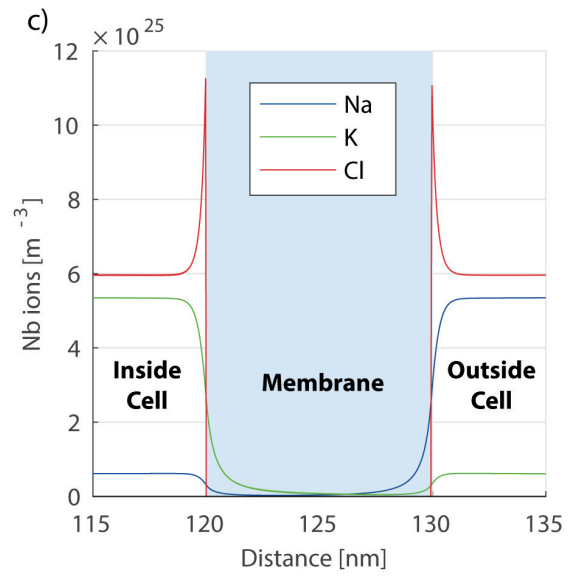
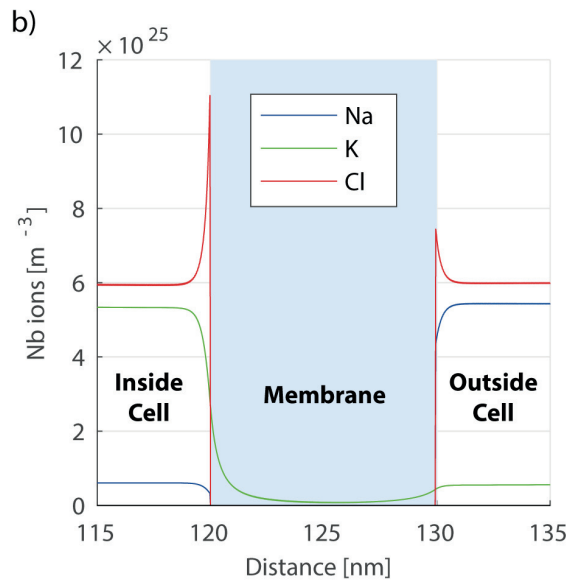
In order to achieve a stable resolution, both dx and dt were chosen empirically with respective values of $dx = 0.25 \text{ \AA}$ and $dt = 0.3 \text{ ps}$ over a total structure length of 250 nm and a simulation time of 100 ns.

4.2.3.3 Resolutions



Ligand-gated sodium channel closed

Ligand-gated sodium channel open



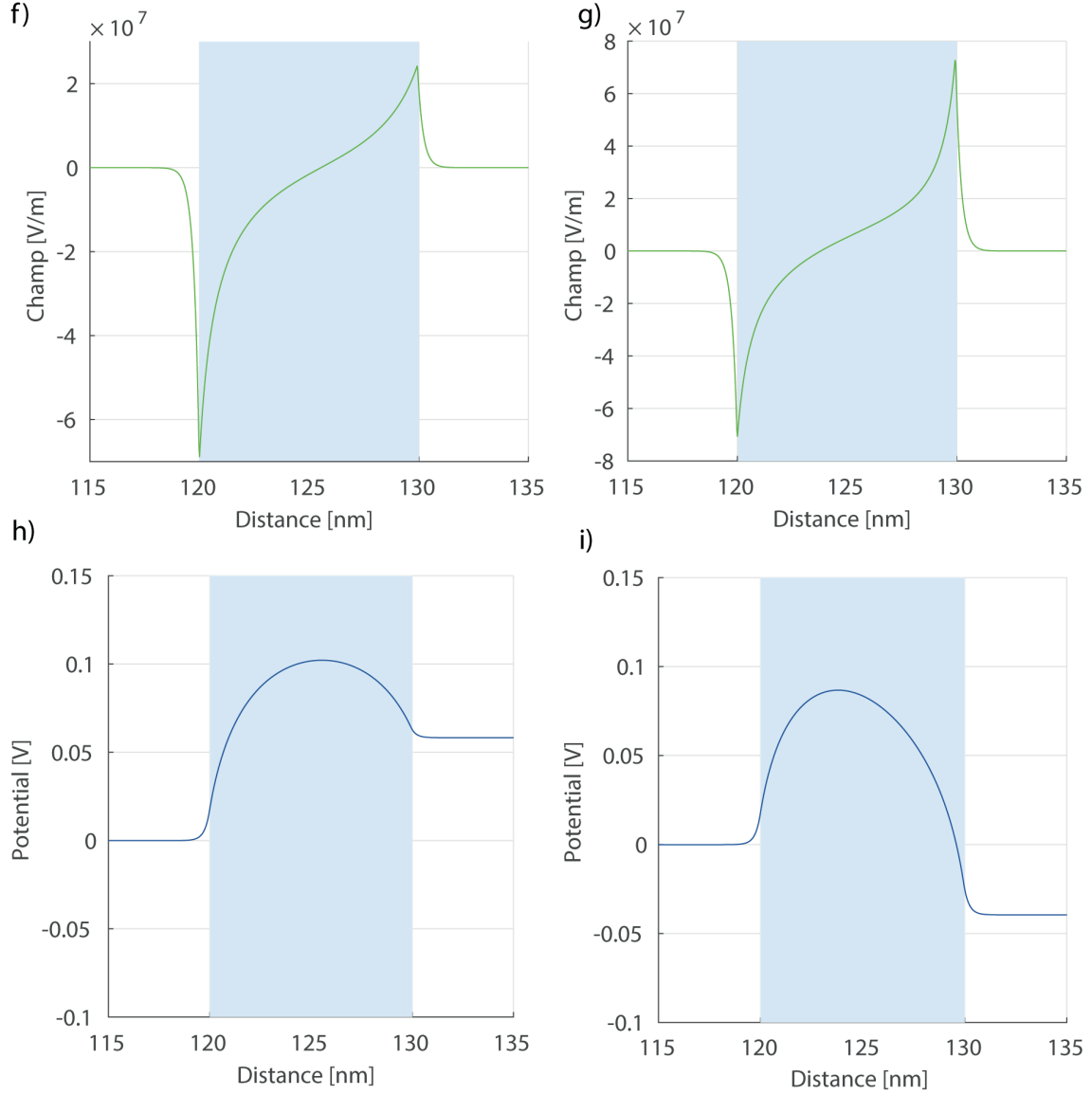


Figure 4.9 : Resolutions of the spatiotemporal ion distribution model. a) Potential across the cell structure varying with time before and after sodium channels opening. b) & c) ions concentration, d) & e) net charge, f) & g) electric field and h) & i) potential along the cell structure before and after the sodium channels opening.

Using the spatiotemporal ion distribution model described above, the electric potential between the inside and outside of the cell is evaluated for the open and close states of ligand-gated sodium channels in addition to the always-open potassium leak channel. Figure 4.9 a) shows the two quasi steady-state voltages obtained with the model. The first quasi-steady state obtained after 50 ns with a value of $-(-58\text{mV})$ represents the resting state of the cell where only the potassium leak channels are open. The second steady state obtained after 100 ns with a value of $-(+40\text{mV})$ represents the case where ligand-gated

sodium channel are open in addition to the potassium leak. Those trans-membrane electric potential results are in agreement with the Goldman-Hodgkin-Katz voltage equation for those conditions of membrane permeability and ion concentration. The sign is opposed to the biological convention as the zero potential was set at the center of the cell to facilitate the numerical solving to the contrary of the biological convention that places the zero potential outside the cell.

4.2.3.4 Ions concentration

Figure 4.9 b) shows the ions concentration for potassium, sodium and chloride around the cell membrane starting from the inside of the cell toward the outside of the cell when potassium leaks channels are open and overexpressed sodium channel are closed. Figure 4.9 c) shows the concentration of the same ions in the case of both potassium leak and overexpressed sodium ion channels open.

For both cases of channel state shown in Figure 4.9 b) & c) the concentration of Na, K, Cl ions are respectively 10 mM, 90 mM, 100 mM at the far left of the curves representing the inside of the cell as imposed as initial condition in the model. Similarly the far right of the curve representing the outside of the cell has the same concentration than the one set as initial condition of 90 mM, 10 mM, 100 mM for Na, K, Cl respectively. This shows that the global concentration everywhere away from the membrane is unchanged whatever is the state of ion channel. Within a range of 1 nm around the membrane, ions are rearranged because of the different permeability of ions channel. In the situation where only potassium leak channel are open as shown in Figure 4.9 b) on the left side of the membrane, potassium ions diffuse through the membrane leaving negatively charged chloride. This charge imbalance creates an electric field that retains potassium ion to diffuse further away and accumulate more chloride toward the membrane. In this case, sodium ions are pushed away from the membrane by the electrical field created by the charge imbalance. On the right side of the membrane, a similar effect is happening with a diffusion of potassium into the membrane, the accumulation of chloride and depletion of sodium.

Figure 4.9 c) shows the case of open ligand-gated sodium channels. This case leave the left side of the membrane almost unchanged in term of ion concentration. On the right side of the membrane, because of the opening of sodium channel, sodium diffuses into the membrane and thus leaves more unbalanced chloride that strengthens the electric field and accumulates further chloride at the membrane. Between those two cases, a chloride increase

from $7.5 \times 10^{25} \text{ m}^{-3}$ to $11 \times 10^{25} \text{ m}^{-3}$ representing a concentration change from 120 mM to 160 mM is observed in a confinement smaller than 1 nm at the right side of the membrane.

It can be concluded that those two different cases does not induce a significant variation in the amount of ions in the overall cell structure although some important differences notably on the chloride concentration are observed in a 1 nm region around the membrane due to the opening of sodium channel.

4.2.3.5 Charge & electric field at the membrane

Consecutively to the ion rearrangement described in the previous section, Figure 4.9 d) & e) shows the net charge as being the sum of all different ions taking in account their sign and valency across the cell membrane. The cell structure starts from the inside of the cell toward the outside of the cell and the two cases of ligand-gated sodium channels open and closed are presented.

The opening of sodium channel does not significantly changes the amount of charges on the cell internal side of the membrane. But on the cell external side of the membrane, positive charges accumulated on the left side of the membrane-cell interface increase from 0.3 C/m^3 to 4.5 C/m^3 and negative charges accumulated on the right side of the membrane-cell interface decrease from -4 C/m^3 to -12.5 C/m^3 .

Figure 4.9 f) et g) shows the corresponding electric field across the cell membrane. On the cell internal side of the membrane, the electric field is not significantly changed by the channel modulation with a constant value of $-7 \times 10^7 \text{ V/m}$. On the right side of the membrane, the electric field increases from $2.5 \times 10^7 \text{ V/m}$ to $7 \times 10^7 \text{ V/m}$ when overexpressed ion channels are open.

4.2.3.6 Trans-membrane potential

The local ions rearrangement leads to a change of charges, electric field and finally electrical potential across the membrane. Figure 4.9 h) shows the electric potential along the cell structure starting from the inside of the cell toward the outside of the cell when potassium leaks channel are open and ligand-gated sodium channel are closed. According to this curve, a potential difference of $-(-58 \text{ mV})$ is observed across the membrane. Figure 4.9 i) shows the same electric potential curve in the case of both potassium leak and liagand-gated sodium ion channels open. According to this curve, a potential difference of $-(-40 \text{ mV})$ is observed

across the membrane. Both curves show a potential variation comprised in the region of the membrane extended by a few nanometer on each side. Once this extension region is passed, the potential does not change anymore in all the cell structure.

4.2.4 Non-invasive measurements of ion channel permeability

The different physical quantities variations observed in the resolution above are discussed as potential measurement method to detect ion channel permeability modulation. A special emphasis is placed on physical quantity that can be measured by impedance spectroscopy as a non-invasive measurement technique.

4.2.4.1 Trans-membrane potential measurements

Considering Figure 4.9 a) & b), the trans-membrane voltage varies from $-(-58\text{mV})$ to $-(40\text{mV})$ consecutively to the ligand-gated sodium channels opening. Those results are in agreement with the discrete electrical equivalent Hodgkin-Huxley model as well as the Goldman-Hodgkin-Katz equation and represents a 98mV voltage swing. As anticipated, the trans-membrane potential variation is a very efficient way to observe the ion channel modulation. Moreover the electric potential has a steady spatial value in all the cell structure except in a small region extending a few nanometers around the membrane. This allows performing potential measurements with little constraints on electrodes placement. However, because of the need of the cell internal potential value, this method is either invasive with the insertion of an intracellular electrode or the cell as to be segmented to record the internal potential with an external electrode as detailed in the previous section (§4.2.2).

4.2.4.2 Charge & electrical field measurements

According to Figure 4.9 d) to g), the sodium channel modulation also affect the net charge accumulated at the cell external side of the membrane and its corresponding electrical field. Even though, this effect is very localized at the membrane proximity, it can be used for ion channel permeability modulation as illustrated in different works introducing the concept of BioFET derived from the ISFET structure based on potentiometric detection of charge density change (Sakata, 2008; Schaffhauser, 2012). This method is by nature non-invasive as the whole cell is put into contact with a semiconductor structure and no electrodes have to be placed inside the cell.

4.2.4.3 Impedance measurements

Two effects induce a cell conductivity change that is translated into an impedance variation. The first effect is the modulation of the membrane ion channels permeability *per se* as described by the discrete electric equivalent Hodgkin-Huxley model as shown in Figure 4.1 c). As ion channels are the main restriction for ion transport, they significantly affect the membrane conductivity. This effect is anticipated to be measurable by impedance spectroscopy.

The second effect is linked to the distribution of ions in the structure. Assuming that the number of carriers multiplied by their charge and mobility gives the conductivity in a conductive material, the ion redistribution at the proximity of the oocyte membrane will modulate the conductivity. As depicted in Figure 4.9 b) & c), the chloride ion concentration is effectively varying from 120 mM to 160 mM at the right side of the membrane. However, this ion redistribution affects only a region extending 1 nm away from the membrane. We anticipate a conductivity increase in the 1 nm slice around the cell because of the chloride accumulation despite a smaller sodium depletion. Observing this localized effect using impedance spectroscopy would require to use a very specific electrode arrangement allowing conductivity measurement of a volume not significantly extending the 1 nm slice around the cell. A possibility to observe this effect could be the use of nanoelectrodes.

However, for impedance spectroscopy measurements on a whole cell, the first effect directly related to the ion channel resistance modulation is predominant. This suggests that whole cell impedance measurement is comprehensively described by the discrete impedance model derived from the Hodgkin-Huxley model presented in Figure 4.5 b).

4.3 Impedance spectroscopy on *Xenopus laevis* oocytes for ion channel modulation investigations

The section presents the experimental work performed on *Xenopus laevis* oocytes for monitoring ligand-gated ion channels activity using impedance spectroscopy as a label free, non-invasive and real-time method.

4.3.1 Material & methods

4.3.1.1 *Xenopus laevis* oocytes

Xenopus laevis oocytes are used as cellular model in this study because of their large size allowing easy handling as well as their ability expressing a wide panel of membrane proteins directly from RNA injection. This make *Xenopus laevis* oocyte a gold standard cellular model for ion channel protein expression (Gudron, 1971; Miledi, 1982; Sumikawa, 1982; Dascal, 1987; Weber, 1999).

Oocytes were surgically removed from the ovarian tissue of female *Xenopus laevis* african clawed frog, which had been anesthetized by immersion in MS-222 (Bargeton, 2010). Oocytes from different stages of maturity are extracted from the ovary and placed in modified Barth's solution (MBS). Mature oocytes of stage V and VI are large cells of a diameter around 1.2 mm (Sherman-Gold, 1993). Oocytes are manually sorted according to their stage suiting electrophysiology measurements and presenting a good visual aspect attesting of their viability and quality.

Oocytes consist of a multi layer and membranes structure as illustrated in Figure 4.10. The oocytes cellular membrane embedding ion channels is surrounded by a 10 μm vitelline membrane made of fibrous glycoprotein allowing this large cell to keep its mechanical stiffness and integrity. The vitelline membrane has a gel-like porous structure largely permeable to ions. A follicular layer coupling oocytes together surrounds the vitelline membrane. A collagenase treatment is used to strip off the follicular layer. It consists of immersing the oocyte for 60 min to 70 min in a calcium-free saline solution containing 2 mg/mL of collagenase and 1 mg/mL of bovine serum albumin at room temperature (Sherman-Gold, 1993).

4.3.1.2 Injection & preparation

Epithelial Sodium Channels (ENaC) are ion channels involved in the sodium balance maintenance of mammals (Rossier, 2014). These channels were selected for this study. First, because of their high permeability to sodium ions whose concentration can be easily adapted in solutions. Second, as ENaC is a ligand-gated ion channel, it allows modifying its permeability by exposing the ligand-gating domain to amiloride, a channel blocker and drug used to treat high blood pressure (Canessa, 1994). Third, ENaC presents a bi-stable behavior with a natural high permeability steady state and low permeability steady state when amiloride bind to the ligand-domain. This allows to monitor a slow kinetic only controlled by the perfusion and thus removing the high bandwidth constraints on the instrumentation. CRNAs constructs from DPT, UNIL of rENaC and hENaC were used in this study. 100 nL of solution at 10, 50 or 100 ng/ μ L were directly injected into the oocytes cytosol using the RobotInject (MultiChannelSystem). ENaC injected oocytes were then incubated at 19° for 24 hours in a modified MBS (low Na⁺ MBS) containing only 10mM of sodium balanced with 80mM of NMDG, an impermeant ions, because of the high sodium permeability of ENaC expressing cells. Oocytes were stored at 19° in MBS or Low Na⁺ MBS for ENaC injected oocytes between their preparation and the experiments. Normal Frog Ringer (NFR, Ecocyte, US) as well as NFR containing 200 μ M amiloride (Sigmaaldrich, US) were used for the recordings performed in this study. During this work, frog surgery, oocytes preparation and automated injection were performed by my colleague Dr. Benoîte Bargeton, CIG, UNIL according to the Swiss Federal Laws on Animal Protection.

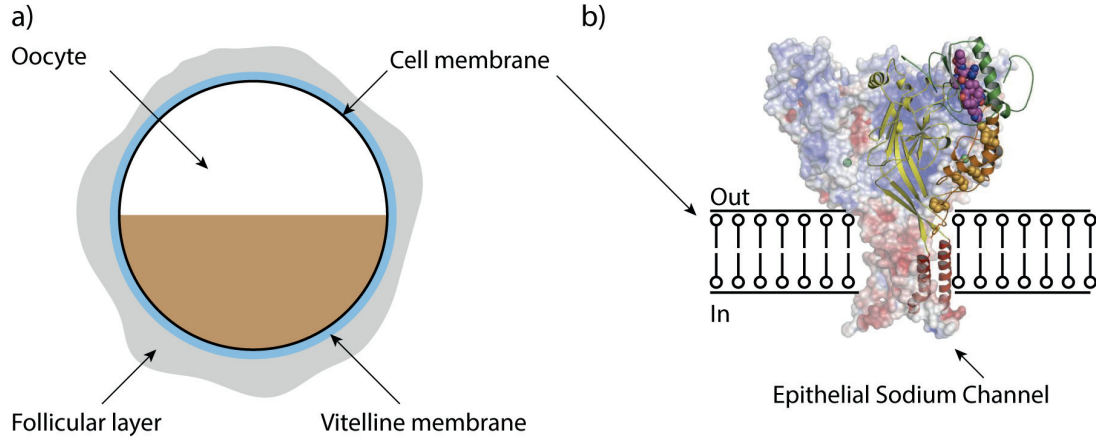


Figure 4.10 : *Xenopus laevis* oocyte structure a) Illustration of stage 5 and 6 *Xenopus laevis* oocytes. Oocytes are composed of a dark animal pole and a light vegetal pole shown in brown and white in the sketch. Oocytes contain a cell membrane surrounded by a vitelline membrane and a follicular layer. b) Illustration of Epithelial Sodium Channel (ENaC) inserted in the oocyte cell membrane adapted from (Kashlan, 2011)

4.3.2 Setup design and model

4.3.2.1 Transoocyte chamber design & fabrication

The concept of non-invasive impedance spectroscopy measurements on *Xenopus Laevis* oocytes is based on the cell membrane segmentation introduced in the previous section (§4.2.2). Figure 4.11 describes the transoocyte chamber designed for the oocyte impedance spectra measurements. The setup is designed to expose asymmetrically the upper and lower membrane sections of the oocyte allowing asymmetric impedance based oocytes measurements.

Figure 4.11 a) shows the transoocyte chamber consisting of 3D printed plastic frame supporting the upper and lower silver electrodes (200 μm silver wire, Advent, UK) disposed on each sides of the oocyte, a liquid reservoir to apply an hydrostatic pressure on the oocyte and a glass pipette to hold the oocyte with the asymmetric exposition of its two membrane sections. The glass pipette is ordered with an external diameter of 4 mm, an internal diameter of 3 mm and a pulled tip with internal diameter of 200 μm (Hilgenberg, DE). The tip of the glass pipette is then polished (PM2, Logitech Ltd, UK) with sandpaper P600, at speed 1 and with 5.33 g of additional weight for 19 min. Figure 4.11 c) shows the side view of the tailor-made glass pipette containing an oocyte and illustrates the asymmetric section of the upper and lower membrane patches. Figure 4.11 d) shows the lower membrane

section of an oocyte in the glass pipette. Using this setup, the glass pipette containing the oocyte can be immersed into different solutions to expose the lower membrane patch to chemical compounds and its corresponding impedance can be measured. According to Figure 4.11 d) the lower membrane patch has a diameter of 400 μm defining a surface ~ 20 time smaller than the total oocyte surface.

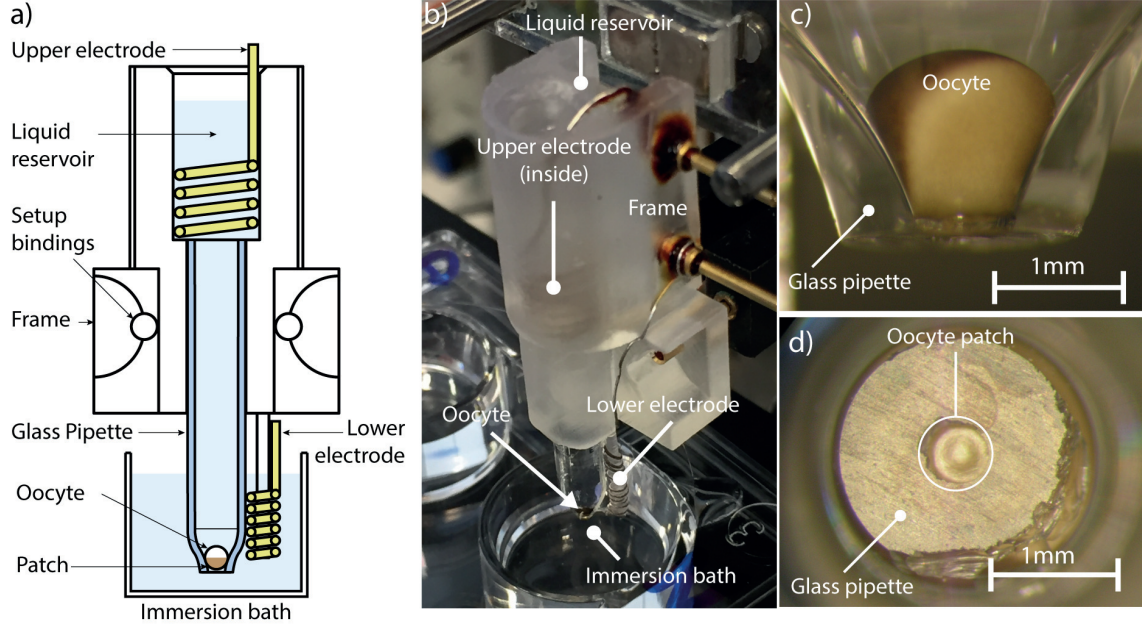


Figure 4.11 : Transoocyte chamber for asymmetric impedance measurements on *Xenopus laevis* oocytes. a) Sketch of the transoocyte chamber consisting of a plastic frame supporting the upper and lower electrodes together with a glass pipette. b) Picture of the transoocyte chamber. c) & d) Magnification of the glass pipette tip containing an oocyte.

4.3.2.2 Electrical equivalent model of an oocyte in the transoocyte chamber

Figure 4.12 a) presents the electric equivalent model of an oocyte placed in the transoocyte chamber according to the principle introduced in the section (§4.2.2).

It comprises the upper and lower electrodes capacitances combined together in serie $C_{Electrodes}$ calculated for two silver wire electrodes of length $l_{electrode} = 7.5 \text{ mm}$ and diameter $d_{electrode} = 200 \mu\text{m}$. Dielectric properties of the NFR are assumed to be similar than water with an absolute permittivity of $8.85 \times 10^{-12} \text{ F/m}$, a relative permittivity of 12.4 and an outer helmoltz plane distance d_{OHP} of 0.5 \AA (Meissner, 2012).

The oocyte membrane is splitted in the upper and the lower membrane patches. The upper membrane patch is much larger than the lower membrane patch and approximated by the total oocyte membrane surface.

The upper membrane patch capacitance $C_{Upper\ membrane}$ is approximated by the total oocyte capacitance $C_{Total,Oocyte}$ of 200 nF (Bernhard, 2002).

The upper membrane patch resistance $R_{Upper\ membrane}$ is approximated by the total oocyte resistance $R_{Total,Oocyte}$ and defined by the membrane ion channel permeability. Specifically for oocytes overexpressing ENaC, values adapted from TEVC literature gives a total current of 2 μ A under a potential membrane difference of 50mV defining a total oocyte resistance $R_{Total,Oocyte} = 25\ k\Omega$ (Dahan, 2007; Dahan, 2008).

According to the asymmetry proposed, the lower membrane patch has a radius comprised between 350 μ m and 450 μ m depending on the oocyte size and consequently a surface 20 times smaller than the total oocyte surface.

The lower patch membrane capacitance $C_{Lower\ membrane}$ is defined twenty times smaller than the upper patch membrane capacitance $C_{Upper\ membrane}$. Providing a homogenous distribution of the protein of interest, the ion channel resistance $R_{Lower\ membrane}$ is selected 20 times bigger than the upper patch membrane resistance $R_{Upper\ membrane}$.

Finally, the resistance R_{Leak} represents the leak around the oocyte, which account for the seal resistance and the resistance of the liquid layer in and below the vitelline membrane. The resistance of the oocyte inside is represented by R_{Inside} and the glass pipette stray capacitance is represented by C_{Stray} . These last three values are empirically chosen. All the different values and respective calculation are summarized in Table 4.2.

Table 4.2 : Selected values for the transoocyte chamber impedance model

$S_{Ratio} =$	$S_{Totale}/S_{Lower\ patch} =$	20	Defined by setup
$C_{Electrodes} =$	$\frac{1}{2} \frac{\epsilon_0 \epsilon_r \pi d_{electrode} l_{electrode}}{d_{OHP}}$	500 nF	Calculated
$R_{Upper\ membrane} =$	$R_{Total,Oocyte} =$	25 k Ω	(Dahan, 2007, 2008)
$C_{Upper\ membrane} =$	$C_{Total,Oocyte}$	200 nF	(Bernhard, 2002)
$R_{Inside} =$		20 k Ω	Experimental
$R_{Lower\ membrane} =$	$R_{Lower\ membrane} = S_{ratio} \cdot R_{Upper\ membrane} =$	500 k Ω	Calculated
$C_{Lower\ membrane} =$	$C_{Lower\ membrane} = \frac{1}{S_{ratio}} \cdot C_{Upper\ membrane} =$	10 nF	Calculated
$C_{Stray} =$		10 pF	Experimental
$R_{Leak} =$		120 k Ω	Experimental

The equivalent electrical schematic was simulated using Matlab Simulink (R2016a, MathWorks, US) according to the values detailed in Table 4.2. Figure 4.12 b) & c) shows the theoretical impedance magnitude and phase obtained with the electric equivalent model.

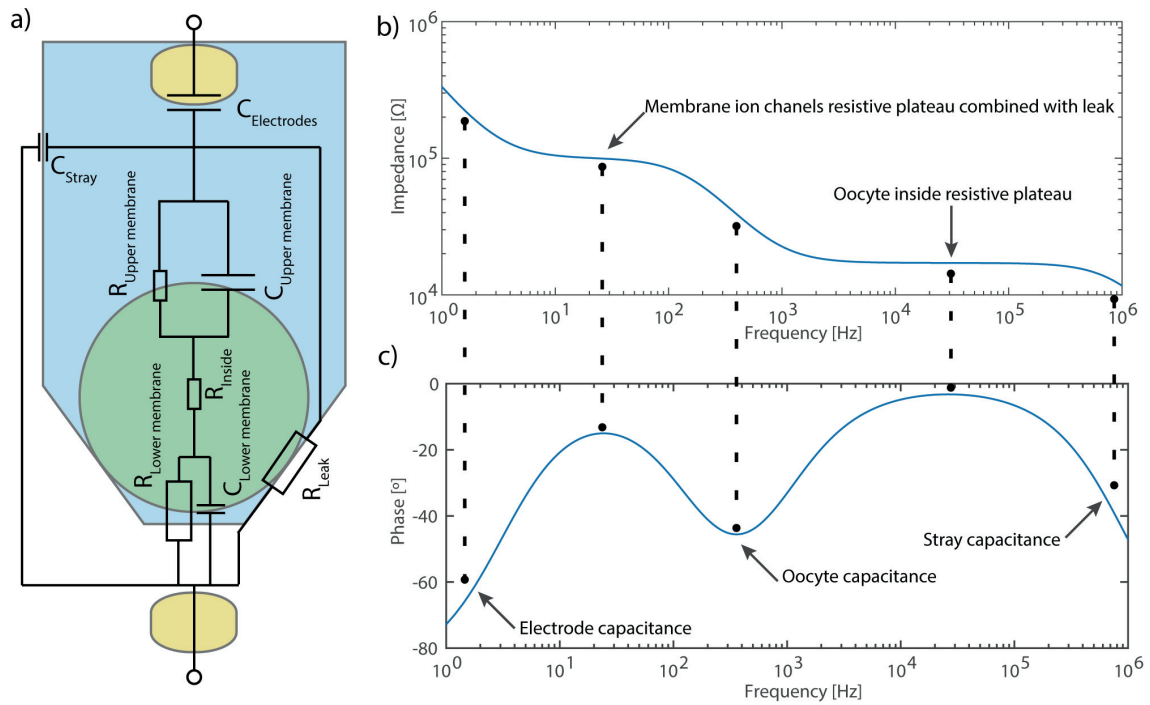


Figure 4.12: Electrical equivalent model of an oocyte in the transoocyte chamber: a) equivalent electrical schematic. b) Magnitude and phase impedance spectra evaluated according to the electrical equivalent model.

Impedance spectra shown in Figure 4.12 b) and c) presents the following domains. Below 10 Hz, the impedance is dominated by the electrodes capacitance $C_{Electrodes}$.

Around 30 Hz, the first resistive plateau is dominated by the lower patch membrane resistance $R_{Lower\ membrane}$ in parallel with the leak resistance R_{Leak} . The upper membrane patch resistance $R_{Upper\ membrane}$ connected in series does not contribute significantly as representing a resistance 20 times smaller due to the asymmetry. The oocytes inside resistance R_{Inside} does not either contributes significantly in this first plateau, as its resistance is one order of magnitude smaller. Under those assumptions, the resistive plateau at 30 Hz is defined by the lower membrane ions channel permeability defining the lower patch membrane resistance $R_{Lower\ membrane}$ together with the leak resistance R_{Leak} in parallel. The clear advantage of this configuration is the ability to immerse the lower membrane patch and its ion channels in different solutions to measure its corresponding impedance.

The cut-off frequency due to the lower patch membrane capacitance $C_{Lower\ membrane}$ occurs around 400 Hz. This cut-off is defined by the frequency where the lower membrane patches capacitance $C_{Lower\ membrane}$ presents an impedance smaller than the lower membrane patches resistance $R_{Lower\ membrane}$ and leads the AC current to flow preferentially through the capacitive path.

Above this cut-off frequency, a second resistive plateau is observed at 30 kHz and dominated by the oocytes internal resistance R_{Inside} . In this case the leak resistance R_{Leak} is not considered because it has a value at least one order of magnitude bigger and connected in parallel.

Finally, above 100 kHz, the stray capacitance C_{Stray} of the glass pipette and setup starts dominating the total impedance.

The region of interest is centered between 30 Hz and 30 kHz as representing respectively the lower patch resistance defined the ion channel permeability, the oocytes capacitance and finally the oocyte internal resistance.

4.3.3 Results

4.3.3.1 *Oocytes impedance spectra*

Impedance spectra of oocytes placed in the transoocyte chamber are measured experimentally and compared with the electrical model (§4.3.2.2) in the following section.

Figure 4.13 shows magnitude and phase impedance spectra of 3 oocytes (not injected). Each oocyte was inserted in the transoocyte chamber filled with NFR. After the oocyte sediment to the tip of the glass pipette, the tip of the transoocyte chamber was immersed into a well containing NFR. Impedance measurements were performed using the impedance analyzer (Agilent 4294A, Agilent technologies, US) between 40Hz as being the minimal frequency achievable with the impedance spectrometer to 400kHz and with an excitation amplitude of 50 mV.

These curves show a first domain between 40 Hz and 100 Hz presenting the end of a resistive plateau defined by a phase smaller than 30° and with average magnitudes of 80 kΩ representing the lower membrane patch resistance combined in parallel with the leak resistance. The frequency range between 100 Hz and 2000 Hz represents a capacitive region defined by lower membrane patch cut-off frequency around 200 Hz. The third region centered at 30 kHz presents a second resistive plateau with average magnitudes of 16 kΩ and defining the oocyte internal resistance. The last capacitive region begins above 100 kHz and demonstrates a limited stray capacitance of the setup allowing to cover a wide range of frequencies for impedance measurements. These measured impedance spectra are in agreement with the oocyte electric equivalent model and the selected region of interest between 40 Hz and 40kHz allows the extraction of oocyte parameters such as the lower patch membrane resistance combined with the leak resistance, the lower patch membrane capacitance and the oocyte internal resistance.

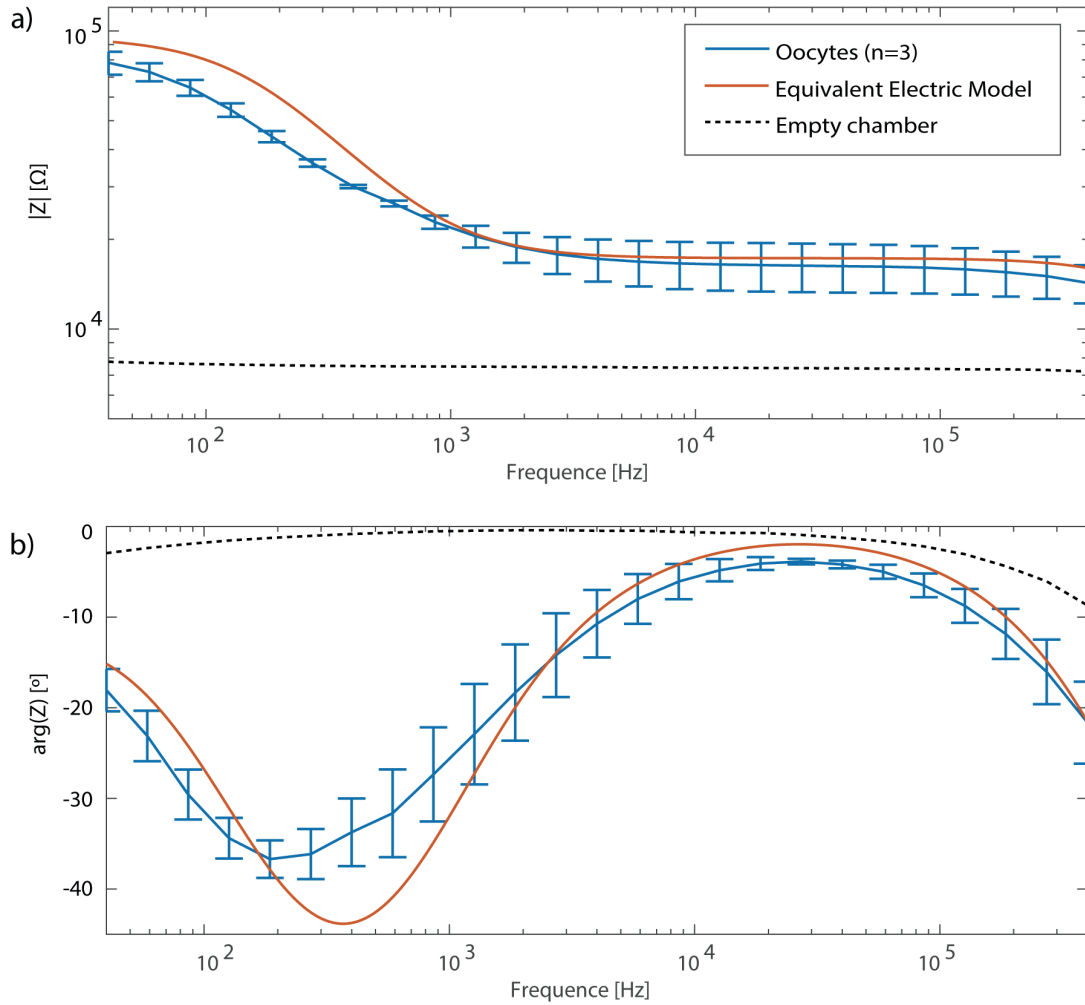


Figure 4.13 : *Xenopus laevis* oocyte impedance spectra in the transoocyte chamber. a) Impedance magnitude spectra measured for 3 oocytes and the empty chamber compared with the magnitude impedance spectra obtained with the electric equivalent model. b) Impedance phase spectra measured for 3 oocytes and the empty chamber compared with the magnitude impedance phase obtained with the electric equivalent model.

4.3.3.2 Ion channels modulation spectra

Figure 4.14 presents an experiment where *Xenopus Laevis* oocytes expressing Sodium Epithelial Channel (ENaC) were measured in combination with amiloride to evaluate the detection of ion channels permeability modulation by impedance spectroscopy accordingly to the principle described in Figure 4.12. Oocytes expressing ENaC were placed one by one in the transoocyte chamber. Impedance spectra were acquired every 3 seconds using the impedance analyzer (Agilent 4294A, Agilent technologies, US) with excitation frequency between 40 Hz and 400 kHz as well as an excitation frequency of 50 mV. At the beginning of

the experiment, the measurement chamber tip containing the oocyte was immersed in NFR solution. After 120 seconds, the tip was retracted from the initial solution and immersed in another NFR solution containing 200 μ M amiloride. As amiloride is an ENaC blocker, the lower patch membrane resistance measured in the first resistive plateau is expected to increase after immersion in amiloride solution.

Figure 4.14 a) shows magnitude impedance spectra between 40 Hz and 400 kHz superimposed for different measurement times. Spectra representing the beginning of the experiment are shown at the bottom of the graph and their magnitude increase along with time after the immersion of the transoocyte chamber tip in the NFR solution containing amiloride. These spectra and their increase in time illustrate the effect of ion channel blocking on the impedance spectra with an effective impedance increase observed only for frequencies below 200 Hz in the first resistive plateau.

Figure 4.14 b) shows the magnitude impedance along time for the same data set at the two selected frequency of 40 Hz (blue curve) and 30 kHz (red curve). It shows again that only the magnitude impedance measured at low frequency (40 Hz) increase when the tip is immersed in the amiloride solution. This curve also shows the kinetic of the impedance increase after the immersion into the amiloride solution with a time constant evaluated at 100 s.

Figure 4.14 c) presents a summary of the measurements performed on the 3 oocytes expressing ENaC with a relative impedance increase at 40Hz of 22% (cv = 11%) after the immersion of the tip containing the oocyte into the amiloride solution while the relative impedance increase observed at 30 kHz was less than 1 % (cv < 1%).

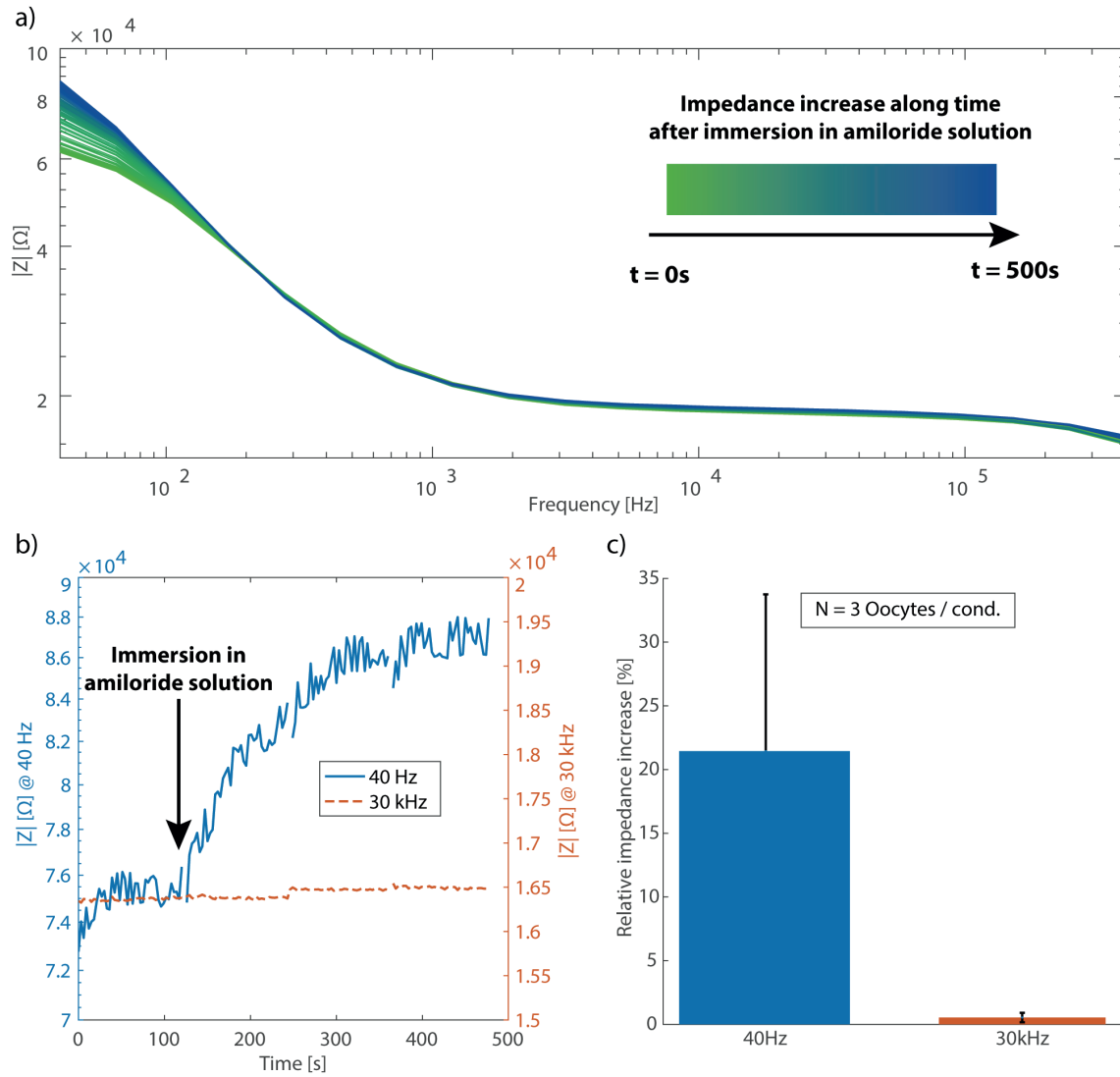


Figure 4.14 : Ion channels modulation spectra: a) Impedance spectra of an ENaC injected oocyte showing magnitude increase along time consecutive to the transoocyte tip immersion in NFR solution containing amiloride. The impedance increase is due to the ENaC blocking by amiloride and is observed in a frequency range below 200 Hz. b) Same data set with impedance magnitude selected for 40 Hz and 30 kHz excitation frequencies. c) Average impedance increase observed for 3 oocytes at 40 Hz and 30 kHz.

4.3.3.3 Ion channels expression spectra

Figure 4.15 presents an experiment where *Xenopus Laevis* oocytes expressing ENaC were compared to not injected oocytes to determine the effect of ion channels expression on the impedance spectra. The measurement is performed using the impedance analyzer (Agilent 4294A, Agilent technologies, US) with excitation frequency between 40 Hz and 400 kHz as well as an excitation frequency of 50 mV. The transoocyte chamber tip containing the oocyte

was immersed in NFR for both oocytes groups. 11 ENaC injected oocytes and 6 not injected oocytes were tested. The two curves show the average impedance magnitude of the two oocytes groups with a lower impedance magnitude for ENaC injected oocytes below 1 kHz. This impedance decrease represents the lower patch membrane permeability increase due to ENaC expression. For the other frequencies, the difference in impedance magnitude is not statistically relevant and is fully comprised in standard deviation of both measurements.

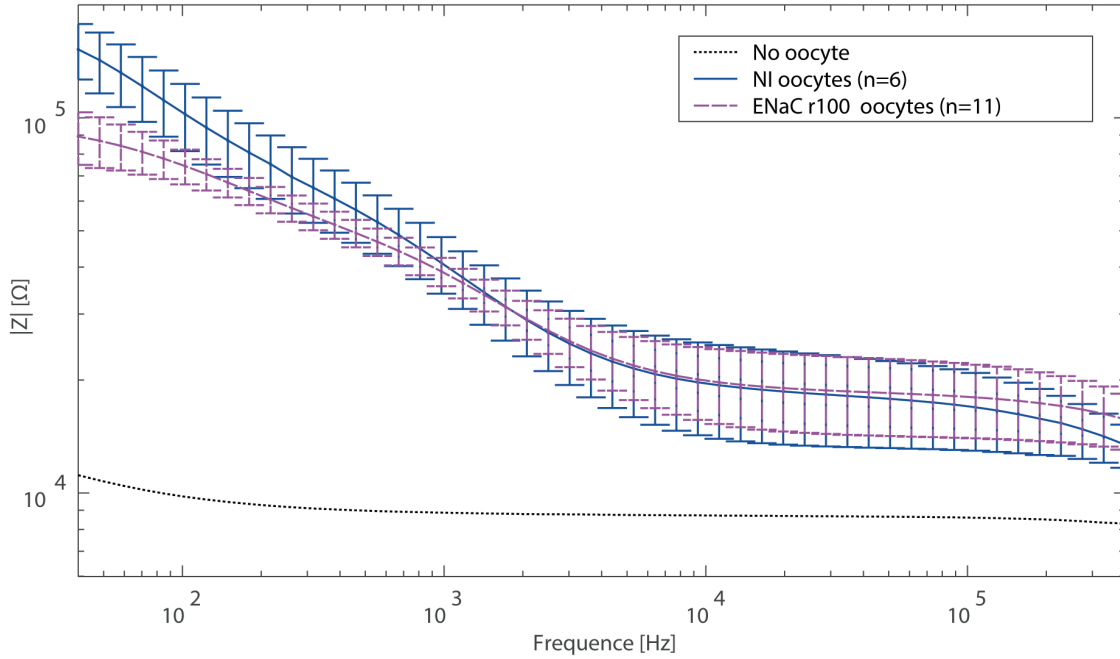


Figure 4.15 : Ion channels expression spectra: Impedance spectra of 11 ENaC injected oocytes, 6 oocytes not injected and the transoocyte chamber without oocyte. The impedance spectra of the ENaC injected oocytes presents a magnitude significantly lower than not injected oocytes in the frequency range below 1 kHz due to the expression of ENaC increasing the membrane permeability.

4.3.3.4 Single frequency impedance measurements of ion channels modulation for integrated systems

Results presented in Figure 4.14 and Figure 4.15 demonstrate that statistically significant oocytes impedances changes due to the modulation of ion channels or their expression level are restricted to the first resistive plateau below 200 Hz. Consequently, the impedance analyzer used to perform this measurement can be considerably simplified if restricted to a single frequency centered in the first resistive plateau at 25 Hz.

For this purpose, a simple and integrable single-frequency impedance analyzer was developed and shown in Figure 4.16 a). This integrable single-frequency impedance analyzer use the lock-in demodulation principle performed by integrated lock-in demodulator (SI-QSD, Sensima, CH). On one electrode, an excitation frequency of 25 Hz with amplitude of 50 mV is applied by the SI-QSD. From the other electrode, the current is amplified using a transimpedance amplifier (OPA2350, TI, USA). The amplified current is measured and the impedance is determined using the acquisition, demodulation and filtering capability of the SI-QSD. This custom circuit is connected to a microcontroller kit (Nano, Arduino, IT) to transmit the impedance value from the SI-QSD to the computer. Figure 4.16 a) shows that such a simplification allows of a fully embedded setup comprising both the measurement chamber and the impedance analyzer.

Figure 4.16 b) presents an experiment where *Xenopus Laevis* oocytes expressing Sodium Epithelial Channel (ENaC) were used in combination with amiloride to detect ion channel modulation with the integrable single-frequency impedance analyzer shown in Figure 4.16 a). Oocytes were placed in the transoocyte chamber one by one. Impedance magnitude at 25 Hz was acquired every 3 ms. At the beginning of the experiment, the transoocyte chamber tip containing the oocyte was immersed in low Na MBS solution. After 180 seconds, the tip is retracted from the initial solution and immersed in another solution containing standard MBS solution. After 330 seconds, the tip was then immersed in MBS solution containing amiloride.

Figure 4.16 b) shows the magnitude impedance at 25 Hz along time for an oocyte expressing ENaC as well as a not injected oocyte. This curve illustrates the effect of ENaC blocking on the oocyte lower patch membrane resistance at a single frequency of 25 Hz combined with a simple setup and impedance analyzer. Figure 4.16 c) shows a summary of the measurements performed on 4 oocytes expressing ENaC and 4 not injected oocytes. Measurement on ENaC expressing oocytes shows an average impedance increase of 54% (cv = 50%) after the immersion of the tip containing the oocyte into the amiloride solution while the not injected oocyte shows an impedance increase smaller of 0.3% (cv = 7%).

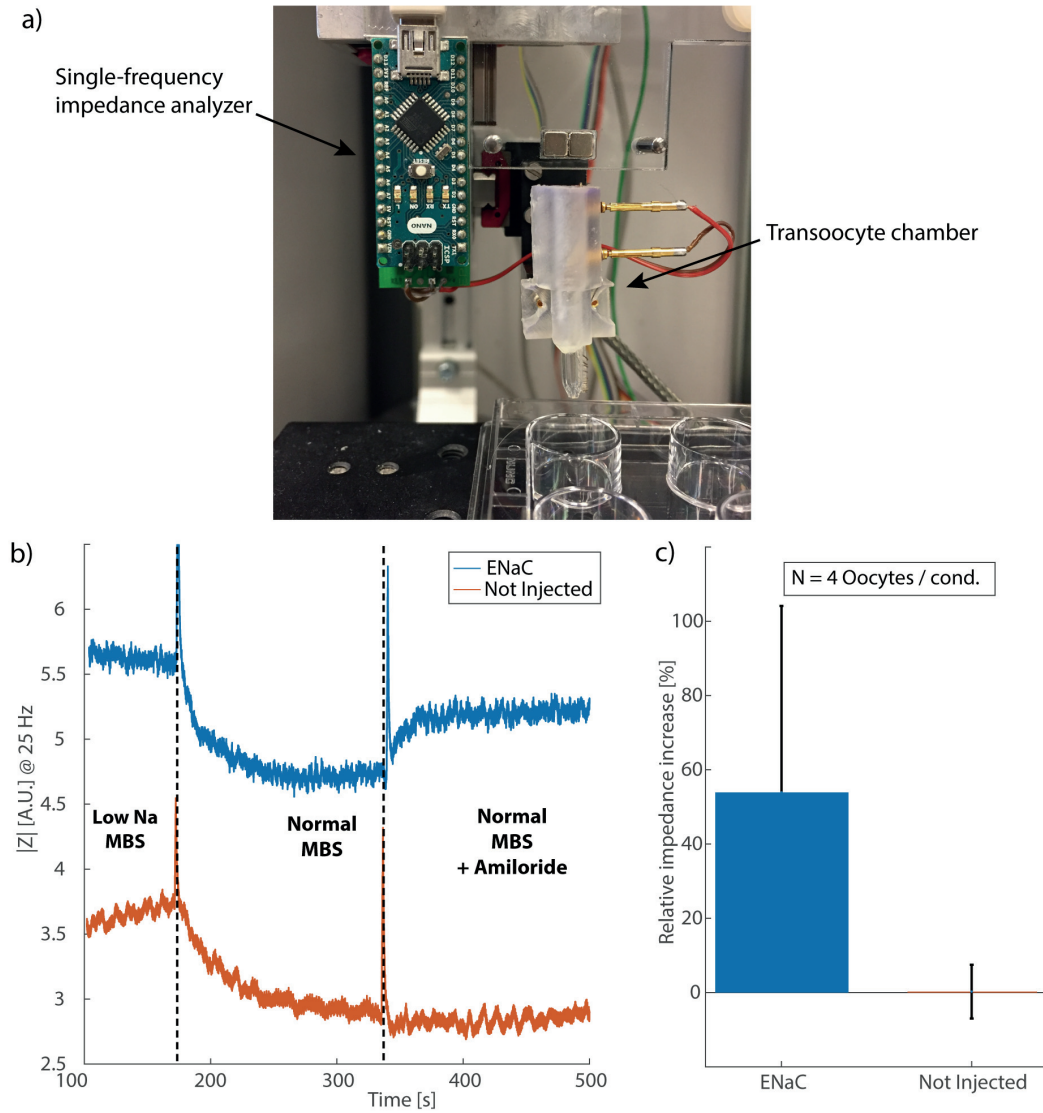


Figure 4.16 : Single frequency impedance measurements of ion channels modulation. a) Integrated single-frequency impedance analyzer combined with the transoocyte chamber. b) Impedance magnitude of an oocyte ENaC injected (blue curve) and an oocyte not injected (red curve). Both oocytes are successively immersed in Low Na MBS solution, normal MBS solution and normal MBS solution containing amiloride. The Impedance of the oocyte expressing ENaC increases when immersed in the solution containing amiloride while the impedance of the oocyte not injected stays at the same value. c) Average impedance increase observed for 4 oocytes expressing ENaC and 4 oocytes not injected.

4.3.4 Strategies to increase the seal

According to the equivalent electric schematic presented in Figure 4.12, the main limitation to have a high sensitivity to ion channel resistance is the leak resistance in parallel with the oocyte. Similarly to observations made for patch clamp (Hamill, 1981), MEA (Spira, 2013) or the preliminary nerve recording experiments presented the previous section (§4.2.2), the cell need to be segmented to measure specifically the lower patch membrane resistance. The sensitivity to the lower membrane resistance increase with the increase of the leak resistance as connected in parallel. Two approaches are discussed to increase the leak resistance in this section.

4.3.4.1 Sucrose perfusion chamber

A specificity of the *Xenopus laevis* oocyte is the vitelline membrane surrounding the cell membrane. Because the vitelline membrane is permeable to ions, it allows electrical current to bypass the oocyte by circulating in the vitelline membrane without crossing the cell membrane. Consequently the leak resistance required to segment the oocyte membrane is decreased.

One solution to control the leak resistance is to replace the conductive solution contained in the vitelline membrane with a non-conductive solution. This can be performed by perfusing the vitelline membrane with a sucrose solution. Sucrose is a non-charged molecule, allowing to adjust the solution osmolarity while preventing electrical conduction in the vitelline membrane.

Figure 4.17 a) shows the design of a sucrose perfusion system for *Xenopus laevis* oocytes. The oocyte sits on a cavity made of three layers. The top layer showed in Figure 4.17 b) is 100µm thick and comprises a 900 µm hole to accommodate and position the oocyte. The top layer also comprises upper measurement electrodes. The mid layer showed in Figure 4.17 c) comprise a 1.2 mm in diameter and 80 µm thick cavity filled with sucrose solution to perfuse the oocyte vitelline membrane and insulate the oocyte lower membrane section from its upper membrane section. Sucrose solution is circulated into this cavity by a 150 µm wide and 80 µm height channel. The lower layer showed in Figure 4.17 d) is also 100 µm thick and comprise a small aperture of 300 µm. This aperture defines the lower membrane patch section to be perfused with the ligand solution acting on the lower membrane ion channels. The lower layer also contains the lower recording electrodes.

All the layers are made of two printed circuit boards (PCB) fabricated with a similar process as described in (§3.2). The PCBs includes the fluidic perfusion channel and are fabricated using a conventional PCB production line. The top and bottom layers consist of the epoxy PCB substrate with copper gold-plated electrodes. The mid layer consists of the fluidic channels structured in dry film resist deposited in one face of each PCB (§3.2). The two PCBs are bonded together with the dry film resist layer facing each other and using similar dry film resist as binding layer. The stack is placed for 10 min on a hot plate at 85 °C with a 220 g load onto it. A glass cupule is glued on the top layer to facilitate the oocyte placement during experiment as shown in Figure 4.17 f).

This stack is clamped in a polyoxymethylen (POM) made chamber integrating a cavity to perfuse the oocyte lower membrane as shown in Figure 4.17 e). The chamber also comprises the oocyte insertion well above the stack that is used to position the oocyte and filled with medium to contact the upper electrodes as shown in Figure 4.17 g). An adjustable vacuum source (AF1 Dual, Elveflow, FR) and a manifold are used to perfuse the oocyte lower membrane patch with different ligand solutions as shown in Figure 4.17 e). Oocyte impedance measurements are performed using the set of upper and lower electrodes. Figure 4.17 h) shows an oocyte placed in the glass cupule ready for measurement.

However, because of time constrains, no further experiments were conducted on this setup and an alternative solution to increase the leak resistance with fewer implementation constraints was envisaged and presented in the following section (§4.3.4.2).

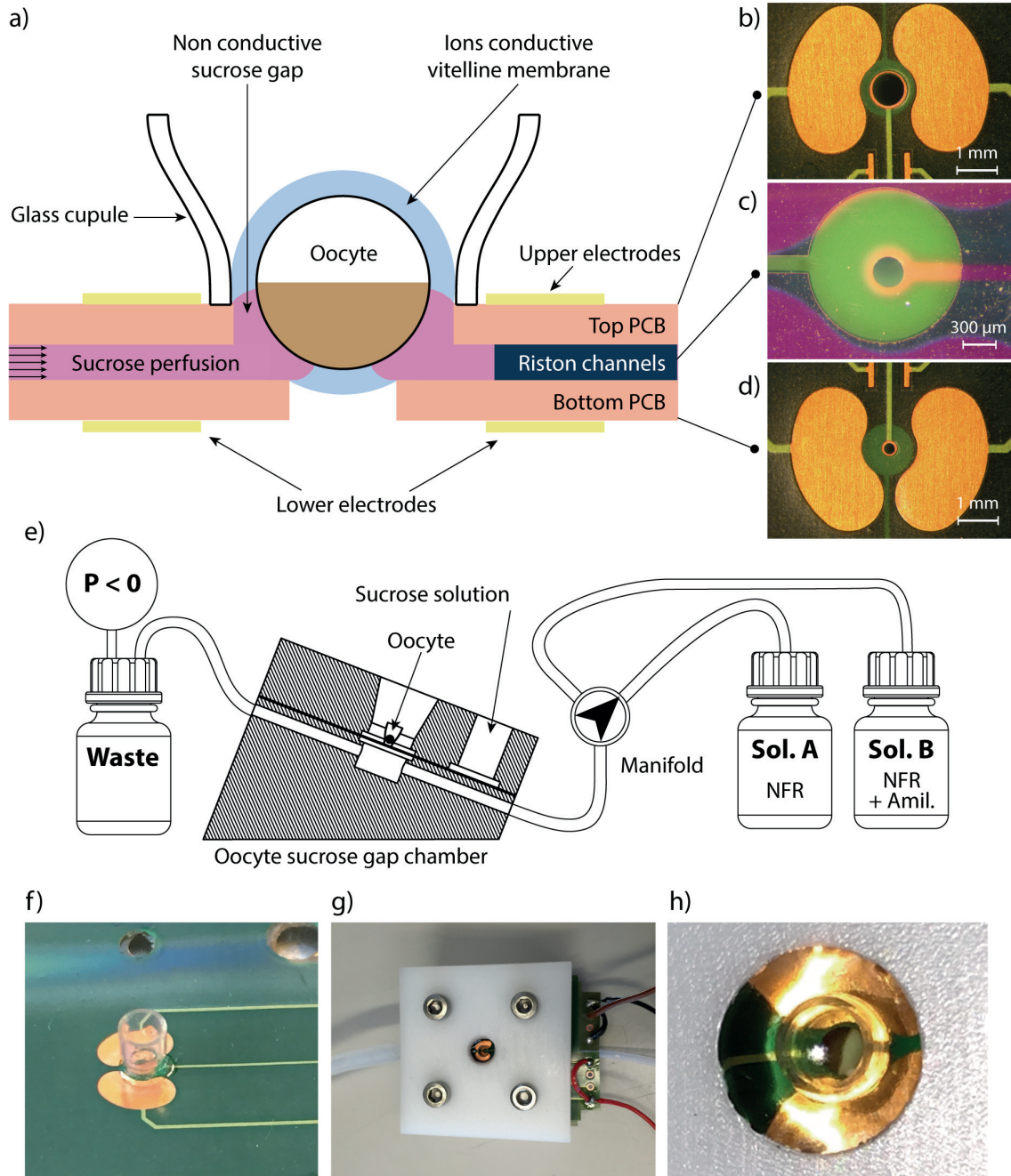


Figure 4.17 : Sucrose perfusion chamber. a) Design of the sucrose perfusion chamber to increase the leak resistance between the oocyte upper and lower membrane patches by perfusing the vitelline membrane with a non-conductive sucrose solution. b), c) & d) Picture of the PCB made layers to accommodate the oocyte and the sucrose perfusion. e) Perfusion and measurement principle with the sucrose perfusion chamber. f) Picture of the glass cupule helping in the oocyte positioning, g) & h) Picture of the sucrose perfusion chamber with an oocyte.

4.3.4.2 Localized impedance measurement with a microelectrode

An alternative method to segment the cell membrane and control the leak resistance between the membrane segments consists of applying a microelectrode on the oocyte surface as shown in Figure 4.18 a). The impedance measured with the microelectrode is mainly restricted in the spreading volume around the electrode and defined by its diameter. In this embodiment, the microelectrode consists of a 200 μm silver wire (Advent, UK) inserted and glued (Araldite, Hornbach, CH) in a dielectric cladding made of a plastic pipette tip (Multiflex round tip 200 μL , Sorenson BioScience, US) as shown in Figure 4.18 b) & c).

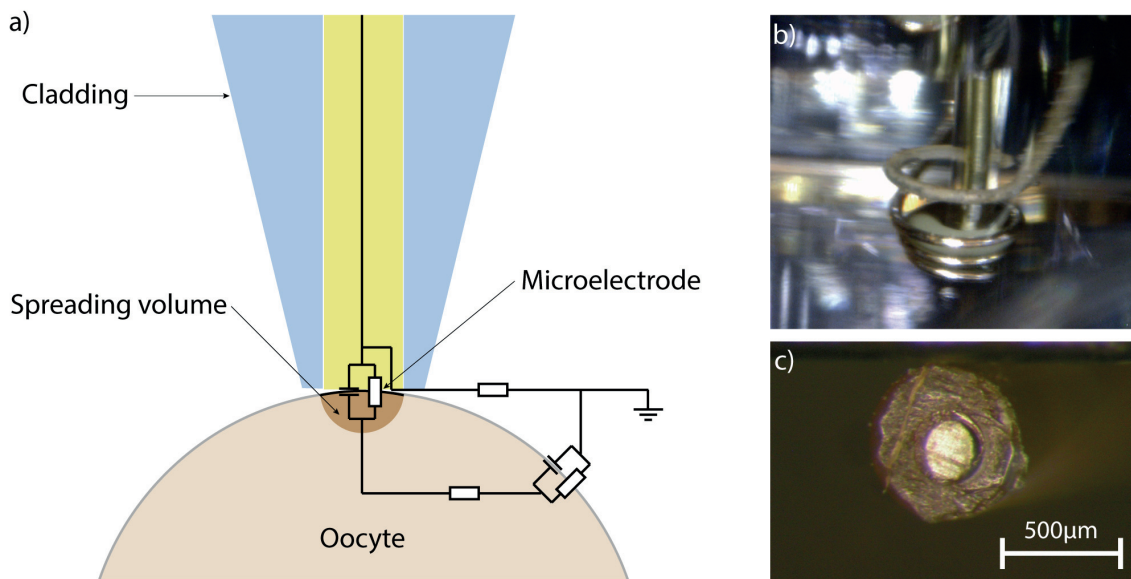


Figure 4.18 : Custom-made microelectrode a) Design of the custom-made microelectrode providing the cell membrane segmentation by the restricted electrode impedance spreading volume. b) Side view picture of the custom-made microelectrode in contact with an oocyte. c) Picture of the custom-made microelectrode tip exhibiting the inner conductive part.

To perform impedance measurement with the custom-made microelectrode, the oocyte is placed in a ground wire basket as used in HiClamp system (MCS) to be mechanically maintained. The custom-made microelectrode showed in Figure 4.18 a) is pushed against the oocyte using the HiClamp manipulator system (MCS). The impedance is measured using the impedance analyzer (Agilent 4294A, Agilent technologies, US) between the custom-made microelectrode and the platinum wire constituting the oocyte basket.

Figure 4.19 shows the impedance magnitude and phase of 3 oocytes measured with the transoocyte chamber and 3 other oocytes measured with the custom-made microelectrode. The magnitude impedance difference between the low and the high frequency resistive plateau is 96 k Ω for the proximity electrode and only 55 k Ω for the transoocyte chamber. Consequently, the microelectrode measurements show a higher contrast between the membrane resistance and the oocyte inside resistance. This impedance difference is 74% bigger in the case of the microelectrode measurement compared with the transoocyte measurements. Moreover the measurement setup is simplified because no oocyte sealing is considered unlike the case of the transoocyte chamber. Furthermore, the cut-off frequency defined by the lower membrane patch capacitance is also displaced from 200 Hz to 600 Hz when using the microelectrode compared to the transoocyte chamber. This is also an advantage to measure impedance variation at higher frequency with a lock-in demodulation system.

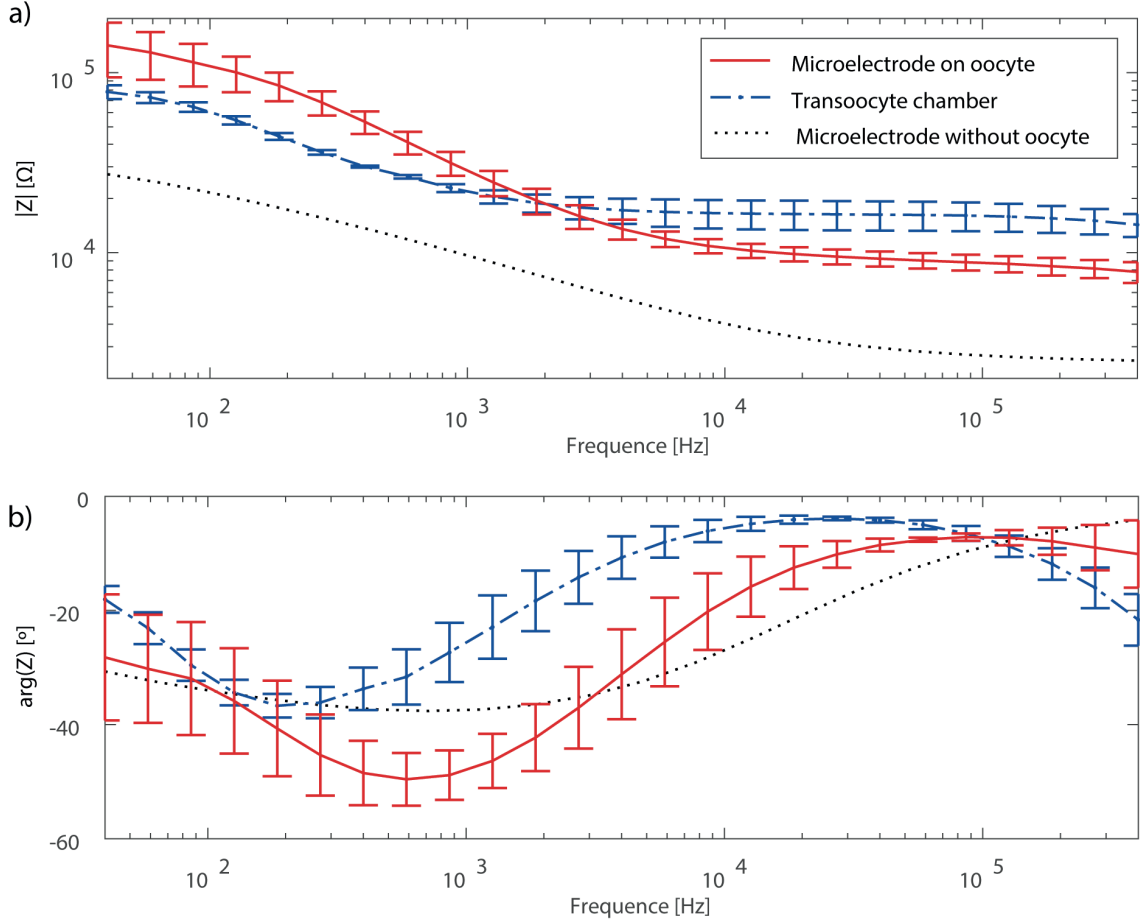


Figure 4.19 : Localized impedance measurement: *Xenopus laevis* oocyte impedance spectra obtained with the custom-made microelectrode compared with the transoocyte chamber. a) Impedance magnitude spectra measured for 3 oocytes with the microelectrode and 3 oocytes with the transoocyte chamber as well as the microelectrode without oocyte. b) Impedance phase spectra measured for 3 oocytes with the microelectrode and 3 oocytes with the transoocyte chamber as well as the microelectrode without oocyte.

4.4 Discussion

The different experiments performed during this study showed oocytes impedance spectra in agreement with the proposed model according to the cell membrane segmentation principle. It validates the selected ratio between the upper and lower membrane patches sections and shows that electrodes surfaces are sufficiently large and the stray capacitance sufficiently small to discriminate the lower patch membrane resistance, capacitance and the

oocyte inside resistance. It shows that the lower patch membrane resistance measurements can be performed in the 10 Hz to 100 Hz resistive plateau.

Experiments performed with ENaC injected oocytes and using amiloride validated the capability of measuring ion channel modulation using impedance spectroscopy and the transoocyte chamber setup. Similarly, it showed that the expression of ENaC compared to not injected oocytes can be measured using the same impedance spectroscopy principle. Importantly, both of those measurements were non-invasive and label free for the oocytes.

In agreement with the model, the impedance change is restricted to the lower frequency resistive plateau and suggests no significant ions rearrangement at the scale of the oocyte length but mainly the modulation of ion channel permeability and thus membrane conductivity. This allows performing the measurements at a single excitation frequency and simplifies considerably the instrumentation. For this purpose, a simplified instrumentation embodiment facilitating the system integration was proposed. Again, measurement of ion channels modulation was validated using ENaC oocytes and compared with not injected oocytes. The combination of this non-invasive method and the integrable single frequency impedance analyzer enable the development of embedded biosensor based on electrophysiology measurements.

The key element to access non-invasively the ion channel permeability is the membrane segmentation. According to the transoocyte chamber, the membrane segmentation is defined by the asymmetry between the section of upper and lower membrane patches. The critical parameter to control is the leak resistance between these two membrane segments. The leak resistance defines the impedance measurement sensitivity to the lower patch resistance variations. Similar bottleneck is observed in the different electrophysiology setups where membranes potential or current have to be measured without intracellular electrodes insertion. Well-known example are MEAs for action potential measurement (Spira, 2013), patch-clamp for single-channel current measurement (Hamill, 1981) or electrophysiology setup to observe light-induced current in single rod membrane (Baylor, 1979; Baylor, 1984). In our experiments, the lower membrane patch comprises a large amount of ion channels to the contrary of patch-clamp, thus a giga-ohm sealing is not required. Nevertheless a higher leak resistance will improve measurements sensitivity. It also explains the limited impedance variation observed in this study when over-expressed sodium epithelial channel are completely blocked by the amiloride.

Different solutions were envisaged to increase the leak resistance and consequently to increase the sensitivity to ion channel modulation. First, the vitellin membrane which is permeable to ions and conducting them along the glass pipette could be removed but this will dramatically weaken the oocyte. This solution is also difficult to conciliate with a high-throughput and automated procedures. Second, the conductive liquid contained in the vitelline membrane allowing current leak along the glass could be replaced by a non-conductive liquid. A solution is presented to perfuse the vitelline membrane with a glucose solution. Third, the oocyte segmentation obtained with the glass pipette could be replaced by a localized impedance measurement defined by the spreading volume of a microelectrode. In this study, it was shown that a microelectrode effectively measure the local oocyte membrane impedance defined by the microelectrode spreading volume. This remove the need to segment the membrane by a mechanical sealing and enable simplified setups and more convenient oocyte manipulation. Also, the use of the microelectrode instead of the transoocyte setup should allow to perform the demonstrated impedance measurements in flow cytometry settings similarly to examples illustrated in previous section (§1.1). These different possibilities to increase the leak resistance also suggest that the non-invasive character of this method does not intrinsically imply a low sensitivity to ion channel modulation.

Finally, this totally non-invasive solution, based on AC impedance measurement is obtained at the cost of a signal demodulation required to obtain the impedance signal. According to the amplitude modulation principle, the maximal bandwidth of the retrieved signal is half of the signal excitation frequency. The theoretical maximal applicable excitation frequency to measure the first resistive plateau is defined by lower membrane patch cut-off frequency, which is 200 Hz in our study. Consequently, no events containing frequencies above 100 Hz could be theoretically detected from ion channel modulation. It could be an important limitation for fast kinetic ion channel investigation. For this reason, the proximity microelectrode embodiment (§4.3.4.2) also showed to improve the system performance as the lower patch membrane cut-off frequency is shifted to 600 Hz.

Another caveat of the impedance spectroscopy is that it cannot be used to set the membrane potential at a given value. It prevents measuring any impedance changes related to the voltage potential itself or channels showing no current variation at their physiological potential level. A possible workaround could be the co-expression of channels with a specific permeability to ions with a different Nernst potential.

Chapter 5 : Conclusion & Future Work

5.1 Single cell dispensing using a pipette tip integrating an impedance sensor

The first contribution made in this thesis consists of allowing the retrieval and isolation of a single cell subsequent to its analysis using single cell impedance spectroscopy. It allows to extract with confidence the cell of interest and also to work with a limited amount of cells in input. This is achieved by designing a sensing tip integrating a Coulter counter combined with an instrumented pipette to enable single cell dispensing.

The sensing tip was optimized using an analytical model to exhibit a particle limit of detection down to 3.2 μm in size. This detection capability ensures a robust detection of mammalian cells in the range of 6 μm to 15 μm . Designing an electronic instrumentation with an appropriate noise level and choosing carefully the particle detection threshold, allows a highly reliable particle detection with a probability to miss a 6 μm particle passage smaller than 0.002. Furthermore, placing the Coulter counter at the interface of the sensing tip leaves no dead volume between the particle detection volume and the receiving container. Together, those elements enable to perform single cell dispensing with confidence and reliability. The cost effective batch process of the sensing tip permits to use them as disposable devices and enable cell culture with the isolated single cell. Also, integrating the tool in standard pipette format prevents a radical change of biologists habits and facilitates its integration in existing cell culture workflows. Furthermore, it is shown that the use of this single cell dispensing tool does not affect the cell viability. Finally, the recording of the impedance time trace allows for a traceable dispensing of single cell. All these features are of primary importance for cell cloning applications such as cell lines development in highly regulated contexts of drugs production.

Experimentations also highlighted the main limitations of the sensing tip. It consists of a limited fluidic control capability due to a small hydraulic resistance. It leads to a sub-optimal plate filling rate with single cells. In a future work, different means could be envisaged to overcome this limitation. The complete automation of the procedure would permit to control the external factors influencing on the particle dispensing such as tip immersion level and the time spend in the well. This could improve the plate filling rate and also increase the throughput of this method. Alternatively, adding a resistive plug in the

fluid path could also increase the sensing tip hydraulic resistance and permits a higher plate filling rate using a handheld device.

5.2 Cost effective and large scale manufacturing of flow cytometers

The second contribution of this thesis consists in the translation of the disposable, sterile and low-cost single cell dispensing concept on a standard planar microfabrication technology. A planar fabrication method based on the industrially standardized printed circuit board (PCB) manufacturing process is studied to produce different topologies of flow cytometers with emphasis on the disposable aspect of those devices required for cell culture.

Thanks to the advances in the PCB fabrication capabilities, the resolution and material currently used in this field merge with BioMEMS applications such as flow cytometers. In this thesis, the possibility to fabricate flow cytometers using standard PCB production lines and PCB design softwares is demonstrated and their performances are characterized. Even though some design and material constraints have to be respected to produce a flow cytometer in a PCB production line, it is shown that this category of BioMEMS chip can advantageously benefit from the standardized and cost effective PCB fabrication industry in the vision of producing disposable devices.

Irrespective of fabrication methods, planar designs of flow cytometers also showed to be an effective solution to conciliate the high particle sensitivity of the Coulter counter topology observed in the sensing tip and the high hydraulic resistance controlled by long microfluidic channels. A future version of the single cell dispensing tool could be based on this planar technology to present an improved fluidic control capability and further increase the single cell plate filling rate. This planar version could also benefit from a smaller stray capacitance. Consequently, impedance spectroscopy could be performed at higher excitation frequencies and would enable the characterization of cell parameters such as their viability during the single cell dispensing. A planar design could also permit the integration of further fluidic functions such as cell sorting. Combined with cell size and viability analysis, the sorting

capability would enable the isolation single cells of specific interest while rejecting the other cells.

5.3 Impedance spectroscopy for active cells analysis

The third contribution of the thesis consists of further exploring cell parameters that can be analyzed by impedance spectroscopy. For this purpose, *Xenopus laevis* oocytes are selected as an effective protein expression system and because of their large size allows an easy handling. A transoocyte chamber to perform impedance spectroscopy measurements on the oocyte is designed. Impedance spectra expected from the cellular dielectric structure are observed and permit to measure cellular parameters including the membrane resistance, membrane capacitance and the cell inside resistance. In this thesis, it is shown that the modulation of ion channels permeability such as ENaC can be observed non-invasively using impedance spectroscopy. Using the same method, the expression of ENaC can also be measured. A model describing the spatiotemporal ion distribution related to ion channel modulation is proposed. According to this model and in agreement with experiments, the main effect of channel modulation at the whole cell level consists in the change of the membrane resistance. Alternatively, ions rearrangement and local changes of the cytosol conductivity are restricted in a slice of 1 nm around the cell membrane. Measuring this very localized effect would requires another approach such as using nanoelectrodes presenting a resistance spreading volume in the range of nanometers or to select a much smaller cellular organism.

The different experiments performed during this thesis showed that the key parameters enabling non-invasive cell measurements is the segmentation of the cell membrane and the control of the leak resistance between those segmented domains. Experiments presented in this thesis showed a limited sensitivity to ion channel modulation because of a small leak resistance caused by the vitelline membrane surrounding the oocyte. Different approaches were considered to circumvent this limitation. A solution to decrease the vitellin membrane ionic conductivity in the sealing region and to segment more efficiently the oocyte membrane consisting of a sucrose perfusion chamber is proposed. Alternatively, the application of a microelectrode directly on the oocyte membrane showed to be another

efficient way to perform the cell membrane segmentation and turns out to be a much simpler embodiment compared to the transoocyte chamber. Moreover, the use of a contact microelectrode reconciles the impedance spectroscopy measurement method with conventional flow cytometry applications. In a future work, a flow cytometer measuring the oocyte viability or channel expression level could be envisaged.

This work constitutes a step toward long-term, automated and integrated cellular electrophysiology monitoring required to develop cell biosensors based on ligand-gated ion channel modulation. Also it suggests that a compromise on the selected cellular organism is required to obtain better performances. The oocyte is an efficient model for protein expression and easy to handle because of its large size but the cell membrane segmentation with a high leak resistance is difficult to obtain because of the vitelline membrane. To continue with the development of ligand-gated ion channel based biosensors, it could be of advantage to select another cellular model closer to what is used in electroantennography. It could permit to conciliate the facile membrane segmentation required for an effective non-invasive measurement and the specific expression of ligand-gated ion channels for chemical detection.

Chapter 6 : **References**

- Agre, P., Preston, G. M., Smith, B. L., Jung, J. S., Raina, S., Moon, C. H. ... & Nielsen, S. (1993). Aquaporin CHIP: the archetypal molecular water channel. *American Journal of Physiology-Renal Physiology*, 265(4), F463-F476.
- Altuna, A., de la Prida, L. M., Bellistri, E., Gabriel, G., Guimerá, A., Berganzo, J., ... & Fernández, L. J. (2012). SU-8 based microprobes with integrated planar electrodes for enhanced neural depth recording. *Biosensors and Bioelectronics*, 37(1), 1-5.
- Ashkin, A., Dziedzic, J. M., & Yamane, T. (1987). Optical trapping and manipulation of single cells using infrared laser beams. *Nature*, 330(6150), 769-771.
- Attia, U. M., Marson, S., & Alcock, J. R. (2009). Micro-injection moulding of polymer microfluidic devices. *Microfluidics and Nanofluidics*, 7(1), 1-28.
- Ayliffe, H. E., & King, C. S. (2011). *Instrumented pipette tip*. U.S. Patent No. 8,015,887. Washington, DC: U.S. Patent and Trademark Office.
- Ayliffe, H. E., Frazier, A. B., & Rabbitt, R. D. (1999). Electric impedance spectroscopy using microchannels with integrated metal electrodes. *Journal of Microelectromechanical systems*, 8(1), 50-57.
- AZO Material (2012), The Coulter Principle for Particle Size Analysis, <http://www.azom.com/article.aspx?ArticleID=6020>, Accessed on March 22, 2016
- Bargeton, B., & Kellenberger, S. (2010). The contact region between three domains of the extracellular loop of ASIC1a is critical for channel function. *Journal of Biological Chemistry*, 285(18), 13816-13826.
- Barnard, E. A., Miledi, R., & Sumikawa, K. (1982). Translation of exogenous messenger RNA coding for nicotinic acetylcholine receptors produces functional receptors in *Xenopus* oocytes. *Proceedings of the Royal Society of London B: Biological Sciences*, 215(1199), 241-246.
- Barrandon, Y., & Green, H. (1985). Cell size as a determinant of the clone-forming ability of human keratinocytes. *Proceedings of the National Academy of Sciences*, 82(16), 5390-5394.
- Bashir, R. (2004). BioMEMS: state-of-the-art in detection, opportunities and prospects. *Advanced drug delivery reviews*, 56(11), 1565-1586.
- Baylor, D. A., Lamb, T. D., & Yau, K. W. (1979). The membrane current of single rod outer segments. *The Journal of Physiology*, 288(1), 589-611.
- Baylor, D. A., Matthews, G., & Nunn, B. J. (1984). Location and function of voltage-sensitive conductances in retinal rods of the salamander, *Ambystoma tigrinum*. *The Journal of Physiology*, 354, 203.

- Boppart, S. A., Wheeler, B. C., & Wallace, C. S. (1992). A flexible perforated microelectrode array for extended neural recordings. *IEEE transactions on biomedical engineering*, 39(1), 37-42.
- Bray, R. A. (1994). Flow cytometry crossmatching for solid organ transplantation. *Methods in cell biology*, 41, 103-119.
- Buffi, N., Merulla, D., Beutier, J., Barbaud, F., Beggah, S., Van Lintel, H., ... & van der Meer, J. R. (2011). Development of a microfluidics biosensor for agarose-bead immobilized *Escherichia coli* bioreporter cells for arsenite detection in aqueous samples. *Lab on a Chip*, 11(14), 2369-2377.
- Canessa, C. M., Schild, L., Buell, G., Thorens, B., Gautschi, I., Horisberger, J. D., & Rossier, B. C. (1994). Amiloride-sensitive epithelial Na⁺ channel is made of three homologous subunits. *Nature*, 367(6462), 463.
- Di Carlo, D., & Lee, L. P. (2006). Dynamic single-cell analysis for quantitative biology. *Analytical chemistry*, 78(23), 7918.
- Chen, D., Lear, J., & Eisenberg, B. (1997). Permeation through an open channel: Poisson-Nernst-Planck theory of a synthetic ionic channel. *Biophysical Journal*, 72(1), 97-116.
- Chen, J., Shakiba, N., Tan, Q., & Sun, Y. (2012). Single-Cell Impedance Spectroscopy. In *Encyclopedia of Nanotechnology* (pp. 2425-2429). Springer Netherlands.
- Cheung, K. C., Di Berardino, M., Schade-Kampmann, G., Hebeisen, M., Pierzchalski, A., Bocsi, J., ... & Tárnok, A. (2010). Microfluidic impedance-based flow cytometry. *Cytometry Part A*, 77(7), 648-666.
- Cheung, K. C., Renaud, P., Tanila, H., & Djupsund, K. (2007). Flexible polyimide microelectrode array for in vivo recordings and current source density analysis. *Biosensors and Bioelectronics*, 22(8), 1783-1790.
- Cheung, K., Gawad, S., & Renaud, P. (2005). Impedance spectroscopy flow cytometry: on-chip label-free cell differentiation. *Cytometry Part A*, 65(2), 124-132.
- Cole, K. S. (1949). Dynamic electrical characteristics of the squid axon membrane. *Archives des sciences physiologiques*, 3(2), 253-258.
- Coulter, W. H. (1953). *Means for counting particles suspended in a fluid*. U.S. Patent No 2,656,508. Washington, DC: U.S. Patent and Trademark Office.
- Coulter, W. H. (1956). High speed automatic blood cell counter and cell size analyzer. In *Proc Natl Electron Conf* (Vol. 12, pp. 1034-1040).

- Coulter, W. H., & Hogo, W. R. (1970). *Signal modulated apparatus for generating and detecting resistive and reactive changes in a modulated current path for particle classification and analysis*. U.S. Patent No. 3,502,974. Washington, DC: U.S. Patent and Trademark Office.
- Coulter, W. H., & Rodriguez, C. M. (1988). *Particle analyzer for measuring the resistance and reactance of a particle*. U.S. Patent No. 4,791,355. Washington, DC: U.S. Patent and Trademark Office.
- Coulter, W., & Hogg, W. (1973). *Electronic particle analyzing apparatus with improved aperture tube*. U.S. Patent No. 3,714,565. Washington, DC: U.S. Patent and Trademark Office.
- Craig, F. E., & Foon, K. A. (2008). Flow cytometric immunophenotyping for hematologic neoplasms. *Blood*, 111(8), 3941-3967.
- Dahan, E., Bize, V., Lehnert, T., Horisberger, J. D., & Gijs, M. A. M. (2007). Integrated microsystem for non-invasive electrophysiological measurements on *Xenopus* oocytes. *Biosensors and Bioelectronics*, 22(12), 3196-3202.
- Dahan, E., Bize, V., Lehnert, T., Horisberger, J. D., & Gijs, M. A. M. (2008). Rapid fluidic exchange microsystem for recording of fast ion channel kinetics in *Xenopus* oocytes. *Lab on a Chip*, 8(11), 1809-1818.
- Dascal, N. (1987). The use of *Xenopus* oocytes for the study of ion channel. *Critical Reviews in Biochemistry*, 22(4), 317-387.
- Davies, D. (2007). Cell Sorting by Flow Cytometry. *Flow Cytometry*, 257.
- Demierre, N., Braschler, T., Linderholm, P., Seger, U., Van Lintel, H., & Renaud, P. (2007). Characterization and optimization of liquid electrodes for lateral dielectrophoresis. *Lab on a Chip*, 7(3), 355-365.
- Dunlop, J., Bowlby, M., Peri, R., Vasilyev, D., & Arias, R. (2008). High-throughput electrophysiology: an emerging paradigm for ion-channel screening and physiology. *Nature reviews Drug discovery*, 7(4), 358-368.
- Eisenberg, B. (1998). Ionic channels in biological membranes: natural nanotubes. *Accounts of chemical research*, 31(3), 117-123.
- Evans, K., Albanetti, T., Venkat, R., Schoner, R., Savery, J., Miro-Quesada, G., ... & Groves, C. (2015). Assurance of monoclonality in one round of cloning through cell sorting for single cell deposition coupled with high resolution cell imaging. *Biotechnology progress*, 31(5), 1172-1178.
- Fröhlich, J., & König, H. (2000). New techniques for isolation of single prokaryotic cells. *FEMS microbiology reviews*, 24(5), 567-572.

- Fuller, S. A., Takahashi, M., & Hurrell, J. G. (2001). Cloning of hybridoma cell lines by limiting dilution. *Current Protocols in Molecular Biology*, 11-8.
- Fulwyler, M. J. (1965). Electronic separation of biological cells by volume. *Science*, 150(3698), 910-911.
- Gawad, S., Cheung, K., Seger, U., Bertsch, A., & Renaud, P. (2004). Dielectric spectroscopy in a micromachined flow cytometer: theoretical and practical considerations. *Lab on a Chip*, 4(3), 241-251.
- Gawad, S., Schild, L., & Renaud, P. (2001). Micromachined impedance spectroscopy flow cytometer for cell analysis and particle sizing. *Lab on a Chip*, 1(1), 76-82.
- Gillespie, D. T. (1996). The mathematics of Brownian motion and Johnson noise. *American Journal of Physics*, 64(3), 225-240.
- Givan, A. L. (2001). Principles of flow cytometry: an overview. *Methods in cell biology*, 63, 19-50.
- Greener, J., & Wimberger-Friedl, R. (2006). Precision injection molding. *Carl Hanser, Munich*.
- Gross, A., Schoendube, J., Zimmermann, S., Steeb, M., Zengerle, R., & Koltay, P. (2015). Technologies for Single-Cell Isolation. *International Journal of Molecular Sciences*, 16(8), 16897-16919.
- Gross, A., Schöndube, J., Niekrawitz, S., Streule, W., Riegger, L., Zengerle, R., & Koltay, P. (2013). Single-cell printer: automated, on demand, and label free. *Journal of laboratory automation*, 18(6), 504-518.
- Gross, G. W., Rieske, E., Kreutzberg, G. W., & Meyer, A. (1977). A new fixed-array multi-microelectrode system designed for long-term monitoring of extracellular single unit neuronal activity in vitro. *Neuroscience Letters*, 6(2), 101-105.
- Gross, G. W., Rieske, E., Kreutzberg, G. W., & Meyer, A. (1977). A new fixed-array multi-microelectrode system designed for long-term monitoring of extracellular single unit neuronal activity in vitro. *Neuroscience Letters*, 6(2), 101-105.
- Guo, J., Li, H., Chen, Y., & Kang, Y. (2014). A microfluidic impedance cytometer on printed circuit board for low cost diagnosis. *IEEE Sensors Journal*, 14(7), 2112-2117.
- Gurdon, J. B. (1971). Use of Frog Eggs and Oocytes for the Study of Messenger RNA and its Translation. *Nature*, 233, 177.
- Hamill, O. P., Marty, A., Neher, E., Sakmann, B., & Sigworth, F. J. (1981). Improved patch-clamp techniques for high-resolution current recording from cells and cell-free membrane patches. *Pflügers Archiv European journal of physiology*, 391(2), 85-100.

- Hierold, C., Hildebrandt, A., Na, U., Scheiter, T., Mensching, B., Steger, M., & Tielert, R. (1996). A pure CMOS surface-micromachined integrated accelerometer. *Sensors and Actuators A: Physical*, 57(2), 111-116.
- Hodgkin, A. L., & Huxley, A. F. (1939). Action potentials recorded from inside a nerve fibre. *Nature*, 144(3651), 710-711.
- Hodgkin, A. L., & Huxley, A. F. (1952). A quantitative description of membrane current and its application to conduction and excitation in nerve. *The Journal of physiology*, 117(4), 500.
- Hodgkin, A. L., & Huxley, A. F. (1952). Currents carried by sodium and potassium ions through the membrane of the giant axon of *Loligo*. *The Journal of physiology*, 116(4), 449.
- Hodgkin, A. L., & Huxley, A. F. (1952). The components of membrane conductance in the giant axon of *Loligo*. *The Journal of physiology*, 116(4), 473-496.
- Hodgkin, A. L., & Huxley, A. F. (1952). The dual effect of membrane potential on sodium conductance in the giant axon of *Loligo*. *The Journal of physiology*, 116(4), 497.
- Hodgkin, A. L., Huxley, A. F., & Katz, B. (1952). Measurement of current-voltage relations in the membrane of the giant axon of *Loligo*. *The Journal of physiology*, 116(4), 424-448.
- Holmes, D., & Morgan, H. (2010). Single cell impedance cytometry for identification and counting of CD4 T-cells in human blood using impedance labels. *Analytical chemistry*, 82(4), 1455-1461.
- Holmes, D., Pettigrew, D., Reccius, C. H., Gwyer, J. D., van Berkel, C., Holloway, J., ... & Morgan, H. (2009). Leukocyte analysis and differentiation using high speed microfluidic single cell impedance cytometry. *Lab on a Chip*, 9(20), 2881-2889.
- Huggett, B., & Lhteenmaki, R. (2012). Public biotech 2011--the numbers. *Nature biotechnology*, 30(8), 751.
- Hulett, H. R., Bonner, W. A., Barrett, J., & Herzenberg, L. A. (1969). Cell sorting: automated separation of mammalian cells as a function of intracellular fluorescence. *Science*, 166(3906), 747-749.
- International Conference on Harmonization . *ICH Harmonised Tripartite Guideline: Derivation and Characterization of Cell Substrates used for Production of Biotechnological/Biological Products Q5D* International Conference on Harmonization; 1997. Published Federal Register. 1998; 63.182:50244-50249. Available at: http://www.ich.org/fileadmin/Public_Web_Site/ICH_Products/Guidelines/Quality/Q5D/Step4/Q5D_Guideline.pdf. Accessed May 15, 2014.

- Jin, L., Han, Z., Platisa, J., Woollorton, J. R., Cohen, L. B., & Pieribone, V. A. (2012). Single action potentials and subthreshold electrical events imaged in neurons with a fluorescent protein voltage probe. *Neuron*, 75(5), 779-785.
- Johnston, D., & Wu, S. M. S. (1994). *Foundations of cellular neurophysiology*. MIT press.
- Kaigala, G. V., Lovchik, R. D., & Delamarche, E. (2012). Microfluidics in the “open space” for performing localized chemistry on biological interfaces. *Angewandte Chemie International Edition*, 51(45), 11224-11240.
- Kaigala, G. V., Lovchik, R. D., Drechsler, U., & Delamarche, E. (2011). A vertical microfluidic probe. *Langmuir*, 27(9), 5686-5693.
- Kalisky, T., & Quake, S. R. (2011). Single-cell genomics. *Nature methods*, 8(4), 311-314.
- Kalisky, T., Blainey, P., & Quake, S. R. (2011). Genomic analysis at the single-cell level. *Annual review of genetics*, 45, 431-445.
- Kantardjieff, A., & Zhou, W. (2013). Mammalian cell cultures for biologics manufacturing. In *Mammalian Cell Cultures for Biologics Manufacturing*. Springer Berlin Heidelberg.
- Kashlan, O. B., & Kleyman, T. R. (2011). ENaC structure and function in the wake of a resolved structure of a family member. *American Journal of Physiology-Renal Physiology*, 301(4), F684-F696.
- Keeney, M., Chin-Yee, I., Weir, K., Popma, J., Nayar, R., & Sutherland, D. R. (1998). Single platform flow cytometric absolute CD34+ cell counts based on the ISHAGE guidelines. *Cytometry*, 34(2), 61-70.
- Kern, R., Sastrawan, R., Ferber, J., Stangl, R., & Luther, J. (2002). Modeling and interpretation of electrical impedance spectra of dye solar cells operated under open-circuit conditions. *Electrochimica Acta*, 47(26), 4213-4225.
- Kim, H. R., Park, B. R. G., & Lee, M. K. (2008). Effects of bacteria and yeast on WBC counting in three automated hematology counters. *Annals of hematology*, 87(7), 557-562.
- King, J. M. H., DiGrazia, P. M., Applegate, B., Burlage, R., & Sanseverino, J. (1990). Rapid, sensitive bioluminescent reporter technology for naphthalene exposure and biodegradation. *Science*, 249(4970), 778.
- Kirby, B. J. (2010). *Micro-and nanoscale fluid mechanics: transport in microfluidic devices*. Cambridge University Press.
- Kontakis, K., Petropoulos, A., Kaltsas, G., Speliotis, T., & Gogolides, E. (2009). A novel microfluidic integration technology for PCB-based devices: Application to microflow sensing. *Microelectronic Engineering*, 86(4), 1382-1384.

- Küttel, C., Nascimento, E., Demierre, N., Silva, T., Braschler, T., Renaud, P., & Oliva, A. G. (2007). Label-free detection of *Babesia bovis* infected red blood cells using impedance spectroscopy on a microfabricated flow cytometer. *Acta tropica*, 102(1), 63-68.
- Lacour, S. P., Atta, R., FitzGerald, J. J., Blamire, M., Tarte, E., & Fawcett, J. (2008). Polyimide micro-channel arrays for peripheral nerve regenerative implants. *Sensors and Actuators A: Physical*, 147(2), 456-463.
- Lee, K. K., He, J., Singh, A., Massia, S., Ehteshami, G., Kim, B., & Raupp, G. (2003). Polyimide-based intracortical neural implant with improved structural stiffness. *Journal of Micromechanics and Microengineering*, 14(1), 32.
- Li, C. W., Cheung, C. N., Yang, J., Tzang, C. H., & Yang, M. (2003). PDMS-based microfluidic device with multi-height structures fabricated by single-step photolithography using printed circuit board as masters. *Analyst*, 128(9), 1137-1142.
- Lovchik, R. D., Kaigala, G. V., Georgiadis, M., & Delamarche, E. (2012). Micro-immunohistochemistry using a microfluidic probe. *Lab on a Chip*, 12(6), 1040-1043.
- Madou, M. J. (1997). *Fundamentals of Microfabrication*. CRC.
- Mandy, F., Nicholson, J., Autran, B., & Janossy, G. (2002). T-cell subset counting and the fight against AIDS: Reflections over a 20-year struggle. *Cytometry*, 50(2), 39-45.
- Marmont, G. (1949). Studies on the axon membrane. I. A new method. *Journal of Cellular and Comparative Physiology*, 34(3), 351-382.
- Marshall, L. A., Wu, L. L., Babikian, S., Bachman, M., & Santiago, J. G. (2012). Integrated printed circuit board device for cell lysis and nucleic acid extraction. *Analytical chemistry*, 84(21), 9640-9645.
- Martina, M., & Taverna, S. (Eds.). (2014). *Patch-clamp methods and protocols*. Humana Press.
- Martinsen, O. G., & Grimnes, S. (2011). *Bioimpedance and bioelectricity basics*. Academic press.
- Meissner, R., Joris, P., Eker, B., Bertsch, A., & Renaud, P. (2012). A microfluidic-based frequency-multiplexing impedance sensor (FMIS). *Lab on a Chip*, 12(15), 2712-2718.
- Melamed, M. R. (2001). A brief history of flow cytometry and sorting. *Methods in cell biology*, 63, 3-17.
- Mercanzini, A., Cheung, K., Buhl, D., Boers, M., Maillard, A., Colin, P., ... & Renaud, P. (2007). Demonstration of cortical recording and reduced inflammatory response using flexible polymer neural probes. *Micro Electro Mechanical Systems, 2007. MEMS. IEEE 20th International Conference on* (pp. 573-576). IEEE.

- Mercanzini, A., Colin, P., Bensadoun, J. C., Bertsch, A., & Renaud, P. (2009). In vivo electrical impedance spectroscopy of tissue reaction to microelectrode arrays. *IEEE Transactions on biomedical engineering*, 56(7), 1909-1918.
- Merrill, D. R., & Tresco, P. A. (2005). Impedance characterization of microarray recording electrodes in vitro. *IEEE transactions on biomedical engineering*, 52(11), 1960-1965.
- Merulla, D., Buffi, N., Van Lintel, H., Renaud, P., & van der Meer, J. R. (2010). Development of a bacterial biosensor for arsenite detection. *Journal of Biotechnology*, 150, 224-225.
- Miledi, R. (1982). A calcium-dependent transient outward current in *Xenopus laevis* oocytes. *Proceedings of the Royal Society of London B: Biological Sciences*, 215(1201), 491-497.
- Miledi, R., Parker, I., & Sumikawa, K. (1982). Properties of acetylcholine receptors translated by cat muscle mRNA in *Xenopus* oocytes. *The EMBO journal*, 1(11), 1307.
- Miledi, R., Parker, I., & Sumikawa, K. (1982). Synthesis of chick brain GABA receptors by frog oocytes. *Proceedings of the Royal Society of London B: Biological Sciences*, 216(1205), 509-515.
- Misawa, N., Mitsuno, H., Kanzaki, R., & Takeuchi, S. (2010). Highly sensitive and selective odorant sensor using living cells expressing insect olfactory receptors. *Proceedings of the National Academy of Sciences*, 107(35), 15340-15344.
- Mitzner, K. (2009). *Complete PCB design using OrCAD Capture and PCB editor*. Newnes.
- Moore, G. E. (2006). Cramming more components onto integrated circuits, Reprinted from *Electronics*, volume 38, number 8, April 19, 1965, pp. 114 ff. *IEEE Solid-State Circuits Society Newsletter*, 20(3), 33-35.
- Morgan, H., Sun, T., Holmes, D., Gawad, S., & Green, N. G. (2006). Single cell dielectric spectroscopy. *Journal of Physics D: Applied Physics*, 40(1), 61.
- Muller G. (2016). *Microwell and impedance-based approaches to isolate single cells for life sciences*, EPFL Thesis
- Neumann, E., Schaefer-Ridder, M., Wang, Y., & Hofschneider, P. H. (1982). Gene transfer into mouse lyoma cells by electroporation in high electric fields. *The EMBO Journal*, 1(7), 841-5.
- Nguyen, N. T., & Huang, X. (2001). Miniature valveless pumps based on printed circuit board technique. *Sensors and Actuators A: Physical*, 88(2), 104-111.
- Ormerod, M. G., & Novo, D. (2008). *Flow cytometry: a basic introduction*. Michael G. Ormerod.

- Pakula, L. S., Yang, H., Pham, H. T. M., French, P. J., & Sarro, P. M. (2004). Fabrication of a CMOS compatible pressure sensor for harsh environments. *Journal of Micromechanics and Microengineering*, 14(11), 1478.
- Philippidis, A. (2015). The Top 25 Best-Selling Drugs of 2014. <http://www.genengnews.com/the-lists/the-top-25-best-selling-drugs-of-2014/77900383?page=2>, Accessed on March 03, 2017
- Robinson, J. P. (2013). Wallace H. Coulter: Decades of invention and discovery. *Cytometry Part A*, 83(5), 424-438.
- Rossier, B. C. (2014). Epithelial sodium channel (ENaC) and the control of blood pressure. *Current opinion in pharmacology*, 15, 33-46.
- Sadiku, A., & Alexander, C. K. (2009). Fundamentals of electric circuits. *International Edition, Mc Graw Hill*.
- Sakata, T., & Miyahara, Y. (2007, November). Drug transport measurement for transporter variants using oocyte-based field effect transistor. In *Microprocesses and Nanotechnology, 2007 Digest of papers* (pp. 514-515). IEEE.
- Sakata, T., & Miyahara, Y. (2008). Noninvasive Monitoring of Transporter- Substrate Interaction at Cell Membrane. *Analytical chemistry*, 80(5), 1493-1496.
- Schaffhauser, D. F., Andrini, O., Ghezzi, C., Forster, I. C., Franco-Obregón, A., Egli, M., & Dittrich, P. S. (2011). Microfluidic platform for electrophysiological studies on *Xenopus laevis* oocytes under varying gravity levels. *Lab on a Chip*, 11(20), 3471-3478.
- Schaffhauser, D. F., Patti, M., Goda, T., Miyahara, Y., Forster, I. C., & Dittrich, P. S. (2012). An integrated field-effect microdevice for monitoring membrane transport in *Xenopus laevis* oocytes via lateral proton diffusion. *PloS one*, 7(7), e39238.
- Schmitt, B. M., & Koepsell, H. (2002). An improved method for real-time monitoring of membrane capacitance in *Xenopus laevis* oocytes. *Biophysical journal*, 82(3), 1345-1357.
- Schnizler, K., Küster, M., Methfessel, C., & Fejtl, M. (2003). The roboocyte: automated cDNA/mRNA injection and subsequent TEVC recording on *Xenopus* oocytes in 96-well microtiter plates. *Receptors and Channels*, 9(1), 41-48.
- Schoendube, J., Wright, D., Zengerle, R., & Koltay, P. (2015). Single-cell printing based on impedance detection. *Biomicrofluidics*, 9(1), 014117.
- Schulze, D., Tölke, R., & Widmann, I. (2014). Noble Metal PCB Manufacturing for Direct Implants. *Market Outlook*, 202, 0.
- Shanahan, T. (1997). Application of flow cytometry in transplantation medicine. *Immunological investigations*, 26(1-2), 91-101.

- Shapiro, H. M. (2004). The evolution of cytometers. *Cytometry Part A*, 58(1), 13-20.
- Shapiro, H.M. (2003). *Practical Flow Cytometry*, 4th ed.; Wiley-Liss: New York, NY, USA.
- Shear, J. B., Fishman, H. A., Allbritton, N. L., & Garigan, D. (1995). Single cells as biosensors for chemical separations. *Science*, 267(5194), 74.
- Shear, J. B., Fishman, H. A., Allbritton, N. L., & Garigan, D. (1995). Single cells as biosensors for chemical separations. *Science*, 267(5194), 74.
- Sherman-Gold, R. (1993). *The axon guide for electrophysiology & biophysics: Laboratory techniques*. Axon Instruments.
- Shi, J., Ahmed, D., Mao, X., Lin, S. C. S., Lawit, A., & Huang, T. J. (2009). Acoustic tweezers: patterning cells and microparticles using standing surface acoustic waves (SSAW). *Lab on a Chip*, 9(20), 2890-2895.
- Siegel, M. S., & Isacoff, E. Y. (1997). A genetically encoded optical probe of membrane voltage. *Neuron*, 19(4), 735-741.
- Spira, M. E., & Hai, A. (2013). Multi-electrode array technologies for neuroscience and cardiology. *Nature nanotechnology*, 8(2), 83-94.
- Stephan, K., Pittet, P., Renaud, L., Kleimann, P., Morin, P., Ouaini, N., & Ferrigno, R. (2007). Fast prototyping using a dry film photoresist: microfabrication of soft-lithography masters for microfluidic structures. *Journal of Micromechanics and Microengineering*, 17(10), N69.
- Stühmer, W. (1998). Electrophysiologic recordings from *Xenopus* oocytes. *Methods in enzymology*, 293, 280-300.
- Sun, T., & Morgan, H. (2010). Single-cell microfluidic impedance cytometry: a review. *Microfluidics and Nanofluidics*, 8(4), 423-443.
- Sun, T., Gawad, S., Bernabini, C., Green, N. G., & Morgan, H. (2007). Broadband single cell impedance spectroscopy using maximum length sequences: theoretical analysis and practical considerations. *Measurement Science and Technology*, 18(9), 2859.
- Sun, T., Gawad, S., Green, N. G., & Morgan, H. (2006). Dielectric spectroscopy of single cells: time domain analysis using Maxwell's mixture equation. *Journal of Physics D: Applied Physics*, 40(1), 1.
- Sze, S. M., & Ng, K. K. (2006). *Physics of semiconductor devices*. John Wiley & sons.
- Tanaka, Y., Funano, S. I., Nishizawa, Y., Kamamichi, N., Nishinaka, M., & Kitamori, T. (2016). An electric generator using living Torpedo electric organs controlled by fluid pressure-based alternative nervous systems. *Scientific reports*, 6.

- Temiz, Y., Lovchik, R. D., Kaigala, G. V., & Delamarche, E. (2015). Lab-on-a-chip devices: How to close and plug the lab?. *Microelectronic Engineering*, 132, 156-175.
- Thomas, R. S., Morgan, H., & Green, N. G. (2009). Negative DEP traps for single cell immobilisation. *Lab on a Chip*, 9(11), 1534-1540.
- Tornay, R., Chapuis, V., Haguët, V., Chatelain, F., & Renaud, P. (2007, June). Electrical detection and ejection of beads in a one-cell-per-drop microdispenser. In *Solid-State Sensors, Actuators and Microsystems Conference, 2007. TRANSDUCERS 2007. International* (pp. 695-698). IEEE.
- Tung, J. W., Heydari, K., Tirouvanziam, R., Sahaf, B., Parks, D. R., Herzenberg, L. A., & Herzenberg, L. A. (2007). Modern flow cytometry: a practical approach. *Clinics in laboratory medicine*, 27(3), 453-468.
- Updike, S. J., & Hicks, G. P. (1967). The enzyme electrode. *Nature*, 214, 986-988.
- Van der Meer, J. R. (2010). Bacterial sensors: synthetic design and application principles. *Synthesis lectures on synthetic biology*, 2(1), 1-167.
- Van Der Meer, J. R., & Belkin, S. (2010). Where microbiology meets microengineering: design and applications of reporter bacteria. *Nature Reviews Microbiology*, 8(7), 511-522.
- van Heeren, H., Tantra, R., & Salomon, P. (2015). Microfluidic devices: a road forward by standardization of interconnects and classification. *Microfluidics and Nanofluidics*, 19(5), 1203-1207.
- Vasilakis, N., Moschou, D., Carta, D., Morgan, H., & Prodromakis, T. (2016). Long-lasting FR-4 surface hydrophilisation towards commercial PCB passive microfluidics. *Applied Surface Science*, 368, 69-75.
- Verkhatsky, A., Krishtal, O. A., & Petersen, O. H. (2006). From Galvani to patch clamp: the development of electrophysiology. *Pflügers Archiv*, 453(3), 233-247.
- Vermeulen, L., Todaro, M., de Sousa Mello, F., Sprick, M. R., Kemper, K., Perez Alea, M., ... Medema, J. P. (2008). Single-cell cloning of colon cancer stem cells reveals a multi-lineage differentiation capacity. *Proceedings of the National Academy of Sciences of the United States of America*, 105(36), 13427-32.
- Volpatti, L. R., & Yetisen, A. K. (2014). Commercialization of microfluidic devices. *Trends in biotechnology*, 32(7), 347-350.
- Vulto, P., Glade, N., Altomare, L., Bablet, J., Del Tin, L., Medoro, G., ... & Guerrieri, R. (2005). Microfluidic channel fabrication in dry film resist for production and prototyping of hybrid chips. *Lab on a Chip*, 5(2), 158-162.

- Wang, Q., Moser, J. E., & Grätzel, M. (2005). Electrochemical impedance spectroscopic analysis of dye-sensitized solar cells. *The Journal of Physical Chemistry B*, 109(31), 14945-14953.
- Wang, X., Becker, F. F., & Gascoyne, P. R. (2002). Membrane dielectric changes indicate induced apoptosis in HL-60 cells more sensitively than surface phosphatidylserine expression or DNA fragmentation. *Biochimica et Biophysica Acta (BBA)-Biomembranes*, 1564(2), 412-420.
- Weber, W. M. (1999). Ion currents of *Xenopus laevis* oocytes: state of the art. *Biochimica et Biophysica Acta (BBA)-Biomembranes*, 1421(2), 213-233.
- Wego, A., Richter, S., & Pagel, L. (2001). Fluidic microsystems based on printed circuit board technology. *Journal of Micromechanics and Microengineering*, 11(5), 528.
- Werlen, C., Jaspers, M. C., & van der Meer, J. R. (2004). Measurement of biologically available naphthalene in gas and aqueous phases by use of a *Pseudomonas putida* biosensor. *Applied and environmental microbiology*, 70(1), 43-51.
- WHO, 2014. WHO Expert Committee on Biological Standardization. World Health Organization technical report series, 1-266, back cover
- Wu, A., Wang, L., Jensen, E., Mathies, R., & Boser, B. (2010). Modular integration of electronics and microfluidic systems using flexible printed circuit boards. *Lab on a Chip*, 10(4), 519-521.
- Wurm, F. M. (2004). Production of recombinant protein therapeutics in cultivated mammalian cells. *Nature biotechnology*, 22(11), 1393-1398.
- Young, J. Z. (1936, January). Structure of nerve fibres and synapses in some invertebrates. In *Cold Spring Harbor Symposia on Quantitative Biology* (Vol. 4, pp. 1-6). Cold Spring Harbor Laboratory Press.
- Yusof, A., Keegan, H., Spillane, C. D., Sheils, O. M., Martin, C. M., O'Leary, J. J., ... & Koltay, P. (2011). Inkjet-like printing of single-cells. *Lab on a Chip*, 11(14), 2447-2454.
- Zhang, K., Han, X., Li, Y., Li, S. Y., Zu, Y., Wang, Z., & Qin, L. (2014). Hand-Held and Integrated Single-Cell Pipettes. *Journal of the American Chemical Society*, 136(31), 10858-10861.
- Zimmermann, U., Pilwat, G., & Riemann, F. (1974). Dielectric breakdown of cell membranes. *Biophys J.*, 14(11), 881-99.

Chapter 7: **Appendix**

7.1 Hair follicle morphogenetic assay using the instrumented pipette. Figure reprinted from Georges Muller PhD thesis

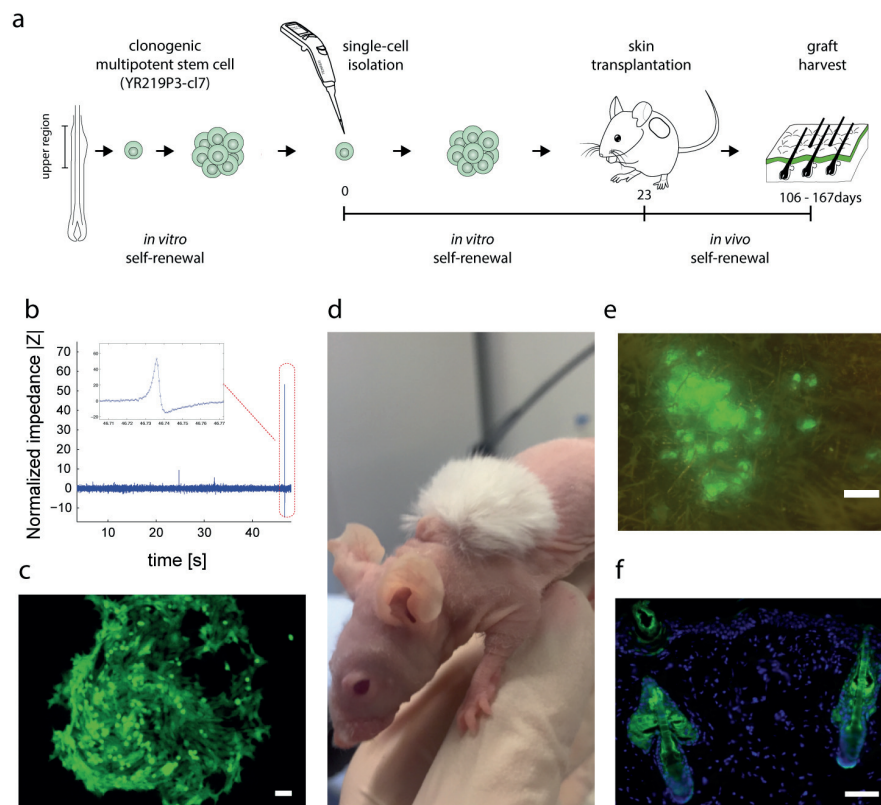


Figure 7.1 : Figure courtesy of Georges Muller (Muller, 2016). Hair follicle morphogenetic assay of rat hair follicle multipotent stem cells. Sub-clones were derived from single YR219P3-cl7 cells (Claudinot et al., PNAS, 2005) isolated with the instrumented pipette. Cells were cultured for 7 days. Wells were then searched for subclones. Growing subclones were selected and amplified twice in culture. A mass culture of the clone YR219P3-cl7 was used as a control. Each clonal progeny and the mass culture were injected at the dermal-epidermal junction on the back of a newborn mouse. Each graft was transplanted onto the back of a NUDE mouse. (a) Schematic of the assay. (b-f) Results of the subclone 2 harvested 106 days after transplantation. (b) Impedance trace documenting the single-cell origin of the subclone. (c) Micrograph of the subclone after 5 days in culture. (d) View of the transplant on the back of the NUDE mouse showing growing hair follicles (e) UV-illumination of the harvested transplant revealed the presence of EGFP+ hair follicles (top view). (f) Immuno-histology of the transplant. Scale bars: c: 50 μm , d: 100 μm , e: 100 μm , f: 50 μm .

7.2 Python code: Sensing tip analytical model

```
# -*- coding: utf-8 -*-
# Sensing tip analytical model
# Author: D. Bonzon

#####
# Imports #
#####

import matplotlib.pyplot as plt
import numpy as np
import math
from scipy.misc import imread
import time
import numpy as np

#####
# Definitions #
#####

#PI
pi = 3.1415

#Diametre extérieur tip petit coté
De = 1.1e-3
#Diametre intérieur tip petit coté
Di1 = 500e-6
#Diametre intérieur tip grand coté
Di2 = 5.0e-3
#Longeur tip
L = 50e-3
#Position de l'electrode interne
l = 3.5e-3
#Epaisseur de la membrane
e = 15e-6
#Diamètre du trou
d = 30e-6

#Longueur sur lequel les graphs sont tracés
Laff = 3.5e-3

# Constantes physique electrique
rho = 0.65

# Constantes physique fluidique
mu = 1e-3

# Constantes physique bruit
Kb = 1.38e-23
T = 300
dF = 2400

# Constante de calcul
#spatial
NPAS = 2500

INT_LENGTH = (De/2) + 1
```

```

dx = INT_LENGTH / NPAS

# Fin des domaines
# from -De/2 to 0
DOMAIN1 = 0
# from 0 to e
DOMAIN2 = e
# from e to l
DOMAIN3 = l
# from l to L
DOMAIN4 = L
# from l to L

#####
# Variables #
#####

X = [0]*NPAS
Xum = [0]*NPAS
R = [0]*NPAS
U = [0]*NPAS

dR = [0]*NPAS
dU = [0]*NPAS
dJ = [0]*NPAS

deltaI = [0]*NPAS

Rtot_PosPart = [0]*NPAS

Uexc = 0.5
Rtot = 0
Itot = 0

#####
# Fonctions #
#####

#Retour la resistance infinitesimal de la position pos en fonction de
position pos_part de la particule et de son diamètre diam_part
# pos et pos_part sont en mètres

def eval_dR(pos, pos_part, diam_part, delta_x):

    #Evaluation de la section occupée par la particule
    if(diam_part > 0):
        if( ( pos > ( pos_part-(diam_part/2) ) ) and ( pos < (
pos_part+(diam_part/2) ) ) ):
            fleche = (diam_part/2) - abs(pos-pos_part)
            corde = 2*math.sqrt((diam_part-fleche)*fleche)
            SectPart = pi*(corde/2)**2
        else:
            SectPart = 0
    else:
        SectPart = 0

    #Evaluation de la resistance infinitesimale locale
    deltaR = 0
    if(pos<DOMAIN1):
        rayon=-pos
        deltaR = (rho*delta_x)/((2*pi*(rayon+d/2)**2) - SectPart)
        #deltaR = (rho*delta_x)/((pi*(rayon+d/2)**2) - SectPart)

```



```

elif(pos<DOMAIN2):
    deltaR = (rho*delta_x)/((d/2)**2*pi) - SectPart)
elif(pos<DOMAIN3):
    rayon = pos - e
    deltaR = max( (rho*delta_x)/(((Di1+((Di2-Di1)*pos)/L))/2)**2*pi)
- SectPart ) , (rho*delta_x)/(2*pi*(rayon+d/2)**2) - SectPart ) )
    #deltaR = max( (rho*delta_x)/(((Di1+((Di2-
Di1)*pos)/L))/2)**2*pi) - SectPart ) , (rho*delta_x)/(pi*(rayon+d/2)**2)
- SectPart ) )
    else:
        deltaR = 0

    return deltaR

#####
# Initialization #
#####

f_static_R = open('Dropbox/PhD/ModelPipette/Results/resultsStaticR.txt',
'w')
f_static_U = open('Dropbox/PhD/ModelPipette/Results/resultsStaticU.txt',
'w')
f_particules =
open('Dropbox/PhD/ModelPipette/Results/resultsParticles.txt', 'w')

#####
# Calculs #
#####

# calcul de l'axe des x
for i in range(NPAS):
    X[i] = i*dx - (De/2)
    Xum[i] = X[i]*1000000

# calcul sans particule

position_particule = 0
diametre_particule = 0

R[0] = 0
U[0] = Uexc

for i in range(NPAS):
    position = X[i]

    #Calcul de dR
    dR[i] = eval_dR(position, position_particule, diametre_particule, dx)

    #Calcul de R
    if(i>0):
        R[i] = R[i-1] + dR[i]

    f_static_R.write(str(position)+'\t'+str(dR[i])+'\t'+str(R[i])+'\n')

#Calcul de i
Rtot = R[NPAS-1]
Itot = Uexc / Rtot

for i in range(NPAS):
    position = X[i]
    #Calcul de dU

```

```

dU[i] = -dR[i]*Itot

#Calcul de U
if(i>0):
    U[i] = U[i-1] + dU[i]

#calcul de dJ
dJ[i] = (Itot*dR[i])/(rho*dx)

f_static_U.write(str(position)+'\t'+str(dU[i])+'\t'+str(U[i])+'\t'+str(dJ[i])+'\n')

# Calcul parametrique avec particules

DiamTip = [500e-6]

PosElectrode = [3500e-6]
#PosElectrode = [it * 1e-6 for it in range(250, 4001, 250)]

MembraneThickness = [15e-6]

DiamAperture = [35e-6]
#DiamAperture = [it * 1e-6 for it in range(45, 70, 5)]

DiamParticule = [15e-6]
#DiamParticule = [0, 6e-6, 10e-6, 12e-6, 15e-6]
#DiamParticule = [it * 1e-9 for it in range(0, 15100, 100)]

for Dil in DiamTip:
    for l in PosElectrode:
        DOMAIN3 = l
        INT_LENGTH = (De/2) + l
        dx = INT_LENGTH / NPAS

        for i in range(NPAS):
            X[i] = i*dx - (De/2)
            Xum[i] = X[i]*1000000

        for e in MembraneThickness:
            DOMAIN2 = e

            for d in DiamAperture:

                R[0] = 0
                for i in range(NPAS):
                    pos = X[i]
                    dR[i] = eval_dR(pos, 0, 0, dx)
                    if(i>0):
                        R[i] = R[i-1] + dR[i]

                Rbase = R[NPAS-1]
                Rmesure = 30e3
                jNoise =
math.sqrt(4*Kb*T*((Rbase*Rmesure)/(Rbase+Rmesure))*dF)
                RNoise = (jNoise*(Rbase+Rmesure))/Uexc

```

```

        for dp in DiamParticule:

            for ind_part in range(NPAS):
                pos_particule = X[ind_part]

                #Calculs dR,R
                R[0] = 0
                for i in range(NPAS):
                    pos = X[i]
                    dR[i] = eval_dR(pos, pos_particule, dp, dx)
                    if(i>0):
                        R[i] = R[i-1] + dR[i]

                Rtot_PosPart[ind_part] = R[NPAS-1] #Rtot pour
chaque position de particule

                Rmax = max(Rtot_PosPart)

f_particules.write(str(dx)+'\t'+str(l)+'\t'+str(Dil)+'\t'+str(e)+'\t'+str(d
)+'\t'+str(dp)+'\t'+str(Rbase)+'\t'+str(Rmax)+'\t'+str(Rmax-
Rbase)+'\t'+str(100*(Rmax-Rbase)/Rbase)+'\t'+str(RNoise)+'\n')
                print "dx=",dx,"pos=",l," diam_tip=",Dil," mem=",e,"
aperture=",d," part=", dp, " Rbase=", Rbase, "Rpeak=", Rmax, "deltaR=",
(Rmax-Rbase), "%=", ((Rmax-Rbase)/Rbase)*100, "Rnoise=", RNoise

#####
# Affichage #
#####

fig = plt.figure("Figure "+str(diametre_particule), figsize=(15,8))

plt.subplot(311)
plt.plot(Xum,dR, label="Diff Res")
plt.axis([- (De/2)*1000*1000, Laff*1000*1000, 0, 3000])
plt.ylabel('Resistance [ohm]')
plt.xlabel('Position [um]')
plt.grid()

plt.subplot(312)
plt.plot(Xum,R, label="Resistance")
plt.axis([- (De/2)*1000*1000, Laff*1000*1000, 0, 35000])
plt.ylabel('Resistance [ohm]')
plt.xlabel('Position [um]')
plt.grid()

plt.subplot(313)
plt.plot(Xum,U, label="Potential")
plt.axis([- (De/2)*1000*1000, Laff*1000*1000, 0, 0.6])
plt.ylabel('Potentiel [V]')
plt.xlabel('Position [um]')
plt.grid()

plt.show()
f_static_R.close()
f_static_U.close()
f_particules.close()

```

7.3 Matlab code: Spatiotemporal ion distribution model for electrically active cells

```
%% Spatiotemporal ion distribution model for electrically active cells
%% AUTHOR: D.Bonzon
%% Last version: 03.03.2017

%% CLEAR
clear all;
close all;

%% CONSTANTS

ESPECE = 4;
NA = 1;
K = 2;
CL = 3;
NPI = 4;
Z = [1,1,-1,-1];

SIZE = 10000;

FRONTIER1 = 4800;    % 10nm membrane
FRONTIER2 = 5200;

ITERATIONS = 333333;
AFF_PAR_IT = 166666;

dt = 0.3e-12;
dx = 0.25e-10;

Q = 1.602e-19;
e0 = 8.854e-12;
er = 5;
NAV = 6.022e23;
kT = 4.11e-21;
%Mobility coefficients [m^2/v*sec]
mu(NA) = 10.12e-8;
mu(K) = 4.98e-8;
mu(CL) = 6.88e-8;
mu(NPI) = 6.88e-8;

%% INITIALIZATIONS
X = zeros(1,SIZE);
for i = 1:SIZE
    X(i) = (i-1)*dx;
end
Xnm = X.*1000*1000*1000;

T = zeros(1,ITERATIONS);
for t = 1:ITERATIONS
    T(t) = (t-1)*dt;
end
```

```

CONCENTRATION_NA_IN = 10;
CONCENTRATION_K_IN = 90;
CONCENTRATION_CL_IN = 100;
CONCENTRATION_NPI_IN = 0;

CONCENTRATION_NA_MEM = 0;
CONCENTRATION_K_MEM = 0;
CONCENTRATION_CL_MEM = 0;
CONCENTRATION_NPI_MEM = 0;

CONCENTRATION_NA_OUT = 90;
CONCENTRATION_K_OUT = 10;
CONCENTRATION_CL_OUT = 100;
CONCENTRATION_NPI_OUT = 0;

Seff(:,NA) = zeros(1,SIZE);
Seff(:,K) = zeros(1,SIZE);
Seff(:,CL) = zeros(1,SIZE);
Seff(:,NPI) = zeros(1,SIZE);
N(:,NA) = zeros(1,SIZE);
N(:,K) = zeros(1,SIZE);
N(:,CL) = zeros(1,SIZE);
N(:,NPI) = zeros(1,SIZE);
Grad_N(:,NA) = zeros(1,SIZE);
Grad_N(:,K) = zeros(1,SIZE);
Grad_N(:,CL) = zeros(1,SIZE);
Grad_N(:,NPI) = zeros(1,SIZE);
Grad_J(:,NA) = zeros(1,SIZE);
Grad_J(:,K) = zeros(1,SIZE);
Grad_J(:,CL) = zeros(1,SIZE);
Grad_J(:,NPI) = zeros(1,SIZE);
Charge = zeros(1,SIZE);
Champ = zeros(1,SIZE);
LocalConductance = zeros(1,SIZE);

PotentialTime = zeros(1,ITERATIONS);

cnt = 1;
for i = 1:FRONTIER1
    N(i,NA) = CONCENTRATION_NA_IN*NAV;
    N(i,K) = CONCENTRATION_K_IN*NAV;
    N(i,CL) = CONCENTRATION_CL_IN*NAV;
    N(i,NPI) = CONCENTRATION_NPI_IN*NAV;
    Seff(i,NA) = 1;
    Seff(i,K) = 1;
    Seff(i,CL) = 1;
    Seff(i,NPI) = 1;
end
for i = FRONTIER1:FRONTIER2
    N(i,NA) = CONCENTRATION_NA_MEM*NAV;
    N(i,K) = CONCENTRATION_K_MEM*NAV;
    N(i,CL) = CONCENTRATION_CL_MEM*NAV;
    N(i,NPI) = CONCENTRATION_NPI_MEM*NAV;
    Seff(i,NA) = 0;
    Seff(i,K) = 1/10;
    Seff(i,CL) = 0;
    Seff(i,NPI) = 0;
end
for i = FRONTIER2:SIZE
    N(i,NA) = CONCENTRATION_NA_OUT*NAV;
    N(i,K) = CONCENTRATION_K_OUT*NAV;

```

```

N(i,CL) = CONCENTRATION_CL_OUT*NAV;
N(i,NPI) = CONCENTRATION_NPI_OUT*NAV;
Seff(i,NA) = 1;
Seff(i,K) = 1;
Seff(i,CL) = 1;
Seff(i,NPI) = 1;
end

%% COMPUTATION
for t = 1:ITERATIONS

    %Channel state
    if(t>166667)
        for i = FRONTIER1:FRONTIER2
            Seff(i,NA) = 1/2;
            Seff(i,K) = 1/10;
            Seff(i,CL) = 0;
            Seff(i,NPI) = 0;
        end
    end

    %Charge
    Charge=Q*(Z(1)*N(:,1)+Z(2)*N(:,2)+Z(3)*N(:,3)+Z(4)*N(:,4));
    %Field
    Champ = (1/(e0*er)).*cumtrapz(X,Charge);
    %Potential
    Potential = -cumtrapz(X,Champ);
    Potential(SIZE)

    LocalConductance = 0;

    PotentialTime(t) = Potential(SIZE);

    for i = 1:ESPECE
        %Concentration gradient
        Grad_N(:,i) = gradient(N(:,i),dx);
        %Diffusion current
        JDiffusion(:,i) = sign(Z(i))*(kT).*mu(i).*Grad_N(:,i);
        %Drift current
        JDrift(:,i) = abs(Z(i))*Q*mu(i)*N(:,i).*Champ;
        %Total current
        JTot(:,i) = Seff(:,i).*(JDrift(:,i)-JDiffusion(:,i));
        %Current gradient
        Grad_J(:,i) = gradient(JTot(:,i),dx);
        %Continuity
        N(:,i) = N(:,i) - (1/(Q*Z(i))) * Grad_J(:,i).*dt;
    end

    %% PLOTS
    if(mod(t-1,AFF_PAR_IT)==0)

        figure(t)
        hold on;
        grid on;
        rectangle('Position',[120,0,10,12e25],'FaceColor',[0.88 .93
.99],'EdgeColor','w','LineWidth',0.1)
        plot(Xnm,N(:,NA),'b')
        plot(Xnm,N(:,K),'g')
        plot(Xnm,N(:,CL),'r')
        plot(Xnm,N(:,NPI),'k')
        xlabel('Distance [nm]')

```

```

ylabel('Nb ions [m-3'])
legend('Na', 'K', 'Cl', 'NPI')
xlim([115 135])

figure(t+1)
hold on;
grid on;
plot(Xnm, Charge, 'r')
xlabel('Distance [nm]')
ylabel('Charge [C/m3'])
xlim([115 135])

figure(t+2)
hold on;
grid on;
plot(Xnm, Champ, 'g')
xlabel('Distance [nm]')
ylabel('Champ [V/m]')
xlim([115 135])

figure(t+3)
hold on;
grid on;
rectangle('Position',[120,-0.1,10,0.25],'FaceColor',[0.88 .93
.99],'EdgeColor','w','LineWidth',0.1)
plot(Xnm, Potential, 'b')
xlabel('Distance [nm]')
ylabel('Potential [V]')
xlim([115 135])

figure(t+6)
hold on;
grid on;
rectangle('Position',[120,-12000,10,24000],'FaceColor',[0.88 .93
.99],'EdgeColor','w','LineWidth',0.1)
plot(Xnm, JTot(:,NA), 'b')
plot(Xnm, JTot(:,K), 'g')
plot(Xnm, JTot(:,CL), 'r')
plot(Xnm, JTot(:,NPI), 'k')
xlabel('Distance [nm]')
ylabel('J [A/m2']')
xlim([115 135])

figure(t+7)
hold on;
grid on;

yyaxis left
plot(Xnm, -Potential, 'b')
xlabel('Distance [nm]')
ylabel('Epot [eV]')
xlim([115 135])

yyaxis right
plot(Xnm, Potential, 'b')
xlabel('Distance [nm]')
ylabel('Potential [V]')
xlim([115 135])

```

```
        set(gca,'YDir','reverse');  
    end  
  
end  
  
figure(99)  
hold on;  
grid on;  
plot(T,PotentialTime.*1000,'b')  
xlabel('Time [s]')  
ylabel('Potential [mV]')
```




David Bonzon
Ch. du Bois-de-Ruz 1
1801 Mont-Pèlerin
Suisse

079 729 37 19

dbonzon@bluewin.ch

29.03.1986
Swiss citizen
Single

David Bonzon

PhD candidate in microelectronic & microsystem at EPFL.

I have curiosity to discover, passion for entrepreneurship and determination to succeed.

Education

PhD in Microelectronics & Microsystems, EPFL, 2012 to present

Impedance spectroscopy for single-cells analysis and dispensing

MSc Microengineering, EPFL, Lausanne, 2010 – 2012

Orientation Micro-, Nano Systems and Biomedical Technologies

Final Master grade of 5.75 / 6

- Master project at Prof. M. J. Madou Group, University of California, Irvine : « *Use of Electro Spinning for Structural Color Applications* »

- Two semester projects in startup with Biocartis SA: « *Microfluidic Pumping System* » & « *Séchage de canaux microfluidiques remplis de disques de silicium* »

Venture Challenge, VentureLab, Lausanne, 2011

A 14 weeks class to develop a business idea

BSc Microengineering, EPFL, Lausanne, 2006 – 2009

Propédeutique Grade : 5.66 / 6, Bachelor Grade 5.49 / 6

Cours de Mathématiques Spécial, EPFL, Lausanne, 2005 - 2006

Ecole Technique et des Métiers de Lausanne, Lausanne, 2002 - 2005

Electronics Apprenticeship. School Award, Practice Prize 2004 & 2005, Sport Prize and Prize for the best grade in the "Canton de Vaud" after final exams

Working experience

Doctoral Assistant, LMIS4, EPFL, 2012 - present

Start-up Development, Pandora Underwater Equipment SA, 2008 - 2013

Co-founder of Pandora Underwater Equipment SA, a start-up focusing on development and marketing of premium safety underwater equipments. Pandora is now funded by Business Angels, VentureKick, Departement de l'économie du Canton de Vaud and was awarded the CTI Startup Label. I focused on the technological proof of principle and the company operations were taken over by a management team since 2013.

Venture Leaders program: Swiss Start-up national Team, 2011

10 days Business Development Program in Boston with executive education at Babson College and workshops with VC and experts.

iCAN'11 International Contest in Nano/micro technology, 2011

Third prize at the iCan'11 Finals in Beijing with the project « Sensing the world through smartphone »

Hardware engineer, Novano, Lausanne, 2009 - 2010 (part time)

Development and design of a high speed digital signal PCB that became integrated in one of Novano's solution.

Web application development, Freelancer, 2002 - 2012

Web applications development focusing on team management, invoicing & sales for sports club and associations.

Intern, Radio Suisse Romande, Lausanne, 2005

Intern, ThermoFisher Scientific, Lausanne, 2002

Qualification profile

Softwares:

Altium Designer, SolidWorks, Matlab, COMSOL, XCode, Word, Excel, PowerPoint, Mathematica, ImageJ

Processes:

Electronic & Microfluidic design, Machining & Fast prototyping, SEM Observation, Cleanroom processing

Programming languages:

C, C++, Matlab, Java, Python, Assembleur (Atmel), PHP/MySQL, XHTML/CSS

Others:

Patent strategy and writing

Languages

French : mother tongue, English : level C2, German : level A2

Hobbies

Ski mountaineering (Patrouille des Glaciers 2010 & 2014), Road bicycle racing, Triathlon, Running

List of publications

Peer reviewed articles

Bonzon, D., Martinez-Duarte, R., Renaud, P., & Madou, M. (2014). Biomimetic *Pieris rapae*'s nanostructure and its use as a simple sucrose sensor. *Micromachines*, 5(2), 216-227.

Conferences

Bonzon, D., Bargeton, B., Benton, R., & Renaud, P. (2016). *Xenopus Laevis* oocyte based Biosensors. *Nano-Tera Annual Meeting 2016*

Bonzon, D., Muller, G., Barrandon, Y., & Renaud, P. (2015). Microfabrication on a pipette tip for single cell dispensing. *Nanobiotech, Montreux, Switzerland*

Bonzon, D., Muller, G., Barrandon, Y., & Renaud, P. (2014). Single-cell dispensing on a pipette. *Nanobiotech, Montreux, Switzerland*

Bonzon, D., Bargeton, B., Benton, R., Giovanna, Z., & Renaud, P. (2014) *Xenopus Laevis* oocyte based Biosensors. *Nano-Tera Annual Meeting 2014*

Patents

Bonzon, D., Bonzon, J.-P., Muller, G., Bureau, J.-B., Barrandon, Y., Renaud, P. (2017). *Tip connector for fluidic and electrical connection*. PCT/IB2017/052088

Bonzon, D., Lany, M., Van Neyghem, N., Aeberli, L., Choppe, J., Muller, G., & Renaud, P. (2017). *Method for manufacturing a microfluidic sensor*. PCT/IB2017/051385

Bonzon, D. V., Muller, G. H., Renaud, P., Barrandon, Y., Bureau, J.-B., & Béguin, S. (2016). *Devices, systems and methods for dispensing and analysing particles*. WO 2016166729 A1

Bonzon, D. V., Béguin, S., Forchelet, D., Muller, G. H., Renaud, P., & Barrandon, Y. (2016). *Observation device with optical compensation*. WO 2016120757 A1

Bonzon, D. V., Muller, G. H., Renaud, P., & Barrandon, Y. (2014). *Sensing tip with electrical impedance sensor*. WO 2015056176 A1

Bonzon, D., Sinclair, A., Glez, C., & Webb, C. (2012). *Vent valve for diver's buoyancy compensator*. WO 2013144712 A3

Bonzon, D., Sinclair, A., Glez, C., & Webb, C. (2012). *A safe automatic buoyancy control device*. WO 2013144711 A1

